ABSTRACT

Title of Dissertation:	CHEMICAL SENSING WITH A TUBE-IN-A-TUBE NANOSTRUCTURE
	Benjamin Kerr Barnes, Doctor of Philosophy, 2022
Dissertation directed by:	Professor YuHuang Wang, Department of Chemistry and Biochemistry

Carbon nanotube field-effect transistors (FETs) exhibit exceptional electrical properties such as ballistic conductance and record-high carrier mobility that make them attractive for potential applications in chemical sensing. Successfully translating these properties to FET chemical sensors may advance the fields of medical diagnosis and *in vivo* chemical detection for a revolutionary impact on public health and personalized medicine. To this end, we must address multiple challenges for electrical detection, including 1) the need for simultaneous rapid detection and sensitivity to trace amounts of target molecules, 2) the need for detection in high ionic strength conditions, which tend to dampen the field-effect. 3) New fabrication routes are needed for producing FET chemical sensors at scale without compromising their superior electrical properties, and 4) new device form factors are needed for *in vivo* biosensing that combine these favorable electrical characteristics with biocompatibility, mechanical flexibility, and chemical sensitivity.

The commonality in these seemingly diverse challenges is a lack of structure control at multiple length scales, from 10^{-9} m to 1 m. Particle length and surface defects at the single-nanostructure or nanometer-level dictate the electrical properties and target-probe kinetics, and therefore provide a fundamental lower limit of signal transduction. Furthermore, controlling the surface chemical properties at this scale can be used to tune sensing characteristics in high ionic strength conditions. Controlling the interactions and positioning of multiple nanostructures within a device (on the micrometer scale) dictate sensing time, detection range, and signal transduction. At the bulk level, up to the millimeter scale, the assembly of nanostructures into organized films and coatings dictates whether sensing properties can be preserved when fabricating devices at scale. Additionally, at this scale, device form factors must be considered, which determine the biocompatibility and sensitivity in the case of implantable FET sensors.

In this work, I will address the challenge of structure control at multiple length scales using Tube-in-a-tube (Tube^2) nanostructures as a test platform. Tube^2 nanostructures are double-wall carbon nanotubes (DWCNTs) with heavily functionalized outer walls and semiconducting inner walls. This combination enables the use of outer wall surface chemistry modifications to address chemical selectivity and ionic screening challenges, while preserving the electrical transport properties of the inner wall for sensitive signal transduction.

CHEMICAL SENSING WITH A TUBE-IN-A-TUBE NANOSTRUCTURE

by

Benjamin Kerr Barnes

Dissertation submitted to the Faculty of the Graduate School of the
University of Maryland, College Park, in partial fulfillment
of the requirements for the degree of
Doctor of Philosophy
2022

Advisory Committee:
Professor YuHuang Wang, Chair
Professor Ian White
Professor Ichiro Takeuchi
Professor John Cumings
Professor Mohamad Al-Sheikhly

Acknowledgements

I would like to thank Dr. YuHuang Wang for his advice and assistance with my PhD research, as well as my committee members for generously giving their time and expertise in support of my dissertation. I also thank my co-workers in the Wang Lab who have provided practical help and useful discussions over the years, especially Dr. Peng Wang, Ziyi Wang, and Dr. James Wu, as well as the UMD FabLab and Surface Analysis Center staff for their advice and instruction. Finally, I would like to thank my family and close friends for their support during my studies.

I would also like to thank the funding sources that have supported the research in this dissertation, including the National Institute of General Medical Sciences through R01GM114167, the National Science Foundation through grant number CHE1904488, and the Air Force Office of Scientific Research award through the Multidisciplinary University Research Initiatives FA9550-16-1-0150. Additionally, the National Science Foundation funded the shared AFM used extensively in this work through the MRI Program grant number CHE1626288.

Table of Contents

List of Tables

List of Figures

List of Abbreviations

ADC: Ammonium deoxycholate

ATP: Polymer aqueous two-phase separation

AFM: Atomic Force Microscopy

CSA: Chlorosulfonic acid

DNA: Deoxyribonucleic acid

DOC: Sodium deoxycholate

DWCNT: Double-walled carbon nanotube

DX: Dextran

FCCVD: Floating catalyst chemical vapor deposition

FET: Field-effect transistor

I_{SD}: Source-drain current

λ_D: Debye length

LPDI: Length polydispersity index

L_{avg}: Number-averaged length

L_l: Length-averaged length

MES: 2-(N-morpholino) ethanesulfonic acid

NIR: Near-infrared

PBS: Phosphate buffered saline

PEG: Polyethylene glycol

PL: Photoluminescence

RNA: Ribonucleic acid

SARS-CoV2: Severe acute respiratory syndrome coronavirus 2

S2E: Superacid-Surfactant Exchange

SC: Sodium cholate

SDS: Sodium dodecyl sulfate

SEM: Scanning Electron Microscopy

SIP2: Suspended individualized parallel pathways

SWCNT: Single-walled carbon nanotube

TFT: Thin Film Transistor

Tube^2: Tube-in-a-tube nanostructure

UV: Ultraviolet

vis: Visible

$\mathbf{V_{SD}}$: Source-drain voltage

$\mathbf{V_{GS}}$: Gate-source voltage

Chapter 1: Introduction

Sections 2 and 3 of this chapter are adapted from a published manuscript:[1]

Peng Wang, Benjamin Barnes, Zhongjie Huang, Ziyi Wang, Ming Zheng, YuHuang Wang. "Beyond Color: The New Carbon Ink," *Advanced Materials*, **2021**, 33, 46. P.W. and B.B. contributed equally to this work.

1.1 The scope of this dissertation

Field-effect transistor (FET) chemical sensors are attractive for medical diagnosis and *in vivo* detection since they can be sensitive, potentially scaled down to small sizes, and modified with different probes to target a wide variety of biomarkers. However, some fundamental limitations have thus far prevented the widespread use of such FET chemical sensors. Firstly, the biosensor must be capable of detecting trace analytes quickly (on the order of minutes or seconds), which is challenging due to diffusion limitations. Secondly, for many applications the sensors must be able to detect biomolecules in physiological ionic strength conditions such as those present in blood, saliva, or cerebrospinal fluid, which is difficult since ionic screening in these solutions dampens the electrostatic charging that is needed to generate a signal. An additional challenge is to scalably fabricate FET chemical sensors without compromising their sensing properties. Finally, there is great promise for *in vivo* biosensing applications, such as real-time neurotransmitter detection, but such applications require mass-produced FET chemical sensors with new flexible, biocompatible, and small form factors that are currently not available.

In this work, I will address these challenges using Tube-in-a-tube (Tube^2) nanostructures as a test platform. Tube^2 nanostructures are double-wall carbon nanotubes (DWCNTs) with heavily

functionalized outer walls.[2,3] Unlike single-wall carbon nanotubes (SWCNTs) and graphene, functionalization of the outer wall does not negatively impact the electrical properties of the nanostructure since the inner wall remains intact and acts as a pristine electrical pathway. This enables the use of outer wall selective functionalization to address chemical selectivity and ionic screening challenges, while still taking advantage of the electrical transport properties of the inner carbon nanotube for sensitive signal transduction.

The key to addressing these diverse challenges with Tube^2 nanostructures is achieving structure control at multiple length scales from 10^{-9} m to 1 m (Figure 1-1). I will use length sorting of Tube^2 nanostructure to achieve single-particle (10^{-9} m) structure control for improved electrical and optical properties, few-particle (10^{-6} m) control in new device architectures to address the sensitivity and diffusion challenge, ensemble (10^{-3} m) control by developing a new self-assembling Tube^2 gel to achieve the scalable fabrication of biosensors, and finally structure control at the bulk (1 m) level to scalably fabricate a new fiber-based FET chemical sensor for neurotransmitter detection.

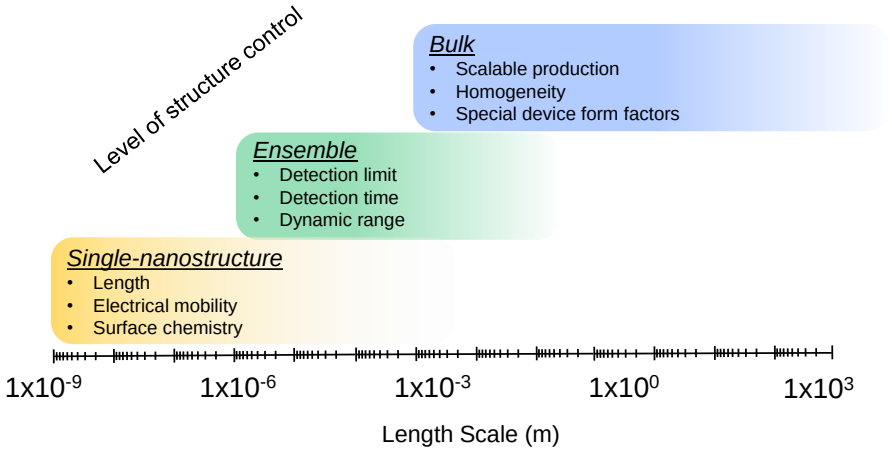

Figure 1-1. Structure control of Tube^2 semiconductor sensors at multiple length scales can be used to address many fundamental challenges in chemical sensing.

Chapter 1 summarizes the physical properties of carbon nanotubes, their applications in chemical sensing, and the specific fundamental challenges facing their broader implementation in chemical detection. In Chapter 2, I introduce experimental results showing the structure control at the individual particle level by separating ultralong DWCNTs for use in chemical sensors. The process enables extraction of ultralong DWCNTs and SWCNTs of up to 18 μm, facilitating the fabrication of chemical sensors and FETs with high electrical mobility. In Chapter 3 I use structure control at the few-particle level to address the competing speed/sensitivity problem with a new sensor architecture consisting of long Tube^2 nanostructures organized in parallel spanning a trench in the substrate. This device design enables a 6-orders of magnitude improvement in the detection limit for oligonucleotide biomarkers compared with films of short randomly oriented Tube^2 nanostructures, while retaining a rapid detection speed of only a few seconds due to the surface area of the suspended parallel nanostructures. Additionally, this device enables biomarker detection in physiological conditions because of the high density of probes on the Tube^2 surface which act locally as a screen for ions. In Chapter 4 I introduce a new printing technique that enables for the first time, high throughout fabrication of aligned and suspended SWCNT and DWCNT devices, providing unprecedented structure control at the ensemble level. This technique is facilitated by a pH-tuned surfactant liquid crystal ink to control the morphology of printed nanotube films. I use the technique to print batches of disposable sensors for detecting picomolar DNA and SARS-CoV-2 RNA targets. In Chapter 5 I demonstrate a new fiber FET chemical sensor that is highly flexible, and mechanically durable, providing structural control at the macroscopic level. This probe can monitor the activity of multiple neurotransmitters in real time. Finally, in Chapter 6 I provide an outlook for the future studies and technological advances enabled by the work in this dissertation.

In summary, I demonstrate in this dissertation that Tube^2 nanostructures can be used as a test platform for addressing the fundamental challenges in chemical detection including simultaneous high sensitivity and rapid detection speeds, while demonstrating new device form factors and fabrication strategies for the scalable production of high-performance chemical sensors. All of these advances come from structure control at multiple length scales, from controlling length at the individual nanoparticle to the meter-scale fabrication of devices with new self-assembly techniques. In addition to providing key technological breakthroughs in chemical sensing and advanced manufacturing, this work addresses fundamental scientific topics of charge screening, biomolecule diffusion, and nanoparticle self-assembly.

1.2 Physical and electrical properties of carbon nanotubes

Nanocarbons are a diverse family of nanomaterials with exceptional physical and chemical properties depending on their specific structure. These materials can be fully conjugated or non-conjugated (as well as partially conjugated). Conjugated nanocarbons include, most notably, quasi zero-dimensional fullerenes,[4] one-dimensional carbon nanotubes,[5,6] and two-dimensional graphene.[7] A SWCNT can be conceptually viewed as a seamless cylinder rolled from a slice of graphene. Similarly, a DWCNT consists of exactly two SWCNTs in a nested configuration (Figure 1-2a). These carbon allotropes feature a fully conjugated π-electron system of bonded sp^2 carbon atoms. Depending on the structure, DWCNTs and SWCNTs can possess properties to an extraordinary scale in terms of electrical conductivity[8] and field-effect mobility.[9,10] The structure of a SWCNT, known as its chirality, can be uniquely indexed by a pair of integers (n,m), which is defined by the rolling-up direction of a graphene sheet. Both graphene and SWCNTs are atomically thin, featuring a surface area as large as $\approx 2600\ m^2\ g^{-1}$, which is useful for achieving chemically functional surfaces and electrical percolation in printed structures.[11]

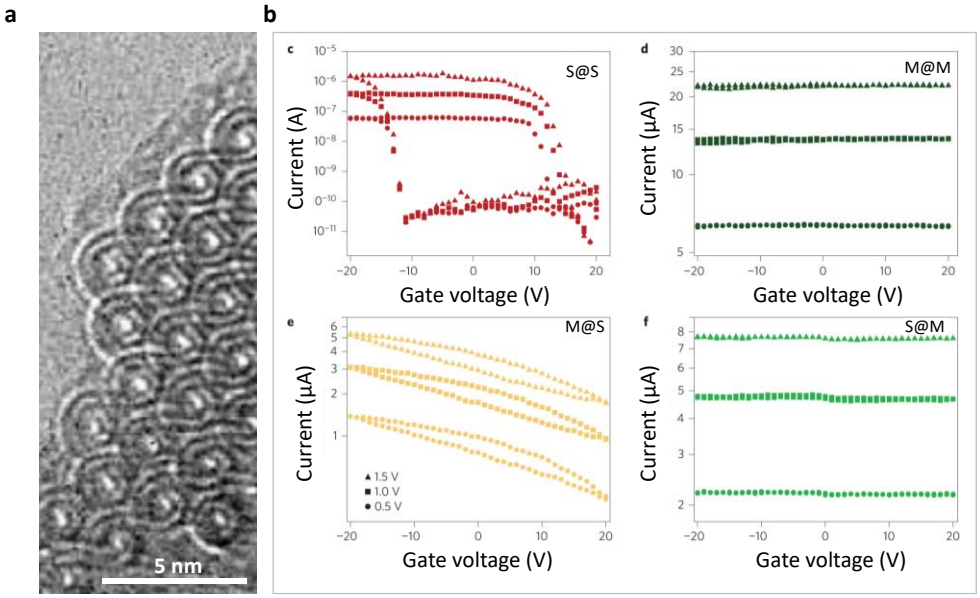

Figure 1-2. Structural and electrical properties of DWCNTs. a) Transmission electron microscope image of a bundle of DWCNTs showing the nested structure. Figure adapted with permission from reference[12]. b) DWCNTs exhibit metallic or semiconducting electrical properties depending on the bandgap of the inner and outer walls. Figures adapted with permission from reference[9].

Carbon nanotubes have demonstrated extraordinary electrical transport properties. An individual SWCNT can reach the ballistic conductance limit of $4e^2/h$ over the μm length scale, where e is the electron charge, and h is Planck's constant.[10] Ballistic conductance occurs when the mean free path of the electron surpasses the length scale of the conductor. In this condition, the contribution of electron scattering to resistivity becomes negligible and the device resistance is limited only by the contact resistance.[10] Besides this high conductance, SWCNTs are further endowed with large current-carrying capacities, far surpassing those of traditional metals, such as copper and gold.[10,13,14] For example, metallic SWCNTs can reach a current density on the order of $\approx 10^9$ A cm-

^{2}, which is 8-orders of magnitude higher than traditional carbon ink materials, like amorphous carbon, and about 1-order of magnitude larger than gold nanowires.[15-17] Graphene similarly exhibits high electrical conductivity with a current density on the order of $\approx 10^{8}$ A cm^{-2}, the upper limit set by the intrinsic electron-phonon scattering in graphene.[18] This high conductivity and current density make graphene and carbon nanotubes attractive candidates for efficient and small-footprint printed electronics[19,20] and transparent conductive films.[8]

An important advantage of carbon nanotubes over graphene is the fact that they can be semiconductors, featuring high carrier mobility (up to 79 000 cm^{2} V^{-1} s^{-1} for individual SWCNTs)[21] and tunable bandgaps from $\approx$0 to $\approx$2 eV depending on the nanotube chirality.[22] Like bulk semiconductors, electrical transport in a carbon nanotube semiconductor can be electrically gated by the field-effect, with an ON-state conductance on the order of $\approx$7000 μA μm^{-1} and ON/OFF ratios approaching $\approx 10^{6}$ (Figure 1-2b).[9,10] These properties, together with the high carrier mobility, make both SWCNTs and DWCNTs[9] suitable for high performance FETs.

1.2 Challenges in FET chemical sensing

Carbon nanotubes can be used to create devices that are responsive to various chemical stimuli, such as biomolecules and ions, eliciting an electrical or photonic signal due to their intrinsic electrical and optical properties. This responsiveness can be used in chemical detection, environmental monitoring, and disease diagnosis. For such applications, carbon nanotubes can be incorporated into four basic types of devices, including electrochemical sensors, FET chemical sensors, chemiresistors, and optical sensors. The focus of this work will be on FET chemical sensors, as these have routinely achieved high sensitivity, and can be adapted readily to target a variety of biomarkers including DNA and RNA oligonucleotides, small molecules, ions, and proteins. FET chemical sensors utilize the spatial proximity of a target probe interaction to the

semiconducting channel to electrostatically gate the current flowing through the semiconductor.[23] This gating can be measured either as a shift in the threshold voltage of the semiconductor channel (determined by sweeping the gate voltage) or as a change in the source-drain conductance with the gate voltage set near the threshold value.

1.2.1 SWCNT chemical sensors

Semiconducting SWCNTs have enabled the development of high performance and small-footprint FET chemical sensors.[24-27] The high ON/OFF ratios and field-effect mobility both translate into enhanced sensitivity and amplified signal transduction. The most sensitive SWCNT chemical sensors have achieved single-molecule detection using enzyme (Figure 1-3a-b)[27] and oligonucleotide (Figure 1-3c)[28] probes in pristine buffers.

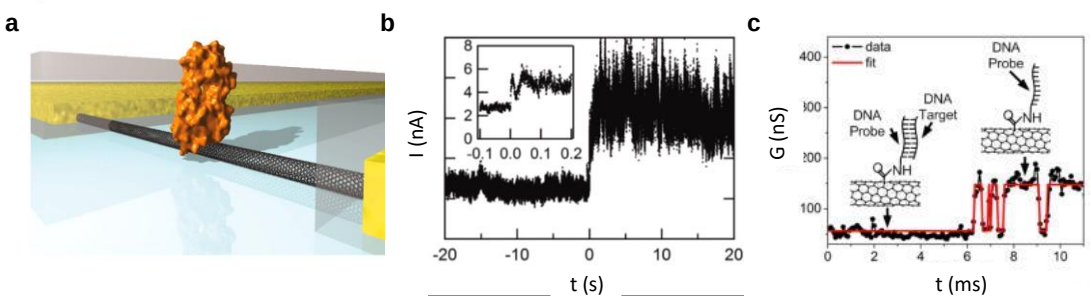

Figure 1-3. SWCNT FET chemical sensors can achieve extraordinary sensitivity. a) an isolated SWCNT with an enzyme probe attached is capable of single-molecule detection. b) Current as a function of time for the device in (a) shows individual binding events after the target molecule is introduces at 0 seconds. Figure adapted from reference [27]. c) A similar device architecture has been used to monitor DNA hybridization. Figure adapted with permission from reference [28].

Chemical functionalization provides a potentially powerful route to further control the structure and properties of nanocarbons in sensing applications such as by reacting them with diazonium salts in water or in chlorosulfonic acid[29,30] (Figure 1-4a) to provide attachment points for biomolecule probes. For sensing applications in complex environments such as blood or cerebrospinal fluid where interfering molecules may generate false positive signals by interacting with the exposed SWCNT sidewall, a high degree of functionalization would be needed. However, a high density of covalent functionalization comes at the cost of the SWCNT's electrical transport due to the disruption of the conjugated π-electron structure, thereby limiting its device applications (Figure 1-4b). DWCNTs provide a solution for addressing this tradeoff of chemical functionality and electrical properties.

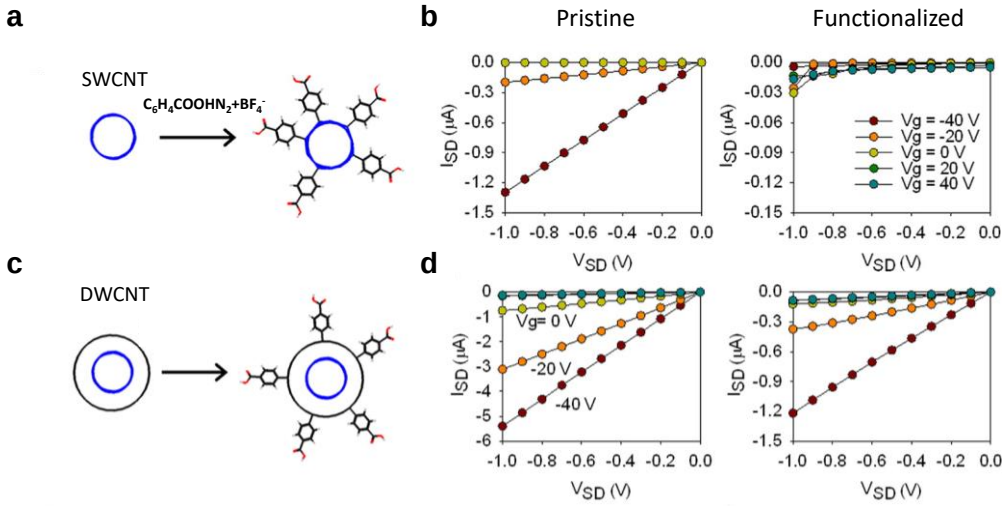

Figure 1-4. DWCNTs facilitate covalent surface modification. a) Schematic showing the covalent attachment of diazonium probes to the surface of a SWCNT. b) Electrical transfer curves before and after functionalization show that the semiconducting properties of the SWCNT are destroyed by the covalent functionalization. c) Schematic showing covalent attachment of probes to a DWCNT. d) Electrical transfer curves show that the DWCNTs retain their semiconducting properties after covalent functionalization. Figures adapted from reference [31] with permission.

1.2.2 Tube^2 chemical sensors

Since DWCNTs consist of nested SWCNTs, it is possible to chemically modify the outer wall while the inner SWCNT remains protected (Figure 1-4c). By such outer wall-selective covalent functionalization,[3,31] we can add chemical functionality to the surface while maintaining the structural integrity and thus the electrical properties of the inner-tube (Figure 1-4d), creating a Tube^2 nanostructure.[3] Since Tube^2 nanostructures largely bypass the problem of probe density vs. signal transduction seen in SWCNT-based sensors, they are a useful tool for chemical sensing studies.

In a Tube^2 nanostructure, the semiconducting inner wall and outer wall loaded with probes are separated by a van der Waals spacing of 0.37 ± 0.04 nm.[32] This close proximity of the probes to the semiconducting inner wall enables the probes to electrostatically gate the current passing through the device, a process we describe as "chemical gating" (Figure 1-5a).[3] The probes on the Tube^2 surface and ions in the surrounding solution equilibrate to form an electrolytic double layer around the Tube^2 structure. As target analyte molecules attach to the probes, they disrupt the ionic layers around the tube surface, electrostatically gating the inner wall.[3] This means that the gate voltage can be removed and sensing achieved with a simple 2-electrode configuration (Figure 1-5b). A previous study of this platform demonstrated nM sensitivity for DNA biomarkers with single mismatch selectivity while providing a signal of up to the µA range (Figure 5c).[3]

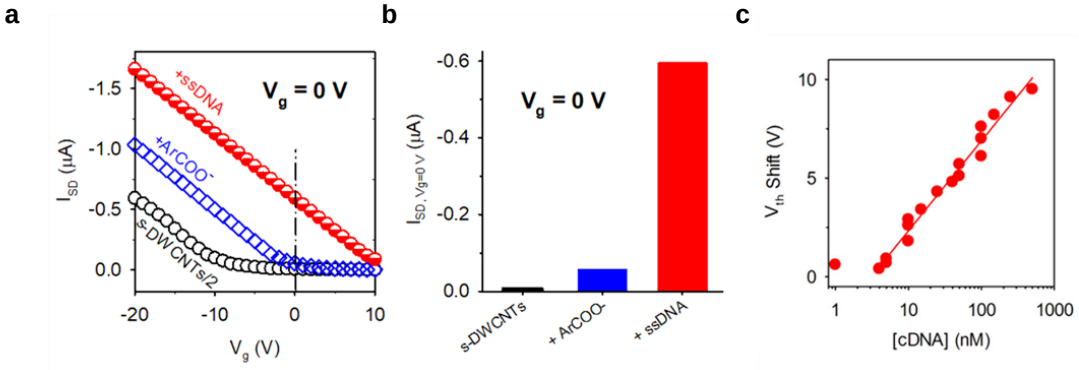

Figure 1-5. Chemical gating of a Tube^2 nanostructure. a) When target DNA hybridizes with probes on the Tube^2 surface, there is a shift in the threshold voltage of the device. b) The threshold voltage shift is sufficient to enable target molecule detection with no applied gate voltage. c) The threshold voltage shift can be correlated with the target DNA concentration. Figures adapted from reference [3].

One challenge facing the use of Tube^2 nanostructures in sensing applications is the lack of control over the length of the nanostructure. Previous Tube^2 chemical sensors have used ultrasonication-dispersed DWCNTs as the precursor. This dispersal process cuts the DWCNTs into short fragments which is undesirable since electrical mobility and conductance of carbon nanotubes decline as the length decreases.[33] I will address this issue in Chapter 2 by developing a superacid-surfactant exchange (S2E) protocol for rapidly extracting long fractions of DWCNTs and investigating the benefit of these longer nanostructure in sensing applications.

1.2.3 Sensitivity and detection time

A major challenge facing Tube^2 and FET chemical sensors is the simultaneous need for both sensitive and rapid detection. While target-probe interactions modulate the electrical signal in FET chemical sensors, the signal in a Tube^2 or other nanosensor can also be impacted by other phenomena, such as non-specific molecular interactions,[23] substrate charging, and crosstalk between adjacent nanostructures.[23] All of these phenomena can obscure target-probe interactions, limit the sensitivity of the device, and introduce noise and drift into the device behavior.[23] One approach to exclude these external effects is the use a single suspended carbon nanotube sensing element. While such devices are extremely sensitive, at low target concentrations it can take hours or days for target molecules to diffuse to the carbon nanotube surface due to the low surface area,

making this approach impractical for diagnosis.[34] To overcome this tradeoff, we will explore few-particle structure control with a new device design in Chapter 3 comprising multiple suspended individualized Tube^2 nanostructures that act as parallel electrical pathways (SIP2). The aligned and suspended nanostructure are freed from substrate contact for increased sensitivity, but collectively present a large surface area for rapid detection.

1.3.4 Detection in high ionic strength conditions

In order to generate a signal, FET chemical sensors require that a target-probe binding event occur within the Debye length of the conduction channel surface. This limitation is shared with all electrical biosensors including Tube^2 sensors, and is especially problematic for direct detection in biological samples, such as blood or cerebrospinal fluid, due to the shortened Debye length at high ionic strengths. The Debye length represents the maximum distance across which two charges can effectively interact and decreases with the inverse square root of the ionic strength of the solution. The Debye length in biological samples can be calculated using the formula below:[35]

$$\lambda_D = \frac{1}{\sqrt{4\pi l_B \sum_i \rho_i {z_i}^2}}$$

where l_B is the Bjerrum length, ρ_i is the number density of ionic species, and z_i is the charge of the ionic species. The Bjerrum length can be treated as a constant, as it is a function of the dielectric properties of the solvent.[35] The result of this calculation when using the salt concentrations in blood plasma[36] shows that the Debye length is only 0.78 nm, about the same length as two nucleotide bases. This means that traditional oligonucleotide probes of tens of bases long will stick up off the biosensor surface far beyond the Debye length. If the target binds with the probe at that distance, it will not generate a strong signal, if any at all.

Previous work has shown that sensing in high ionic strength conditions is possible only by using short dynamic probes, such as antibody fragments[37] and single-stranded DNA aptamers,[38 39] or using a screening layer made of hydrophilic polymers.[40] But these approaches require fragmentation, aptamer discovery research, and surface modification, respectively, reducing the broader applicability of the sensing platform. Tube^2 nanostructures open up new possibilities in probe design due to their chemically tunable surface which, as I demonstrate in Chapter 3, enable the formation of densely packed brush structures for enhanced sensitivity in high salt conditions.

1.3.5 Self-assembled carbon nanotube chemical sensors

Controlling the assembly of carbon nanotubes collectively into ordered structures is an additional challenge of structure control faced when implementing them into devices.[41] SWCNTs aligned in parallel exhibit excellent properties including high electrical mobility[42] which translates into improved chemical sensitivity in sensor applications. Some techniques exist for ordering carbon nanotubes into macroscopic structures, but these methods are limited by poor throughput,[43,44] high costs,[45,46] or the need for high processing temperatures[42,47] incompatible with commercial device fabrication.[48] In Chapter 4 I develop a liquid crystalline carbon nanotube gel that can be printed into ordered structures for high throughout fabrication of aligned and suspended devices that exhibit high chemical sensitivity for DNA and RNA biomarkers.

1.3.6 Chemical sensing in neural tissue

A recent area of interest for chemical biosensors is the detection of neurotransmitters in brain tissue. Inorganic semiconductor thin films have recently been used in a neural probe configuration to detect serotonin with aptamer probes.[49] An additional class of implantable sensors are those made from flexible and electrically functional fibers. In recent work,[50] such a device was made with 3-fibers: two fibers acting as the source and drain electrodes are connected with a polymer

semiconductor channel, and a third electrode, the gate, is made from dry-spun SWCNTs. Aptamer or enzyme coatings on the gate electrode can modulate the conductance of the semiconducting channel, generating signals in response to neurotransmitters.[51]

Currently, implantable chemical sensors are facing two challenges. Firstly, implants are limited by size, as a probe larger than about 50 µm can damage the surrounding brain tissue. It is difficult to fabricate implantable probes, especially with the 3 electrodes required for FET sensing, within such a small size constraint. A second challenge is to achieve multiplex detection, or detection of multiple target molecules simultaneously with one implant. In a conventional implantable probe, in order to achieve multiplexed sensing, it is necessary to chemically functionalize the separate electrode pairs on the probe with different biomolecular recognition elements.[49] Using small diameter carbon nanotube fibers, each chemically tailored to detect a different biomarker, and then tightly wound together is a promising approach, and has been recently explored for the intravenous detection of H_2O_2, prostate specific antigen, Ca^{2+}, and glucose,[52] but not yet for neurotransmitters. In Chapter 5 I will introduce a new device fabrication route for the production of flexible, 10 µm diameter FET fibers using thin films of carbon nanotubes and Tube^2 nanostructures.

1.2 Conclusions

The rich properties of Tube^2 nanostructures, especially their electrical properties and chemical functionality make them promising candidates for addressing fundamental challenges in chemical sensing applications. However, some key scientific and technical challenges remain in achieving their optimal performance merits. These challenges addressed in this dissertation, include achieving simultaneous high sensitivity and low detection time, sensing in physiological ionic strength conditions, achieving scalable device fabrication, and overcoming form factor constrains for implantable sensors. Addressing these challenges is possible with precise structure control at

multiple length scales from the single particle to the bulk level. This control coupled with Tube^2 properties reveals a promising future in chemical sensing applications, such as low cost and rapid medical diagnosis and *in vivo* neurotransmitter detection.

Chapter 2: Self-sorting of 10 μm Long Single-Walled Carbon Nanotubes in Aqueous Solution

This chapter is adapted from a published manuscript:[33]

Peng Wang, Benjamin Barnes, Xiaojian Wu, Haoran Qu, Chiyu Zhang, Yang Shi, Robert J. Headrick, Matteo Pasquali, YuHuang Wang. "Self-sorting of 10 μm Long Single-Walled Carbon Nanotubes in Aqueous Solution." *Advanced Materials*, **2019**, 31, 33.

B.B. assisted with FET device fabrication and adapted length sorting procedures for double wall carbon nanotubes.

2.1 Introduction

Single-walled carbon nanotubes (SWCNTs) are one-dimensional nanomaterials that feature extraordinary optical,[53] electronic,[10,54,55] and mechanical properties[55,56] depending on chirality and length. The last decade has witnessed significant progress in post-synthetic sorting techniques for separating SWCNTs based on their chiralities and electronic types.[57-60] In addition to chirality, nanotube length is another critical factor that governs the properties of SWCNTs and hence the performance of SWCNT-based devices. While short and ultrashort SWCNTs are preferable for bioimaging and drug delivery purposes,[61,62] electrical, mechanical, and many other optical applications require long nanotubes. For electronic applications, when assembled into macroscale objects, short tubes lead to high resistance, low on-currents, and low carrier mobility.[63] The mechanical properties of macroscale aligned objects are determined by inter-nanotube friction, which scales with CNT length and limits the tensile strength far below that of an individual tube.[64,65] Optically, short nanotubes typically fluoresce less brightly than long nanotubes due to

the quenching of excitons at the nanotube ends. In extreme scenarios, unfunctionalized ultrashort nanotubes with lengths of less than ~100 nm completely lose their intrinsic fluorescence.[66,67] To this end, sorting SWCNT mixtures by length is an important step to harness the full potential of electrical, mechanical, and optical properties of these remarkable nanomaterials.

Several length sorting techniques including size exclusion chromatography,[68] density gradient ultracentrifugation,[69] cross-flow filtration,[70] and polymer precipitation[71] have been reported. However, the sorted nanotubes are still short due to the ultrasonication at the initial sample preparation step, which cuts long SWCNTs into smaller pieces. The longest portion attained thus far has an average length (L_{avg}) less than ~1.5 μm[72] and a considerable population (~35% to ~75%) are short nanotubes (<500 nm).[68,70] Moreover, all of these length sorting methods have relatively low throughput. Therefore, it remains an unmet challenge to obtain long SWCNTs in a scalable manner and study their collective properties.

In this work, we demonstrate that the sorting of ultralong nanotubes (>10 μm) can be realized by "self-sorting" in aqueous solutions. In contrast to other reported mechanisms, which all rely on SWCNT interactions with other media, such as gels,[68,73] density gradients,[69] porous membranes,[70] or polymers,[71] the separation here occurs solely due to the length-dependent interactions between the SWCNTs themselves. This process is highly scalable, yielding a significant fraction (~10% based on atomic force microscopy measurements after the 6th sorting cycle) of ultralong (>10 μm) nanotubes featuring a narrow distribution. Importantly, the sorted SWCNTs are individually stabilized in water without additives, such as density gradient media, making them well compatible with established aqueous-based SWCNT sorting (e.g., by diameter, electronic type, or chirality) and other processing methods, allowing us to produce aligned thin films from long SWCNTs with high semiconducting purity (> 99%). We further demonstrate that thin film transistors (TFTs)

fabricated from these films exhibit a current ON/OFF ratio of more than 1000 with the carrier mobility exceeding 90 $cm^2 \cdot V^{-1} \cdot s^{-1}$, which is ~10 times better than short tube controls, exceeding the conventional TFT materials such as organic semiconducting polymers (<1 $cm^2 \cdot V^{-1} \cdot s^{-1}$),[74] nanocrystalline silicon (~50 $cm^2 \cdot V^{-1} \cdot s^{-1}$)[75] and approaching that of polycrystalline silicon TFTs (~100 $cm^2 \cdot V^{-1} \cdot s^{-1}$).[21,76]

2.2 Materials and methods

2.2.1 Dispersion of SWCNTs by S2E

EC 1.5 SWCNTs were obtained from Meijo Nano Carbon Co., Ltd. The SWCNTs (20 mg) and $ClSO_3H$ (20 mL; Sigma Aldrich, > 99%) were mixed and stirred at 1200 rpm with a magnetic stir bar for 3 days or until fully dissolved in a 100 mL round-bottom flask equipped with a ground-glass joint to prevent moisture from the air from entering the system. Prior to the S2E step, the mixture was diluted to the desired concentration using pure $ClSO_3H$. The SWCNT/CSA mixtures with various concentrations were then added dropwise into an aqueous solution of NaOH (0.75 M) and DOC (~0.08 wt/v%) (Sigma Aldrich, > 97%) with vigorous stirring so that the pH decreased to ~7-8. To achieve this pH condition, typically ~65 parts of NaOH-DOC are needed to neutralize one part of SWCNT/CSA mixture. (*Safety note: the neutralization process is aggressive and should be performed in a fume hood as a significant amount of heat and acidic smog can be generated. Personal protective equipment, including goggles/facial mask, lab coats, and acid-resistant gloves are also necessary.*) The solution was further stirred, followed by the addition of several drops of HCl (1 M) aqueous solution to protonate the DOC molecules, causing them to coalesce into dark grey/black precipitates along with the SWCNTs.[8] A 47 mm sized polyvinylidene fluoride filtration membrane was used to filter and collect the precipitates. The dark grey/black precipitates were then mixed with nanopure water and NaOH (1 M) was used to

tune the pH to ~7 to 8, and stirred for 1-3 days.[8] The resulting black solution was then centrifuged at 20,000 rpm for 1.5 h in a SW 41 Ti rotor using an Optima XE-90 ultracentrifuge (Beckman Coulter) to remove undissolved SWCNT bundles. For iterative S2E processes, the precipitated bundles were collected and sequentially rinsed with Nanopure™ water and isopropanol several times to remove the DOC surfactants. After drying in vacuum at 80 ^{o}C for overnight, the clean SWCNT bundles were weighed and re-dissolved in CSA to the desired concentrations (typically at ~70% concentration of the preceding cycles), followed by additional cycles of sorting. The last step of the length sorting process usually involves dissolving the longest nanotube precipitates in CSA at a sufficiently low concentration of ~0.1 mg/mL followed by S2E. Note that ~0.1 mg/mL was chosen as a tradeoff between the long length of SWCNTs with the final aqueous solution concentration.

2.2.2 Length Characterization of S2E-SWCNTs

SiO_2/Si substrates were first cleaned by rinsing with acetone, followed by functionalization with 3-aminopropyl triethoxysilane to facilitate the deposition of DOC-encapsulated S2E-SWCNTs. S2E-SWCNTs were then spin-coated on the functionalized substrates at 3000 rpm, rinsed by Nanopure™ water, and finally blown dry by Ar. To remove the surfactant and remaining organic solvents, we annealed the SWCNT-coated substrates at 300 ^{o}C in air for 15 mins. AFM topographical images were collected in the tapping mode using a Cypher ES AFM (Asylum Research Corporation) with AFM probes that are backside-coated with a thin layer of gold (Tap300GD-G, force constant = 40 N m^{-1}, Ted Pella). All the AFM images were analyzed using the Gwyddion software (version 2.53). The length of each curved SWCNT was measured by summing the lengths of multiple straight sections along the nanotube.

2.2.3 Capillary Thinning Extensional Viscosity Measurement

The diameter of the SWCNTs d was 1.52 ± 0.28 nm based on transmission electron microscope measurements (JOEL JEM 2100). SWCNT mass fraction was converted to volume fraction using the theoretical density of the SWCNTs (1.34 g/cm^3). The initial SWCNT length distribution was estimated by following a previously described study.[77] Briefly, the extensional viscosity of the CNTs dissolved in CSA at 117 and 181 ppm by volume was measured four times with capillary breakup extensional rheology using a Cambridge Trimaster capillary thinning rheometer. The extensional viscosity measurement was used to calculate the SWCNT viscosity average aspect ratio (L_v/d) = 5130 ± 130. The isotropic cloud point φ_{iso} was measured by imaging SWCNT solutions in flame-sealed glass capillaries (VitroTubes) with polarized light microscopy using a Zeiss Axioplan optical light microscope. Solutions were diluted until birefringence no longer appeared in the samples (74 ± 10 ppm by volume). The ratio of the experimentally measured isotropic cloud point φ_{iso} (volume fraction) to the theoretical value for monodisperse rigid rods $\varphi_{Onsager} = 3.34(L_v/d)^{-1}$ was used to estimate the polydispersity index $\sigma \sim 1.41$ and the L_{avg} was then calculated as ~4.5 μm.

2.2.4 Sorting S2E-SWCNTs by ATP

We mixed 1-part of the DOC stabilized SWCNT solution with 0.3-parts of 20% dextran (DX) and 0.3-parts of 50% polyethylene glycol (PEG) aqueous solution to yield ~0.2-parts of SWCNTs concentrated in the bottom DX-enriched phase after mild centrifugation at 4000 g for 60 s. DOC surfactants were then gradually replaced by a sodium cholate (SC) and sodium dodecyl sulfate (SDS) co-surfactant system following the reported procedure so that the final concentration of SC and SDS were 0.9% and 0.7%, respectively. Multiple cycles of this metallic/semiconducting SWCNT sorting process were applied until a desired purity of semiconducting SWCNTs was

reached. The PEG and DX polymers were further removed from the final semiconducting SWCNTs enriched solution by an ultrafiltration step using a centrifugal ultrafiltration tube (Amicon Ultra-15, PLHK Ultracel-PL membrane, 100 kDa).

2.2.5 Fabrication of TFTs and electrical measurements

To eliminate the potential influence of metallic SWCNTs and nanotube density on the measurement of the electrical properties, all semiconducting SWCNTs used were sorted by an identical ATP recipe and cycles and the SWCNT density in the fabricated devices was carefully adjusted to be equal. Solutions of the sorted semiconducting SWCNTs of different nanotube lengths were filtered through a 0.025 μm nitrocellulose membrane (Merck Millipore Ltd.) to form a thin film consisting of a random SWCNT network. Films consisting of aligned SWCNTs were fabricated following a reported procedure.[78] Heavily n-doped silicon wafers (Silicon Quest International) with a 300 nm thermally grown SiO_2 layer were used as the back-gated substrates. SWCNT thin films were placed on the SiO_2 substrates with compressed force and annealed at 95 ^oC so that the films were firmly attached to the substrates. An organic solvent (acetone or chloroform) bath was used to totally dissolve and remove the filter membrane. The substrates were then annealed in Ar at 300 ^oC to increase the adhesion with SWCNTs. Standard bilayer photolithography using LOR-5B as the sacrificial layer and Shipley 1813 as the photoresist was used to define the patterns for electrode deposition (channel length and width were 15 and 35 μm, respectively). Titanium (5 nm) and palladium (30 nm) were subsequently deposited on the Si wafers by Ebeam deposition (Angstrom NexDep Ebeam evaporator). After a standard lift-off procedure, another bilayer photolithography process was used again to remove undesired SWCNTs by oxygen plasma etching so that the adjacent transistors were electronically isolated. Electrical measurements were performed on a Keithley 4200-SCS probe station.

2.2.6 Spectroscopic and microscopic characterization

Ultraviolet-visible-near-infrared (UV-vis-NIR) absorption spectra of the S2E-SWCNTs supernatant after centrifugation were measured using a Lambda 1050 (Perkin Elmer) spectrometer with a broadband InGaAs detector. The resonant Raman spectra of the ATP-sorted SWCNTs was measured by a LabRAM ARAMIS Raman microscope (Horbia Jobin Yvon) with three different excitation laser sources (532 nm, 633 nm, and 785 nm). SEM images were collected by a SU-70 SEM (Hitachi). For PL microscopy measurements, the semiconducting enriched long SWCNTs after ATP sorting were drop cast onto Si wafers coated with gold (50 nm, Ebeam deposition) and followed by a polystyrene layer (50 nm, spin coating). Single nanotube PL imaging was performed on an IR optimized Olympus LCPLN100XIR objective (100x NA 0.85) and a liquid-N_2 cooled (-190 ^{o}C) two-dimensional InGaAs detector (Cougar 640, Xenics, Inc.). SWCNTs were excited with a collimated, 730 nm diode laser (Shanghai Dream Lasers Technology) at a power density of 50 W/cm^2.

2.3 Results and discussion

2.3.1 Role of SWCNT concentration on self-sorting in chlorosulfonic acid

We start this self-sorting process by dissolving raw SWCNT materials into chlorosulfonic acid (CSA, a superacid), followed by adding the SWCNT/CSA dispersion into an aqueous solution containing sodium deoxycholate (DOC) as the surfactant and sodium hydroxide (NaOH; see the Experimental Section for details). The aqueous dispersion is then centrifuged to separate bundled nanotubes from those individually dispersed in the supernatant.

SWCNTs spontaneously dissolve in CSA to form an optically homogenous solution at high concentrations (~0.61 vol%, or ~8.8 mg/mL).[79] In this superacid, SWCNTs behave as a weak base that can be protonated. The protonation induces Coulombic repulsion between nanotubes, which

overcomes the strong tube-tube van der Waals interaction, allowing the SWCNTs to individually dissolve in the superacid to form a thermodynamically stable solution.[79] Unlike many other acids such as nitric acid,[80,81] nitric/sulfuric acid mixture[82] or hydrogen peroxide/sulfuric acid mixture,[83] which can oxidize SWCNTs, chlorosulfonic acid is a true solvent that dissolves SWCNTs without oxidation.[79,84] The sidewall protonation effect is completely reversible and the structures of SWCNTs can be fully recovered as evidenced by spectroscopy studies.[79,84,85] Once dissolved in CSA, the SWCNTs behave like rigid rods with ultrahigh aspect ratios (length/diameter, *L/d*). The phase behavior for rods of monodisperse length was first described by Onsager[86] and Flory,[87] then extended to polydisperse rods by Wensink and Vroege,[88] and finally applied to SWCNTs by Green.[89] These theories have been shown to well describe the SWCNTs dissolved in CSA, which are polydisperse in aspect ratio and exhibit distinct phase behavior at different concentrations.[79,90,91] At sufficiently low SWCNT concentration, the solutions are isotropic and all the SWCNTs freely rotate as Brownian rods. Increasing the SWCNT concentration beyond a critical value (the isotropic cloud point, φ_{iso}) leads to the formation of a nematic liquid crystalline phase that coexists within an isotropic phase. This transition into a biphasic system occurs as the SWCNTs sacrifice rotational entropy to maximize translational entropy. Further increasing the concentration beyond the nematic point (φ_{nem}) causes all of the SWCNTs to transit into a fully liquid crystalline nematic phase.

Both φ_{iso} and φ_{nem} are linearly related to the inverse aspect ratio of the rods (here $\varphi_{iso} = 3.29(L/d)^{-1}$ and $\varphi_{nem} = 4.19(L/d)^{-1}$) and these scaling laws have been applied to polydisperse CNT solutions[89] and confirmed experimentally.[77] Indeed, the polydispersity in aspect ratio of the SWCNTs leads to a self-partitioning of the longest SWCNTs into the nematic phase while the shortest nanotubes remain in the isotropic phase (Figure 2-1a). We have previously demonstrated that the CSA

molecules on SWCNTs can be spontaneously replaced by DOC molecules in a straightforward superacid-surfactant exchange (S2E) process to produce surfactant-stabilized individual SWCNTs.[8,85] In this context, we hypothesize that during S2E, the individual SWCNTs in the isotropic phase are maintained far apart from each other such that the DOC molecules can diffuse to their surfaces before re-bundling can occur as the CSA is neutralized. On the other hand, the SWCNTs in the nematic phase readily bundle and precipitate before DOC can stabilize them individually in the aqueous dispersion. Therefore, by tuning the SWCNT concentration, it should be possible to preferentially bundle long nanotubes during S2E because long CNTs concentrate in the liquid crystalline phase due to their higher excluded volume, and once bundled, they precipitate during centrifugation, leaving short SWCNTs individually dissolved in the aqueous solution (Figure 2-1b).

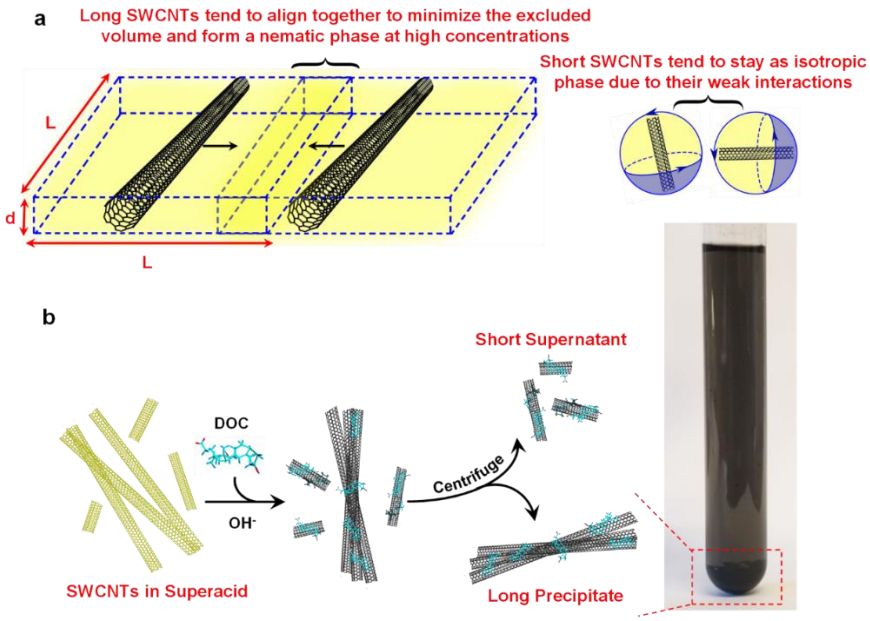

Figure 2-1. Schematic of the self-sorting process of ultralong SWCNTs. a) Long SWCNTs dissolved in CSA tend to align together to minimize the excluded volume (V) and form a nematic phase. The excluded volume scales with dL^2, where d and L are the SWCNT diameter and length respectively ($V \propto dL^2$). Short SWCNTs in superacid tend to stay in an isotropic phase due to their limited interactions. b) The SWCNTs are dissolved in superacid and subsequently neutralized with NaOH and DOC to produce short, individual nanotubes that are stabilized by surfactant in the aqueous solution. Meanwhile, long carbon nanotubes bundle and form precipitates, which can be separated from the dispersion by centrifugation.

We first studied the impact of SWCNT/CSA concentration on S2E to understand how it could potentially be employed to separate the nanotubes by length. Atomic force microscopy (AFM) was used to characterize the length distribution of the DOC-stabilized SWCNTs in the aqueous supernatant after centrifugation (see the Experimental Section for details). Figure 2-2a-e shows representative AFM topographic images of the SWCNTs as a function of the initial nanotube

concentration in CSA. At a high concentration of ~0.7 mg/mL, only short SWCNTs with an L_{avg} of ~0.1 µm were found in the supernatant. As the concentration decreases, we began to observe longer nanotubes in the supernatant, and at a dilute concentration of ~0.1 mg/mL, a maximum L_{avg} of ~3.1 µm was reached. Additionally, the height profiles of these AFM images unambiguously demonstrate that all the samples consist mainly of individual SWCNTs with diameters ranging from ~0.6 to 1.5 nm, indicating that SWCNTs are separated by length rather than the diameter or bundle size.

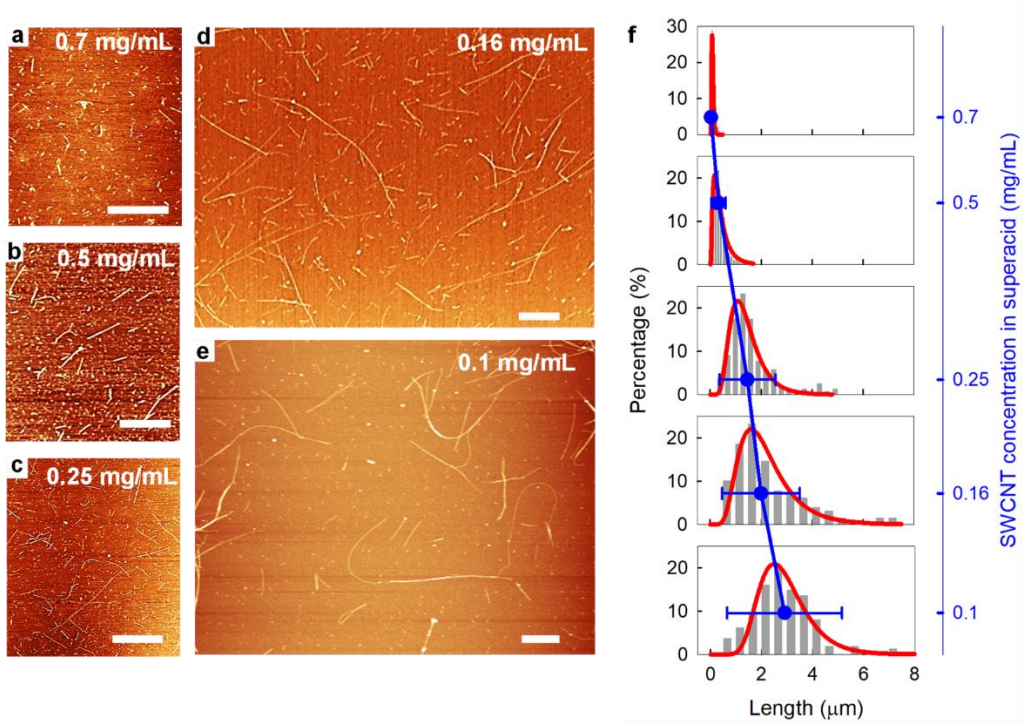

Figure 2-2. Length separation occurs effectively at different nanotube concentrations. a-e) Representative AFM images and f) corresponding length distributions (grey bars) of individual DOC-stabilized SWCNTs from decreasing SWCNT-CSA solution concentrations of ~0.70, ~0.50, ~0.25, ~0.16, and ~0.10 mg/mL, respectively. All scale bars are 1 µm. The distributions are fitted using log-normal functions (red lines). The average length of the DOC-stabilized SWCNTs increases as the concentration of SWCNTs in CSA decreases, as indicated by the blue line.

Analogous to the molecular weight polydispersity index in polymer physics, we calculated the length polydispersity index (*LPDI*) as a ratio of the number-averaged lengths (L_{avg}) and length average lengths (L_l) to quantify the length distribution (eq 2-1-3)[77]:

$$L_{avg} = \frac{\sum_i^N L_i}{N} \quad \text{eq 2-1}$$

$$L_l = \frac{\sum_i^N {L_i}^2}{\sum_i^N L_i} \quad \text{eq 2-2}$$

$$LPDI = \frac{L_l}{L_{avg}} \quad \text{eq 2-3}$$

LPDI is a unitless coefficient that enables the direct comparison of the length distribution of SWCNT samples regardless of their different L_{avg} values. We compiled the L_{avg}, L_l, and *LPDI* values of DOC-stabilized SWCNTs from different initial CSA concentrations in Table 2-1. A clear trend of increasing L_{avg} was observed as the SWCNT concentration in CSA decreases (Figure 2-2f). In addition, *LPDI* increased from 1.27 to 1.58, indicating that as the concentration of SWCNTs in CSA decreases, nanotubes of a wider range of lengths are stabilized as individual nanotubes during the S2E process.

Table 2-1. Correlation of L_{avg}, L_n, and *LPDI* of SWCNTs stabilized in the aqueous phase by S2E with the SWCNT concentration in CSA.

	SWCNT concentration in CSA (mg/mL)				
	~0.70	**~0.50**	**~0.25**	**~0.16**	**~0.10**
L_{avg} **(μm)**	0.11	0.41	1.53	2.13	3.10
L_n **(μm)**	0.14	0.59	2.29	3.28	4.84
LPDI	1.27	1.44	1.50	1.54	1.58

2.3.2 Sequential superacid surfactant exchange for selectively removing short SWCNTs

The strong inverse correlation between SWCNT/CSA concentration with the L_{avg} of DOC-stabilized SWCNTs motivated us to selectively remove the shorter nanotubes by lowering the initial concentrations stepwise. Through repeated application of this self-sorting process, followed by separation of the bundled (longer nanotube) component, and subsequent re-dissolution of this precipitate in the CSA to repeat the process at a lower concentration, we were able to successively reduce the population of shorter nanotubes in the precipitated material. SWCNTs were first dispersed at a high concentration (~0.7 mg/mL) so that only the shortest nanotubes were extracted from the bulk materials by the S2E process (defined as 1 cycle). The precipitates were then collected and re-dissolved into the CSA at a lower concentration (see the Experimental Section). Applying the same S2E process again, a portion of slightly longer SWCNTs were removed, further increasing the average length of the separated nanotubes. Since the overall length of the SWCNTs can be maintained throughout this iterative process, short nanotubes can be extracted repeatedly until a satisfactory long nanotube length is achieved.

Figure 2-3a-c shows representative AFM images of the sorted long tubes from the 2nd, 4th and 6th cycles of self-sorting. The removal of short nanotubes is clearly evident by the absence of nanotubes <1 μm in length. Moreover, the length distribution becomes progressively narrower (with a *LPDI* decreasing from 1.58 in the starting material to 1.30, approaching the ideal limit of 1) while the corresponding L_{avg} values increasing from an initial value of ~3.1 μm to ~3.3 μm after the 2nd cycle, and eventually to ~3.8 μm after the 6th cycle (Figure 2-3d). We note that a significant amount of ultralong nanotubes (>10 μm) can be easily found after 4 cycles. Figure 3-3e shows tiled AFM topography images of a ~12 μm ultralong SWCNT. Analysis of the AFM height profile

unambiguously confirmed that it is an individual nanotube with a diameter of ~1.2 nm (Figure 2-3f).

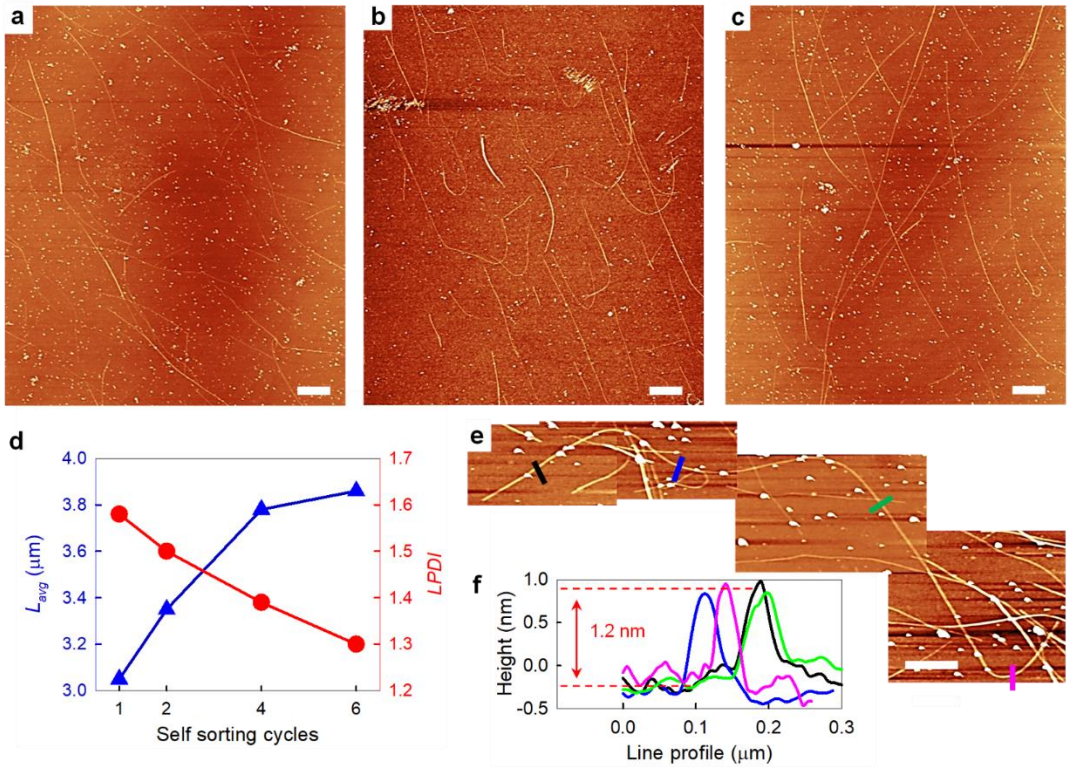

Figure 2-3. Ultralong SWCNTs from different iterations of the self-sorting process. a-c) Representative AFM images of individual, long SWCNTs separated after the 2nd, 4th, and 6th iterative S2E cycles. All scale bars are 1 μm. d) The L_{avg} and *LPDI* of the extracted DOC-stabilized SWCNTs as a function of the self-sorting cycles. e) Tiled AFM images of a 12 μm long SWCNT. Scale bar: 1 μm. f) Height profiles extracted along the nanotube, as marked in (e) by the black, blue, green, and purple lines.

2.3.3 Investigation of the phase behavior of SWCNTs in superacid

We further confirmed the concentration-dependent phase behaviors by cross-polarized microscopy (Figure 2-4a). Clearly, as the SWCNT concentration in the CSA decreases from ~0.7 mg/mL to ~0.1 mg/mL, the relative proportions of the nematic and isotropic phases changes, and the birefringent liquid-crystalline structures disappear completely at φ_{iso} ~0.1 mg/mL. When SWCNT samples with polydisperse length are dissolved in the CSA at a sufficiently high concentration, shorter nanotubes stay as isotropic individual rigid rods while longer nanotubes assemble into nematic ordered phases (Figure 2-4b). Therefore, when neutralizing a SWCNT/CSA solution at a concentration above φ_{iso}, only short nanotubes that stay as isotropic individual rods can be effectively converted into DOC-stabilized SWCNTs by S2E. As the concentration of SWCNTs in CSA decreases, longer SWCNTs partition in the isotropic phase, and eventually with the same S2E procedure, they can be "captured" by the surfactant molecules and stabilized as individual nanotubes in aqueous solution. The fitting between L_{avg} with SWCNT concentration in CSA (c) yield an exponential relationship of $c \propto {L_{avg}}^{-0.76}$, which closely follows the prediction from Onsager's Theory ($c \propto {L_{avg}}^{-1}$). We note the L_{avg} of the pristine sample measured by capillary thinning extensional viscosity[77] is ~4.5 μm, which is ~45% longer than the L_{avg} of ~3.1 μm for the DOC-stabilized SWCNTs before length sorting (see the Experimental Section for details). This discrepancy may be simply due to the approximations intrinsic in the extensional viscosity length determination, or may indicate that even at the optically dilute isotropic regime of ~0.1 mg/mL, ultralong tubes (>20 μm for instance) are still not well-stabilized by DOC molecules during the S2E process. Lowering the concentration of SWCNTs further in the CSA may allow the attainment of even longer SWCNTs by this self-sorting process.

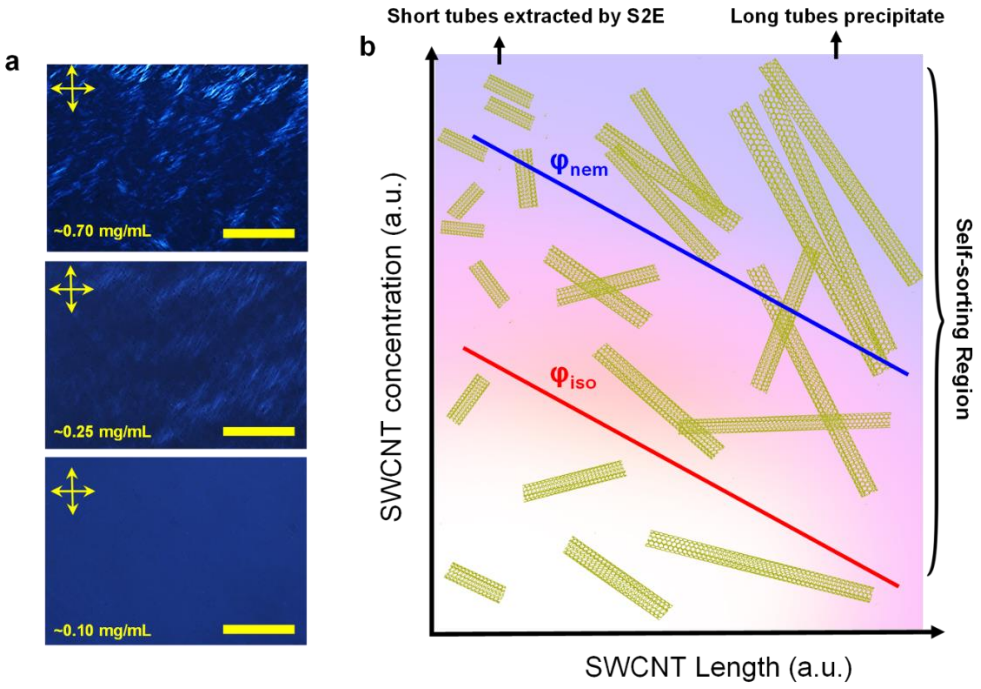

Figure 2-4. Proposed mechanism of the length dependent SWCNT self-sorting effect. a) Polarized light microscopy shows the solution morphology of SWCNTs at different CSA concentrations. The cross arrows indicate the relative orientation between the polarizer and analyzer. Scale bars: 200 μm. b) Phase behavior of SWCNTs in CSA solvent as a function of SWCNT length and concentration. The correlation of φ_{iso} and φ_{nem} with polydispersed SWCNT length are plotted according to the Onsager theory (axes are plotted in logarithmic scale). Above φ_{iso} the short tubes are selectively extracted by S2E while long tubes collapse into bundles.

Although our experiments unambiguously show that the observed "self-sorting" phenomena originate from nanotube phase separation in the CSA, directly centrifuging the SWCNT/CSA solution to separate the long nanotubes from the short ones does not work because the isotropic and nematic phases occur at very similar concentrations (about a factor of 1.5). Hence, the density difference and interfacial tension between the two phases are expected to be minimal. As a result,

the small density difference would make it difficult to separate SWCNTs of different length at low centrifugal force, and the low interfacial tension would allow the two phases to mix during centrifugation.

It is also interesting to note that the quality of the acid is another factor that can influence the length of the DOC-stabilized SWCNT fractions. By adding just 10% (by volume) of 98% sulfuric acid into the SWCNT/CSA solution to reduce the overall acidity of the system, we observed a significant reduction of the length of the DOC-stabilized SWCNTs after S2E. This observation is related to the previous studies showing that a reduction of the acidity of the solvent can effectively decrease the surface charges of the SWCNTs and downshift the φ_{iso}.[79] Decreased surface charges can be translated into reduced repulsive forces between nanotubes, which decreases the length cutoff for CNTs that transition into the nematic phase.

2.3.4 Ultralong SWCNTs for high mobility field-effect transistors

Because our long sorted S2E-SWCNTs are suspended in water, we can further purify the materials according to their electronic properties. We demonstrate this possibility by using the well-established aqueous two-phase (ATP) extraction method[92] with minimum modifications. An ATP system is comprised of two polymer-modified immiscible aqueous phases with slightly different hydrophobicities, which can spontaneously partition SWCNTs according to their electronic types and chirality.[60] Figure 2-5a shows a photo of three sorted fractions of long nanotubes with different chirality distributions, as indicated by the different colors of the solutions and their distinct UV-vis-NIR absorption spectra (Figure 2-5b). From the left to right in Figure 3-5a, the three solutions manifest different electronic properties and are categorized as metallic SWCNTs, large-diameter semiconducting SWCNTs, and small-diameter semiconducting SWCNTs. Photoluminescence (PL) microscopy was used to confirm the long length of the sorted semiconducting SWCNTs

enriched fraction (Figure 2-5c). We also used resonance Raman spectroscopy with different excitation lasers to further validate the enrichment of SWCNTs with specific electronic types after multiple cycles of ATP extraction.

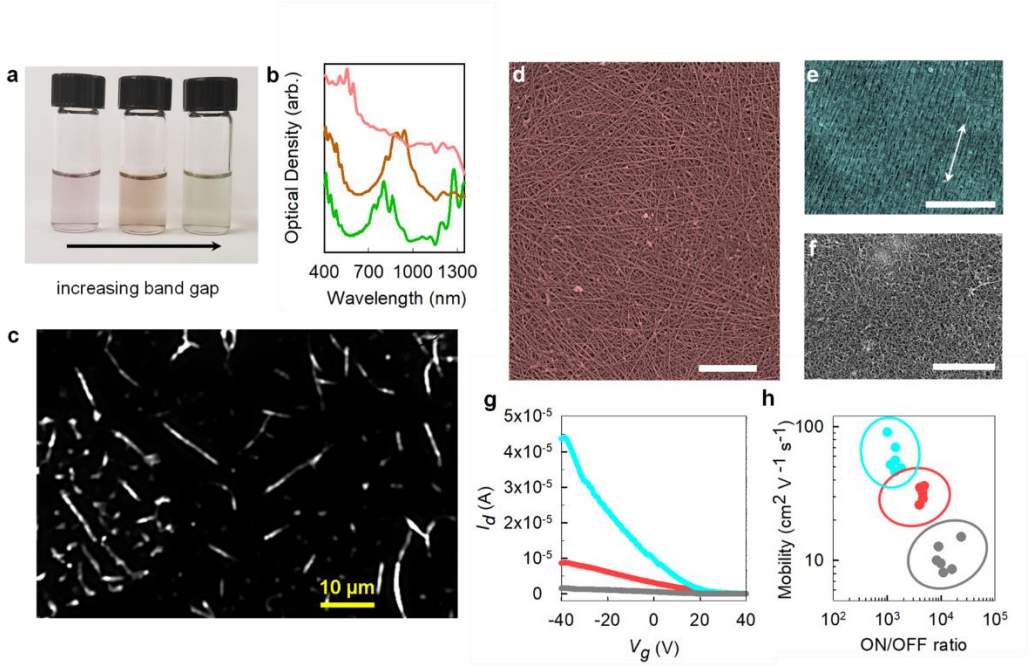

Figure 2-5. Sorting ultralong SWCNTs with specific electrical properties and their applications in TFTs. a) A photograph of aqueous solutions of chirality-sorted SWCNTs with increasing bandgaps by ATP. b) UV-vis-NIR absorption spectra of the 3 solutions shown in (a). c) A broadband (900–1600 nm) PL image of the sorted semiconducting DOC-stabilized SWCNTs. d-f) False-color SEM images of thin films fabricated from (d) random, long semiconducting SWCNTs, (e) aligned, long semiconducting SWCNTs, and (f) random, short semiconducting SWCNTs. All scale bars are 500 nm. g) Electrical transport characteristic curves and h) mobility *vs.* the current ON/OFF ratio of thin film TFTs fabricated from the random, long semiconducting SWCNTs (red, d), aligned, long semiconducting SWCNTs (cyan, e), and random, short semiconducting SWCNTs (grey, f).

To understand the influence of nanotube length and alignment on their macroscale electrical performances, we fabricated thin-film transistors from large-diameter semiconducting SWCNTs with different lengths and alignment, including aligned long semiconducting SWCNTs, random long semiconducting SWCNTs, and random short semiconducting SWCNTs (Figure 2-5d-f), in a back-gated configuration. Electrical transport characteristic curves and the plot of mobility *vs.* the current ON/OFF ratio of TFTs fabricated from different SWCNT films are shown in Figure 2-5g and Figure 2-5h, respectively. All TFTs showed similar p-type semiconducting behaviors with all ON/OFF ratios larger than 1000. However, TFTs fabricated from long aligned semiconducting SWCNTs show the highest mobility up to ~91 $cm^2 \cdot V^{-1} \cdot s^{-1}$ (average ~61.0 ± 15.6 $cm^2 \cdot V^{-1} \cdot s^{-1}$), while long random semiconducting SWCNTs and short random semiconducting SWCNTs exhibited much lower average mobilities of 30.1 ± 3.7 $cm^2 \cdot V^{-1} \cdot s^{-1}$ and 10.7 ± 2.4 $cm^2 \cdot V^{-1} \cdot s^{-1}$, respectively. To the best of our knowledge, the mobility from the long aligned semiconducting SWCNTs are among the highest values reported for SWCNT-based TFTs and is significantly higher than transistor devices made from soluble organic semiconductors (<1 $cm^2 \cdot V^{-1} \cdot s^{-1}$),[74] amorphous Si (~1 $cm^2 \cdot V^{-1} \cdot s^{-1}$) and nanocrystalline Si (~50 $cm^2 \cdot V^{-1} \cdot s^{-1}$),[75] even approaching that of p-type Si TFTs (~100 $cm^2 \cdot V^{-1} \cdot s^{-1}$).[21,76] The relatively low ON/OFF ratios (~1000-4000) of our multilayer thin-film devices can be explained by the charge screening effect, which is typically observed for relatively thick films of semiconducting nanotubes. Generally, the back-gate potential only has good control on the SWCNT-layer that is in contact with the dielectric. The charge carriers generated on this contact layer can screen the overlying SWCNT-layers, making it difficult for them to be fully turned off, resulting in higher off currents and lower ON/OFF ratios.[93,94] This charge screen effect can be circumvented by decreasing the film thickness. We therefore fabricated TFTs comprising a sub-monolayer of long random semiconducting SWCNTs. The ON/OFF ratio

increased up to ~22000 while the mobility remained at ~50 $cm^2 \cdot V^{-1} \cdot s^{-1}$. The output characteristic curves exhibit strong field-effect behaviors (I_d is linear under small V_d and saturated under large V_d), further indicating the electronic purity of our long semiconducting SWCNTs. Strategies for further improving the ON/OFF ratio include using SWCNTs with larger bandgaps,[93] using single-chirality semiconducting SWCNTs[95] or using high-κ dielectric materials.[94] Our study here shows that with long semiconducting SWCNTs as the channel material for long-channel TFTs, the mobilities of charge carriers can be improved by more than 10 times, demonstrating the significant influence of SWCNT-length on the performance of SWCNT-based TFTs.

2.4 Conclusions

In conclusion, we demonstrate that ultralong SWCNTs can be self-sorted by exploiting their length-dependent phase partitioning in solution, which depends on nanotube length. We obtained an L_{avg} ~3.8 μm with a narrow length distribution ($LPDI$ = 1.30), with a significant fraction of ultralong SWCNTs longer than 10 μm. We further sorted SWCNTs with different lengths into semiconducting and metallic fractions using aqueous two-phase extraction. TFTs fabricated from the long semiconducting nanotubes show ON/OFF ratios greater than 1000 and a significant improvement of carrier mobilities up to ~90 $cm^2 \cdot V^{-1} \cdot s^{-1}$, well-exceeding those of short semiconducting SWCNTs, organic semiconducting polymers or polycrystalline silicon. Our approach provides a pathway to attain ultralong SWCNTs with defined electrical properties, opening opportunities to significantly improve the transport properties and performance of SWCNT-based devices, such as TFTs and sensors.

Chapter 3: Parallel Field-effect Nanosensors Detect Trace Biomarkers Instantly at Physiological High Ionic Strength Conditions

This chapter is adapted from a submitted manuscript:

Benjamin Barnes, Peng Wang, YuHuang Wang. "Parallel field-effect nanosensors detect trace biomarkers rapidly at physiological high ionic strength conditions." ACS Sensors.

B.B. and Y.H.W. conceived the idea, designed experiments, and analyzed the data. P.W. sorted nanotubes and B.B. performed device fabrication, surface functionalization, electrical characterization as well as all the other experiments. B.B. and Y.H.W. wrote the manuscript with inputs from all authors.

3.1 Introduction

Chemical sensors that can detect trace biomarkers rapidly, without the need of specialized equipment or laboratory processing, will enable timely detection[96] and longitudinal monitoring of diseases at point of care[97] as well as real time probing of biomolecular functions.[98] However, such sensors must overcome three major technical challenges: 1) the sensor must be sensitive and selective enough to detect the target analyte of interest;[99] 2) the detection must be sufficiently rapid, preferably on the order of minutes or even seconds;[34] and 3) the sensor should ideally function directly in the high ionic strength conditions of biofluids such as whole blood and saliva to minimize requirement of sample processing steps[100] and more importantly, maximally preserve data relevance to the pristine physiological environment.[39] Additionally, such a device may allow real time probing of biofunctions and enable efficient transduction of biochemical—electrical signal at the bio-electronics interface.[101,102]

Nanostructured field-effect transistor (FET) chemical sensors typically work by electrostatically gating their semiconducting channels with charged target molecules.[103,104] The probe molecules, such as oligonucleotides and antibodies, which are attached to the surface of the semiconducting device channel, selectively capture the target biomarkers to create a change in the local electrostatic field that modulates the electrical current passing through the device. FET sensors based on individual single-wall carbon nanotubes (CNTs) have demonstrated ultrahigh sensitivity, in some cases reaching the single molecule limit.[27] However, due to their small surface area, these tiny sensors, whose diameters are merely ~1 nm, require extensive detection time (hours to days) to catch a target molecule at femtomolar concentrations.[34] In contrast, with a large sensor area, thin film FETs can significantly accelerate the speed of detection and additionally benefit from simplified fabrication.[23,101] However, the sensitivity of thin film FETs is typically much poorer than single nanotube FETs.[23] Furthermore, electrical screening quickly dampens the electrostatic gating effect beyond the Debye length (λ_D), which is merely ~0.8 nm in the high ionic strength conditions found in blood, saliva, or synovial fluid,[35,40] making it even more difficult to simultaneously achieve ultrahigh sensitivity and speed for electrical detection in pristine biofluids. Although there are clever tricks to circumvent some of these issues in specific use scenarios, this sensitivity-speed dilemma poses a fundamental challenge broadly impacting bioelectronics.

Here, we show that this sensitivity-speed challenge can be addressed by creating many nanoscale sensor pathways in parallel to simultaneously achieve ultrahigh sensitivity and instant detection, even under the physiological high ionic strength conditions (Figure 3-1). We assembled tube-in-a-tube semiconductors across a trench to form suspended individualized parallel pathways (SIP2) between a pair of gold electrodes. Each SIP2 consists of a single-wall CNT nested within another that is densely functionalized with oligonucleotide probes covalently attached to the sensor

surface. Electrical transport through the semiconducting inner tube is chemically gated by the target-probe interactions at the outer wall.[3] This tube-in-a-tube configuration provides a covalent functional layer that enables high selectivity and structural stability not possible with single-wall CNTs.[31] Since each SIP2 spans the electrodes individually, it acts as a distinct electrical pathway that is comparable to a single nanotube FET sensor, which has achieved single-molecule sensitivity.[27] By effectively increasing the sensor surface area with many of these nanosensors working in parallel, high speed of detection is realized while retaining the high sensitivity of individual single-wall CNT FET sensors. We note although parallel aligned nanostructures are not "new," all previous studies, to the best of our knowledge, do not reveal this simple scaling relation that we found with SIP2 for addressing these fundamental challenges in electrical detection. As a proof-of-concept application, we demonstrate the rapid detection of trace oligonucleotide biomarkers for Lyme disease, achieving instant detection with femtomolar sensitivity and two-mismatch selectivity, all directly at the physiological high ionic strengths.

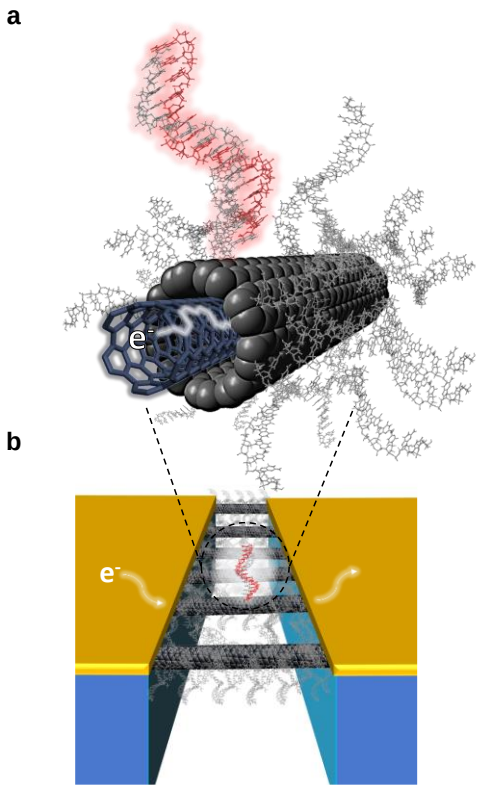

Figure. 3-1. Tube-in-a-tube field-effect biosensor with suspended and individualized parallel electrical pathways. (a) Schematic illustration of a single tube-in-a-tube semiconductor with the inner semiconducting single-wall CNT transporting charge carriers, and the outer wall densely functionalized with DNA probe molecules. **(b)** A schematic of the SIP2 device architecture, consisting of individualized tube-in-a-tube nanostructures aligned in parallel and suspended between two electrodes over a trench.

3.2 Materials and methods

3.2.1 Dispersing and sorting ultralong DWCNTs

Ultralong DWCNTs were separated from raw materials using a length self-sorting method as we previously reported.[33] Briefly, DWCNT powder (Cheap Tubes) was dissolved in chlorosulfonic acid (99%, MilliporeSigma) at a concentration of 1 mg/mL and then dispersed in 0.08 wt% sodium

deoxycholate (DOC, >97%, MilliporeSigma) and 0.75 M NaOH. The double-wall CNTs and sodium deoxycholate were precipitated by adding 37% HCl, typically 1-3 mL, to lower the pH to below the pKa of DOC (pH ~6.6), and then redispersed with 1 M NaOH (to raise the pH above 6.6) to a final surfactant concentration of 6 wt%. The suspension was centrifuged at 16400 rpm for 90 minutes to separate both long and short double-wall CNTs. The precipitated long double-wall CNTs were washed with Nanopure™ water and isopropanol, dried, and re-dissolved in chlorosulfonic acid at 0.7 mg/mL, after which the dispersal in sodium deoxycholate and NaOH was conducted again. The process was repeated 2 more times (for a total of 4 length sorting cycles) at DWCNT concentrations of 0.5 mg/mL and 0.1 mg/mL in chlorosulfonic acid respectively, to further enrich the population of long double-wall CNTs. The final DWCNT suspension contained 5 wt% sodium deoxycholate.

3.2.2 Diazonium salt synthesis

2-fluorobenzoic acid diazonium tetrafluoroborate was synthesized according to a previous procedure.[3] Briefly, 4.814 mmol of 4-amino-2-fluorobenzoicacid (TCI) was added to 3 mL of Nanopure water in a round bottom flask fully covered in aluminum foil to prevent light exposure, which was then submerged in an ice bath. Next, 2.68 mL of fluoroboric acid (48 wt%; MilliporeSigma) was added to the flask while stirring. 670 mg of sodium nitrite was dissolved in 2 mL of Nanopure water and added to the round bottom flask dropwise. The solution was stirred in the dark for 15 minutes, after which the solid product was collected on a PTFE filtration membrane and rinsed with ~100 mL of diethyl ether. The product was then dried in the dark for 20 minutes under vacuum and stored in the dark in a sealed vial at 0 ^{o}C.

3.2.3 Fabrication of aligned and suspended tube-in-a-tube semiconductors

Phosphorous-doped silicon wafers (1-10 Ωcm) with a 300 nm thermal oxide layer (University Wafer) were cleaned in piranha solution (3:1 by volume H_2SO_4:H_2O_2 (30 wt%)), rinsed copiously with Nanopure water and isopropanol, and finally blown dry with compressed nitrogen. Positive photoresist (Shipley 1813) was used to pattern dielectrophoresis electrodes with a 5 µm channel. A chromium/gold (10 nm/30 nm) bilayer was deposited using thermal evaporation at 10^{-7} torr. The excess metal was lifted off in Remover PG at 80 °C for 30 minutes. Before use, the electrodes were rinsed again with water and acetone and blown dry.

Pristine double-wall CNTs were deposited using a dielectrophoresis procedure[105] using the previously fabricated electrodes and the length-sorted aqueous suspension of double-wall CNTs in sodium deoxycholate, diluted 10x with Nanopure water. To obtain only a few individualized double-wall CNTs per device, we used the following dielectrophoresis parameters: 10 MHz, 5 V amplitude, and 1 - 4 minutes of applied voltage. After dielectrophoresis alignment, the device was coated with electron-beam resist (PMMA 495K) and a second pair of electrodes (top contacts) was defined on top of the previous electrodes using electron beam lithography (Raith e-line), which were 10 µm wide and separated by a 1 µm gap. Cr/Au (5/20 nm) was deposited over the patterned substrate, yielding a 1 µm channel in the final device with 2 µm of both ends of the double-wall CNTs buried beneath the top contacts. The top contacts prevent short double-wall CNTs that do not span the channel from contributing to electrical noise, as well as anchor the double-wall CNTs to keep them from collapsing during wet etching of the silicon wafer. The aligned double-wall CNTs exhibited low resistance and an ON/OFF current ratio of ~1 due to the presence of some metallic inner and outer carbon nanotubes. Raw double-wall CNTs typically consist of a mixture of semiconducting and metallic outer walls and inner walls. We partially etched away the substrate

oxide using 6:1 HF:NH_4F buffered oxide etchant to create a 120 nm deep trench in between the source and drain electrodes. Immediately after etching, the devices were dried using supercritical CO_2 (Tousimis).

The tube-in-a-tube semiconductor structures were synthesized *in situ* from the suspended double-wall CNTs using 2-fluorobenzoic acid diazonium salt by submerging the devices in 1 mM diazonium salt solution for 12 hours, followed by 10 mM diazonium salt for 12 hours. The reactions were conducted in the dark. After the reaction time, the devices were rinsed with Nanopure™ water to remove the unreacted diazonium salt.

The metallic inner carbon nanotubes were then destroyed using electrical breakdown. In this process, the source drain voltage was increased from 0 V until a sharp spike in resistance was observed, indicating that one metallic carbon nanotube was destroyed. Breakdown typically occurred between 10 and 20 V. This was repeated until the ON/OFF ratio reached 10–1000. What remained were individual pristine semiconducting nanotubes sealed inside insulating outer walls that are covalently grafted with a layer of aryl groups terminated with COOH functional groups.

We then covalently attached 30-base DNA probes with 5' amino termini (Integrated DNA Technologies) to the surface carboxyl groups on tube-in-a-tube semiconductor using a previous method.[3] See Table 3-1 the DNA sequences used in this chapter. Briefly, the carboxyl groups were activated in 0.4 mg/mL 1-ethyl-3-(3-(dimethylamino)propyl)carbodiimide and 1.01 mg/mL sulfo-N-hydroxysuccinimide in 10 mM MES (Covachem) for 15 minutes. Amino-terminated DNA probes were then attached to the activated groups by placing a droplet of 10 µM of DNA in 0.1X PBS (CovaChem, LLC) on the device. The DNA solution was replaced by pipette on the device every 15 minutes for 1 hour. The devices were then rinsed with Nanopure™ water and stored in 1x PBS (1x PBS was prepared by the instructions provided by CovaChem and consisted of 100

mM sodium phosphate and 150 mM sodium chloride) until characterization (within 1 day of fabrication).

Table 3-1. DNA sequences used in sensing experiments

Name	Sequence	Charges per molecule
Probe	5' AGTTTCACTCTTGCGAGCATACTCCCCAGG	29
Analyte	3' TCAAAGTGAGAACGCTCGTATGAGGGGTCC	29
2x Mismatch	3' TCAAAGTGAGAACGCTGGCATGAGGGGTCC	29
1x Insertion	3' CAAATGTGAGAACGCTCGTATGAGGGGTCC	29
2x Insertion	3' CAAATTGTGAGAACGCTCGTATGAGGGGTCC	30
Fully Mismatched	3' CAATTGTATAGGTTCAACCTCAATTAGAGATGGAACTTA CACCAGTTGTTCAGACTA	57

3.2.4 Electrical characterization

The I-V, transconductance, and sensing curves were collected using a Keithley 4200 Semiconductor Parameter Analyzer. Typical sensing experiments were conducted by placing a 10 µL droplet of the oligonucleotide analyte in PBS on the device channel and either sweeping the source-drain voltage between -1 V and 1 V, or by measuring the current over time with an applied bias of 0.5 V. No appreciable evaporation of the droplet was observed during the short testing period, and the temperature and relative humidity were maintained in the lab across all experiments. Noise was quantified by calculating the coefficient of variation of the current in buffer. Sensing measurements were always conducted from blank PBS to increasing analyte concentrations. Sensing curves were reported as the % change in current (with respect to the blank

measurement) at 0.5 V unless specified otherwise in the text. The device channel was not allowed to dry at any time during the sensing characterization.

3.2.5 AFM characterization

Freshly cleaved mica substrates were soaked in 1 M magnesium sulfate for 10 minutes, blown dry with compressed nitrogen, and rinsed with Nanopure™ water. The solution of length-sorted double-wall CNTs dispersed in sodium deoxycholate was then dropped onto the mica surface and allowed to incubate for 10 minutes, after which the droplet was blown away. The substrate was then rinsed with water and blown dry. The double-wall CNTs and tube-in-a-tube semiconductor nanostructures were characterized in tapping mode using a Cypher ES AFM (Asylum Research Corporation) with gold backside-coated AFM probes (Tap300GD-G, force constant = 40 N m^{-1}, BudgetSensors).

3.2.6 Raman characterization

Raman scattering was measured directly on SIP2 devices with a Horiba Aramis Raman microscope at an excitation wavelength of 532 nm. The Raman shift was calibrated with a silicon chip. A 50x microscope objective and line scan were used to collect up to 10 spectra from between the electrodes where the double-wall CNTs or tube-in-a-tube semiconductors located.

3.3 Results and discussion

3.3.1 Long DWCNTs form individualized parallel electrical pathways

We fabricated SIP2 sensors from long double-wall CNTs that are attainable only recently using a non-destructive dispersion technique followed by length self-sorting, as we previously reported[33] (see Methods for details). The double-wall CNTs used in this study have an average length of 1.85 μm, which is larger than a sonication control (0.44 μm), and 87% were longer than the trench width

(1 µm). We used dielectrophoresis[105] to align the double-wall CNTs across two gold electrodes patterned on silicon oxide. The CNTs are aligned individually between the source and drain electrodes, with the number of nanotubes (2 – 100 / device, up to 17 ± 3 pathways/µm) in each device consistently controlled through the magnitude and duration of the applied electric field (see Methods). We note that long CNTs were essential for achieving SIP2, while shorter CNTs resulted in disordered networks and did not fully span the gap between the electrodes. We attribute the improved alignment to a stronger dielectric force, which scales with the nanotube length, [105] that the longer double-wall CNTs experience compared with the short ones.

We then pinned the CNTs with gold top contacts, which define the source and drain electrodes, apart and etched the substrate oxide with buffered hydrofluoric acid to create a 120 nm deep 1 µm wide trench underneath the CNTs, which removes the substrate effect and maximizes the exposed surface area of the sensors (see methods for the fabrication details). We used a trench width of 1 µm, as this distance could be routinely spanned by individual CNTs without dangling ends and when combined with top contacts, reduces the risk of CNTs collapsing into the trench. We then chemically converted the double-wall CNTs into tube-in-a-tube semiconductors by covalently functionalizing their outer walls with 2-fluorobenzoic acid diazonium salt.[3] We note that the outer layer serves as a functional layer that is complete and non-permeable to small molecules as evidenced by the intactness of the inner tube under chemical attacks.[2] In this top-contacted configuration, the portion of the double-wall CNTs buried under the metal contact are protected from covalent functionalization allowing electrical contact to the tube-in-tube structure. The functionalization was followed by high voltage electrical breakdown of those with metallic inner tubes, as previously described,[106] leaving most semiconducting walls intact. Despite the high density of functional groups on the tube-in-a-tube semiconductor surfaces, the inner nanotube

remains chemically isolated from the outer wall-selective surface chemistry, therefore retaining its electrical conductivity.[2] This approach provides a key advantage over other nanomaterials like single-wall CNTs and graphene, whose electrical properties degrade when covalently functionalized to a comparable degree.[107]

3.3.2 Individualized parallel electrical pathways enable rapid detection of femtomolar targets

We investigated the sensing behavior of SIP2 through the electrical detection of model oligonucleotide biomarkers. We covalently linked the oligonucleotide probes (see Table S1 for the probe sequence) to the tube-in-a-tube semiconductors through the surface 2-fluorobenzoic acid groups using the well-established carbodiimide crosslinking reaction.[3] We note that when carbodiimide crosslinking is used, normally it brings complexity in the sensor and the distance between the target molecular and channel increases causing decrease in sensitivity. In our case, the initial gap between the linker and semiconducting inner wall is less than a nanometer, so the small distance added by the linker does not significantly impact sensitivity. The oligonucleotide target we chose for this demonstration was a 30-base segment of a DNA biomarker for *B. burgdorferi*, the bacterium that causes Lyme disease.[108] Prior to introducing the target molecules, we measured the current passing through the SIP2 device at a constant voltage bias of 0.5 V in 1X phosphate-buffered saline (PBS, containing 100 mM Na_3PO_4 and 150 mM NaCl) that mimics the high salt physiological ionic conditions to determine the background signal and electrical noise. We measured the coefficient of variance of the electrical current over time for 13 devices and determined the average electrical noise to be 0.90% ± 1.01%. This small noise possibly originates from the interaction of the DNA probes, or ions from the buffer, with the semiconductor surface. However, this noise level is significantly smaller than the signal generated by the target analytes (discussed below) which was as much as 70%, allowing for sensitive chemical detection.

To determine the response time of the SIP2 sensor, we introduced 5 fM of target DNA, also in 1X PBS, while applying 0.5 V across the source and drain electrodes. Within ~2 seconds of adding the target the device conductance increased by ~50% and stayed constant (Figure 3-2a). Of the 13 devices evaluated in this study, the response time was typically 1 to 15 seconds. While a rapid sensing response can also be achieved with randomly oriented Tube^2 films, the sensitivity of the SIP2 configuration is significantly enhanced by about 6 orders of magnitude. In contrast, calculations based on the diffusion model predict that at femtomolar concentrations it would take hours for the first molecule to reach the surface of a single single-wall CNT.[34] The rapid response we observed with SIP2 is largely enabled by the larger (> 20x) collective surface area, relative to a single single-wall CNT, of multiple long tube-in-a-tube semiconductor nanostructures acting in parallel, with additional contribution from the suspended structure which further increases surface area and enhances target-probe interactions. Finally, sensing in physiological ionic strength conditions lowers the energy threshold for target-probe DNA binding.

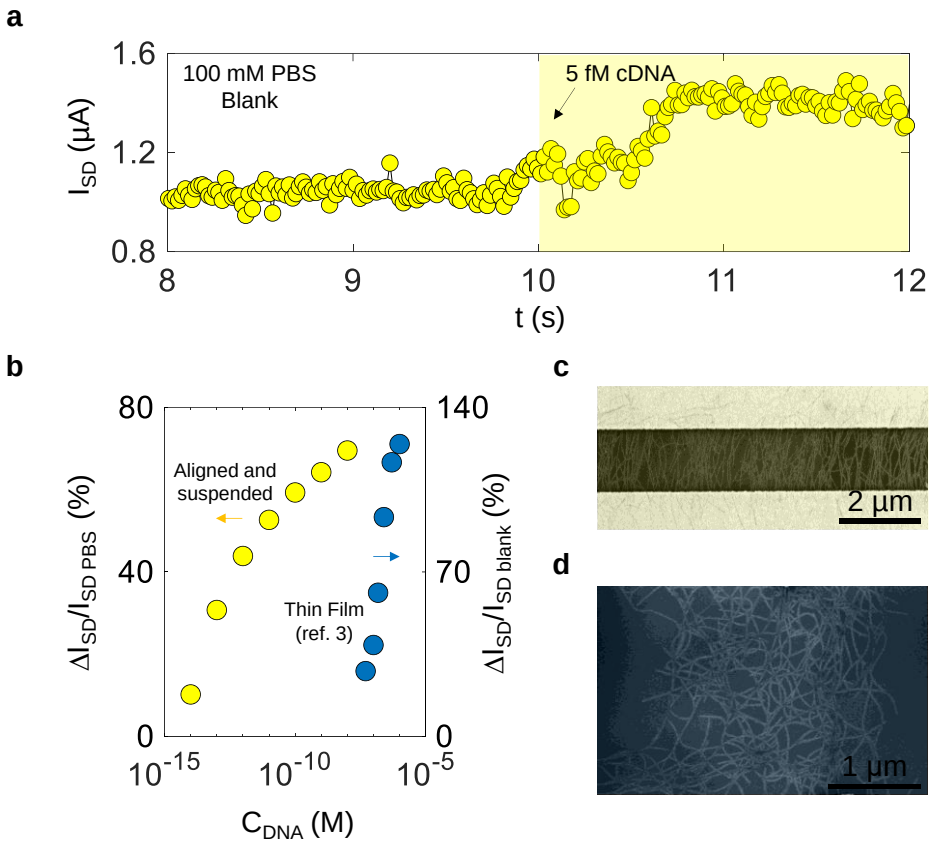

Figure 3-2. Electrical detection of an oligonucleotide Lyme disease biomarker. (**a**) Electrical current passing through the SIP2 device as a function of time at a constant voltage of 0.5 V. Note that addition of 5 fM oligonucleotide target at t=10 seconds led to an increase in the device conductance within just ~2 seconds. (**b)** Current response of a representative sensor showing the increasing conductance of the SIP2 device (yellow) and our previously-demonstrated thin film device[3] (blue) as a function of target DNA concentration. (**c)** False-color SEM image of a SIP2 device with a high density of tube-in-a-tube semiconductor nanostructures which act as electrical pathways. (**d)** False-color SEM image of a representative randomly oriented, short Tube^2 thin film.

To determine the limit of detection and the dynamic range of this device configuration, we measured the signal of a SIP2 device while gradually increasing the target concentration (starting

at 10^{-17} M) until we observed the conductance spike above the background noise. The detection limit was as low as 1 fM, with an average of 6 ± 5 fM from 5 devices evaluated on this parameter. This detection limit is comparable to state-of-the-art three-terminal field-effect sensors made from MoS_2 (with a detection limit of 6 fM)[109] and clustered regularly interspaced short palindromic repeats (CRISPR) technology-integrated graphene sensors (1.7 fM)[110] in similar ionic strength conditions. However, these devices require incubation times of 15 minutes to 1 hour for the target and probe to hybridize. Additionally, unlike three-terminal FETs, our tube-in-a-tube field-effect sensors enable efficient chemical gating in a simple two-terminal design, which significantly simplifies device fabrication. Furthermore, the dynamic range of SIP2 spanned from the fM to nM range (Figure 3-2b). This large dynamic range is a significant improvement over devices fabricated from thicker thin films, which have a dynamic range of just 10 nM to 1 μM.[3]

We attribute the improvement in both sensitivity and dynamic range to the individualized and parallel tube-in-a-tube channel configuration, which confines the sensing current to parallel electrical pathways, each of which is fully gated by the target-probe interactions (Figure 3-2c). Since each electrical pathway directly bridges the electrodes, it is only necessary for target-probe interactions to occur on a single nanostructure in order for the device to be turned to a high conductance ON-state. This mechanism contrasts with conventional thin film devices where many nanostructures are not gated by the target-probe interactions due to leaky pathways, as typically with 2-dimensional materials, or embedding in bundles. Furthermore, the SIP2 configuration, with its individualized and suspended electrical pathways, also contrasts with films composed of short tube-in-a-tube semiconductor (Figure 3-2d) in which tube-tube junctions and semiconductor-substrate interactions can introduce electrical noise or crosstalk that obscure target-probe interactions at low concentrations.

3.3.3 Double mismatch selectivity for DNA biomarkers

In addition to high sensitivity and a rapid response, high selectivity that allows to distinguish between the target analyte and other similar molecules is required to prevent false positive diagnoses. Lyme disease is an excellent example of this challenge. This disease affects 300,000 Americans annually and can cause long-term nerve and tissue damage without prompt detection and treatment.[108] However, its diagnosis currently relies on a two-step process that requires both enzyme-linked immunoassay and western blotting to ensure selectivity and sensitivity.[108] The DNA from benign bacteria is also capable of binding to DNA probes for Lyme disease, which has led to false positive diagnoses in previous polymerase chain reaction-based studies. To determine the selectivity of the SIP2 sensor design, we evaluated the device response to the target sequence and then to a benign bacteria DNA sequence that contains two mismatched bases, corresponding to a 6.9% mismatch, for a direct comparison (see Table S1 for the sequences). We found the current response of the double base mismatch was only about 70% of that of the target (Figure 3-3a), demonstrating the ability to electronically distinguish between the two molecules. Additionally, we measured the device response to targets with 1 and 2 inserted bases that offset the sequence, which yielded signals of only ~60% and ~40% relative to the target analyte, respectively (Figure 3-3a).

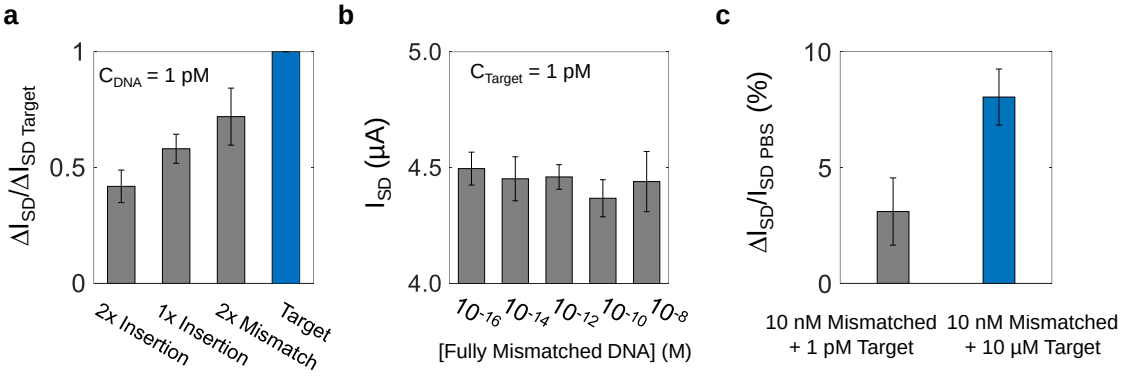

Figure 3-3. SIP2 biosensors exhibit high selectivity for the target sequence. (**a)** Comparison of the current response of a SIP2 device for the target DNA, double-mismatch DNA, and DNA analytes offset by 1 and 2 inserted bases at a constant concentration of 1 pM at the high physiological ionic strength. The signals are normalized by the current response of the target sequence. Error bars represent the standard deviation between 3 measurements. (**b)** The SIP2 device current as a function of fully mismatched DNA concentration and a constant background concentration of 1 pM target DNA. Error bars represent 1 standard deviation. The signal was averaged over 50 seconds for each condition. (**c)** Comparison of the current response of the device in 10 nM mismatched DNA and 1 pM target (gray), and after spiking the sample with 10 μM target DNA (blue). Error bars represent 1 standard deviation. The signal was averaged over 50 seconds for each condition. The voltage was 0.5 V for all the selectivity tests.

We further show SIP2 can also detect the target in the presence of other interfering molecules. We measured the response of a SIP2 device to a mixture of 1 pM target DNA and increasing concentrations of a fully mismatched 57-base DNA sequence (See Table S1 for details). Despite increasing the mismatched DNA concentration by 8 orders of magnitude, the signal did not increase (Figure 3-3b), indicating that non-specific DNA interactions with our sensor are much

smaller than those of the target DNA. To verify that the small amount of target DNA had not saturated the probes, thereby preventing non-specific binding, we further spiked the sensor with 10 µM target DNA, which induced a 159% increase in the current response (Figure 3-3c). This signal spike ruled out the possibility of saturating the probes with the 1 pM target, unambiguously confirming that the signal modulation is dominated by equilibrium between the probes and the target.

This SIP2 platform thus provides a significant advantage over the traditional diagnostic approach for Lyme disease, which requires both enzyme-linked immunosorbent assay and Western blot analysis to ensure both sensitivity and selectivity.[108] A one-step test that achieves both sensitivity and selectivity with high speed of detection, as we demonstrated here with SIP2, could enable rapid diagnosis at the point of care, thus improving the outcomes of patients suspected of having Lyme disease.

3.3.4 Tube^2 surface chemistry enables sensing in physiological conditions

The ability of the parallel pathway sensor to detect low analyte concentrations in 1X PBS, as demonstrated in the results above, is notable as this represents a physiological ionic strength condition with a short λ_D of merely 0.7 nm. Previous work has shown that sensing in such high ionic strength conditions requires passivating the sensor surface with neutral polymers[40] or using aptamer probes,[39] but it is important to note that we do not use these strategies in this work. Instead, we hypothesize that the SIP2 device's ability to sense in high ionic strength conditions results from the high density of probe molecules on the tube-in-a-tube semiconductor surface. Analytical modelling predicts that when DNA is grafted to a surface with a sufficient density, it forms a polymer brush that can exclude ions, reducing the local ionic strength compared to the bulk solution.[111] Our atomic force microscopy (AFM) studies indeed confirm that the DNA probes pack

densely on the tube-in-a-tube semiconductor surface (Figure 3-4a), which is consistent with brush formation. The average height of DNA on the tube-in-a-tube semiconductor surface was 2.3 ± 0.9 nm, with a maximum height of ~5 nm. This height is smaller than the contour length of the DNA probes (~9.9 nm)[112] probably because the AFM measurements were taken in dry conditions, however the result is comparable to previous studies of DNA brushes measured by AFM and ellipsometry.[113]

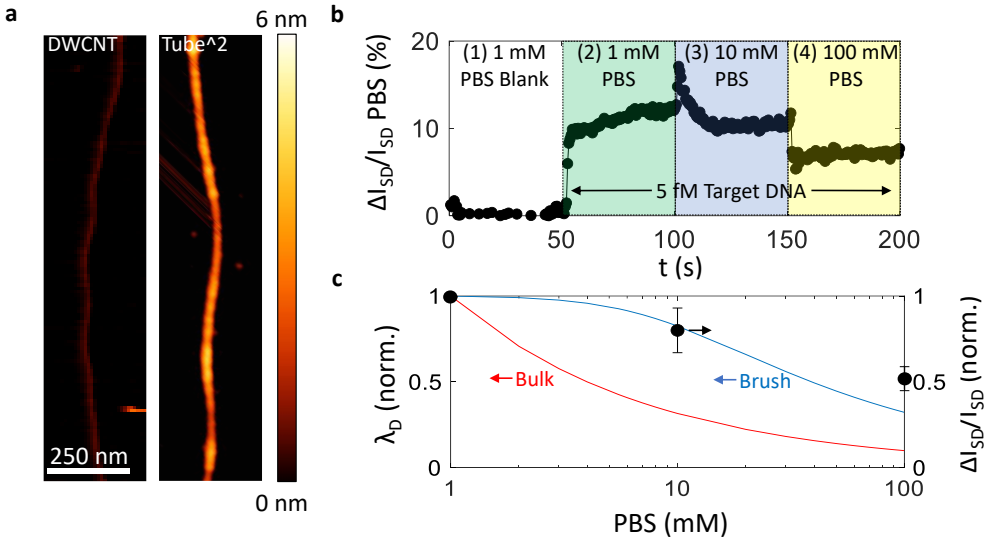

Figure 3-4. SIP2 maintains high signal transduction even at the high physiological ionic strength. (**a**) AFM micrographs of representative tube-in-a-tube nanostructures before (left) and after (right) attaching probe DNA. The probe DNA packs densely on the tube-in-a-tube semiconductor surface adding an average height of 2.3 nm (measured in dry conditions). (**b**) The current response of a SIP2 device in four ionic strength regimes: blank media composed of 0.01X PBS (1); after 5 fM of target DNA is added to the 0.01X PBS (2); and while the DNA target concentration is kept constant at 5 fM while the PBS is increased to 0.1X (3) and 1X (4). (**c**) Comparison of the SIP2 device signal at a constant target DNA concentration of 5 fM (black) and λ_D of the bulk solution (red) and the predicted λ_D in the DNA brush (blue) as a function of the ionic

strength (see the Supporting Information). The data points are normalized to the values at 0.01X PBS and averaged from 3 different devices. Error bars represent 1 standard deviation.

To determine if this brush structure contributes to the observed ability for SIP2 to sense in high ionic strength conditions, we compared the scaling of the signal in different salt concentrations. Since the ionic strength in the brush structure decays more slowly than that in the bulk solution, we expect that the signal of the SIP2 sensor will decay as a function of the calculated local ionic strength in the brush instead of in the bulk solution. We measured the current response of a SIP2 device over time at 0.5 V in 0.01X, 0.1X, and 1X PBS while the target DNA concentration was maintained at 5 fM (Figure 3-4b) and compared it with the λ_D scaling from a theoretical model proposed by Schoning and colleagues to describe field-effect and capacitive sensing with DNA brushes (see the Supporting Information).[111] From 0.01X to 1X PBS, λ_D in the bulk solution decreased by 10-fold (from 7.6 nm to 0.76 nm), but the electrical response of the SIP2 device decreased by only about 2-fold (Figure 3-4c). This decay trend of the signal closely follows that predicted by the DNA brush model,[111] further supporting that the DNA probe brush structure contributes to the remarkable sensing performance in physiological salt concentrations observed in SIP2.

We anticipate further development of SIP2 as the materials challenge is addressed. First, double-wall CNTs with semiconducting inner tubes[9] would be beneficial for optimizing the electrical transport properties of SIP2 devices. Despite the impressive performance of our SIP2 sensors, their ON/OFF ratios, between ~50 and 300, are relatively low due to the presence of some metallic double-wall CNTs in our devices that are difficult to remove completely by electrical breakdown. However, even with this low ON/OFF ratio, we have observed detection limits down to 10^{-15} M, suggesting vast room for further improvement in ON/OFF ratio and sensitivity as pure tube-in-a-

tube materials become attainable.[9,106] Secondly, large scale fabrication of SIP2 devices will require a more scalable technique for aligning the double-wall CNTs, such as the recently discovered filtration method[78] if the technique can be scaled to the monolayer thickness for effective gating, or through the use of tangential flow-induced or DNA templated CNT self-assembly.[46,114]

3.4 Conclusions

We show that parallel and suspended tube-in-a-tube field-effect sensors can effectively address the sensitivity-speed challenge in electrical detection of trace biomarkers. Compared to conventional thin films, SIP2 increases the sensitivity by approximately 6-orders of magnitude, demonstrating the significant benefits of restricting the electrical current to junction-free pathways that can be chemically gated. The collective sensing action of these parallel channels also enables fast detection (in seconds) by providing a relatively large surface area for sensing. Furthermore, the high density of probes on the tube-in-a-tube semiconductor surface contributes to sensing in high ionic strength conditions, with experimental evidence pointing to the formation of a DNA probe brush structure that locally excludes small ions. We demonstrate prototype devices targeting Lyme disease biomarkers, simultaneously achieving high sensitivity (as high as 1 fM), short detection time (< 15 seconds), as well as high chemical selectivity, all directly at high physiological salt concentrations. Our result significantly simplifies Lyme disease diagnosis, which currently requires both enzyme-linked immunoassay and western blotting to ensure selectivity and sensitivity, enabling a simple one-step diagnosis for this disease in contrast to the time-consuming and costly two-step process currently in use. Early and rapid detection of Lyme disease is just one example of the many applications that will be enabled by point-of-care electrical biosensors that can simultaneously overcome the key challenges of sensitivity, selectivity, response time, and

ionic screening. The insight we have learned here may be broadly applicable to electrical detection based on the many varieties of low dimensional materials.

Chapter 4: Direct Writing of Aligned and Suspended Carbon Nanotube Monolayers from a Gel

This chapter is adapted from a manuscript in preparation:

Benjamin Barnes, Ziyi Wang, Xiaojian Wu, Xiyuan Cheng, YuHuang Wang. "Direct writing of aligned and suspended carbon nanotube monolayers from a gel."

B.B. and Y.H.W. conceived the idea, designed experiments, and analyzed the data. Z.W. assisted in developing the CNT gel and operated the direct-write 2D plotter. B.B. performed surface functionalization, electrical characterization, and SEM and AFM imaging. X.W. assisted with PL imaging. X.C. grew DWCNTs by chemical vapor deposition. B.B. and Y.H.W. wrote the manuscript with inputs from all authors.

4.1 Introduction

Individual single-wall carbon nanotubes (SWCNTs) exhibit exceptional properties, including ultrahigh carrier mobility,[115] electrical conductance,[115] and current density,[116] as well as single-molecule chemical sensitivity.[27] Aligned[24,116] and suspended monolayers of SWCNTs can better preserve these remarkable properties in mass-produced arrays of electronic,[24] photonic, and sensing devices. Although significant advances have been made to achieve SWCNT alignment,[41] no technique has demonstrated the ability to scalably fabricate both suspended and aligned SWCNT monolayers due to several issues. Aligned growth techniques, such as directed chemical vapor deposition, provide excellent nanotube alignment over trenches[42] but the high growth temperatures required (~900 ^{o}C) are incompatible with complementary metal-oxide-semiconductor (CMOS) chip processing (~500 ^{o}C).[48] Another issue with chemical vapor deposition is the lack of control over nanotube chirality, which dictates the electronic properties

of SWCNTs. While synthesizing individual nanotube chiralities remains a grand challenge, advances in chirality sorting[22] and processing[1] of SWCNTs have opened new opportunities to address the alignment issue with solution processing. For example, using solutions of purified nanotube chiralities, dielectrophoresis can align SWCNTs between electrodes on a large scale.[117] However, this approach cannot suspend SWCNTs since removing the excess solution after dielectrophoresis would cause the SWCNTs to collapse into the trench. Alternatively, DNA templated assembly is a promising new approach that can achieve monolayer aligned SWCNTs.[45,46] Unfortunately, in addition to the expense of the high molecular-weight DNA templates (6768 bases), this approach has not been used to fabricate suspended SWCNT arrays. Finally, floating evaporative assembly can be used to fabricate substrate-wide films of aligned SWCNTs,[43,114] but the process cannot be used to directly fabricate suspended SWCNT devices because the surface tension of the solvent would cause the nanotubes to collapse.

Herein, we report a new technique that can directly print aligned fibers and thin films of SWCNTs suspended over a trench. This process is made possible using a SWCNT liquid crystalline gel stabilized by ammonium deoxycholate (ADC) surfactant, which is composed of individualized nanotubes that spontaneously align in the direction of a shear force. Even a low shear force is sufficient to align the SWCNTs, such as printing the gel through a syringe or even dipping a needle in the gel and withdrawing it by hand. Our technique preserves the electrical and photoluminescence properties of semiconducting SWCNTs since they remain individualized in the gel. Also, because of the simplicity of this technique, the gel can be used to fabricate high performance devices, potentially at large scales. We demonstrate this potential by directly printing aligned monolayers of carbon nanotubes to form disposable biosensor arrays capable of picomolar detection of RNA and DNA biomarkers. This direct-write assembly approach for achieving

aligned and suspended nanotubes may facilitate the mass production of SWCNT-based high performance thin-film electronics for advanced applications such as chemical sensing and computing.

4.2 Materials and methods

4.2.1 DWCNTS synthesis

DWCNTs were synthesized using the floating catalyst chemical vapor deposition (FCCVD) method with our home-built reactor featuring a controlled evaporation mixing system and self-designed nozzle set. We injected vaporized 2 mol% ethanol (Sigma Aldrich, anhydrous), 0.65 mol% toluene (Sigma Aldrich, ≥ 99%), 0.042 mol% ferrocene (Sigma Aldrich, ≥ 98%), and 0.021 mol% thiophene (Sigma Aldrich, ≥ 99.9%) methanol solution along with nitrogen through a hot furnace (1250 °C). High quality DWCNTs are formed and directly pulled out from the gas phase in a controlled and continuous pattern.

4.2.2 Carbon nanotube solutions

The gel printing approach appears to be applicable to most SWCNT and DWCNT species including SG65, SG65i, EC1.0, EC1.5, EC2.0, Cheap Tubes DWCNTs, and the DWCNTs synthesized in our lab by FCCVD. In all cases, the carbon nanotubes were dissolved in chlorosulfonic acid (Millipore Sigma, 99%) at a concentration of 0.1 mg/mL. We stirred the solution for 2 days to fully disperse the carbon nanotubes in the acid. After stirring, we used the superacid-surfactant exchange protocol we previously developed[85] to disperse the full-length carbon nanotubes in 2 wt% sodium deoxycholate.

4.2.3 Aqueous two-phase extraction

The (6,5)-enriched SWCNT solution was sorted using the aqueous two-phase extraction method described by Subbaiyan et al.[118] Briefly, the 2 wt% sodium deoxycholate-dispersed SG65 solution was diluted to a sodium deoxycholate concentration of 1.04 m/v%. Stock solution was prepared containing 112.8 g polyethylene glycol, 39.2 g dextran, 3.92 g sodium cholate hydrate, 8.932 g sodium dodecyl sulfate, 1.136 g NaCl, and 800 g deionized water (Nanopure™). 12.9 ml of the 1.04 m/v% sodium deoxycholate SWCNT solution was mixed with 25.5 ml of water and 244.8 ml of the stock solution and then centrifuged at 6000 g for 5 minutes. After centrifugation, the solution separated into 2 phases. The bottom phase was (6,5)-enriched. Polymers in the bottom phase were removed by ultrafiltration (Amicon® Stirred Ultrafiltration Cell, Model 8200) with a polyethersulfone membrane (Biomax® PBMK06210, 300kDA) and the final solution contained 2 wt% sodium deoxycholate.

4.2.4 Carbon nanotube/ADC gel synthesis

To synthesize the carbon nanotube/ADC gel, we added 38% HCl dropwise to 3 mL of the carbon nanotubes dispersed in 2% sodium deoxycholate to precipitate the surfactant as deoxycholic acid, and collected the precipitate by vacuum filtration. We transferred the resulting solid into a centrifuge tube and added 200 µL of water and 70 µL of 1M NH_4OH (Fisher Scientific Certified ACS Plus grade). After stirring by hand with a plastic spatula for about 5 minutes, most of the precipitate particles were dissolved to form a viscous mixture. We then centrifuged the carbon nanotube/ADC gel for 10 seconds at 1006 g (3000 rpm) to remove air bubbles and any undissolved solids. The carbon nanotube/ADC gel was then ready to be used as an ink for direct writing onto substrates.

4.2.5 Removing excess ADC

For fibers contacting the substrate, the excess surfactant was removed by rinsing with ethanol along the axis of the fiber to avoid introducing disorder into the resulting carbon nanotube film. For suspended fibers, rinsing was not possible since the surface tension of the solvent would cause the carbon nanotubes to collapse. Therefore, we removed the excess surfactant by annealing at 400 ^{o}C, which can cleanly burn away the ammonium ADC surfactant from the carbon nanotube sidewalls.[119]

4.2.6 Contact resistance measurement by the transmission line method

We prepared gold electrodes on a silicon wafer with 10, 20, 25, and 60 μm gaps. We deposited DWCNT/ADC gel fibers on the electrodes from a syringe and removed the ADC with ethanol rinsing. As a control, we prepared a thin film of the same DWCNT species (grown by chemical vapor deposition in our lab as described above) by vacuum filtering the nanotube solution through a polycarbonate filtration membrane. We cut and transferred a strip of the membrane to the electrodes on the wafer (with DWCNTs facing the substrate) and removed the excess polycarbonate by soaking in chloroform (20 minutes) and rinsing with ~10 mL of fresh chloroform. Both the printed sample and control were annealed at 300 ^{o}C for 45 minutes in air to improve the contact between the DWCNTs and electrodes. We measured the resistance of 3 sets of the 4 electrode gaps and extracted the width-normalized contact resistance.

4.2.7 Test-strip biosensor fabrication

We purchased commercial blood glucose test strips (GE100 Blood Glucose Test Strips Gold Electrode) as substrates for our biosensors. To expose the electrodes, we peeled away the plastic cover from the test strip, and then dissolved the adhesive residue with isopropyl alcohol (Sigma Aldrich 99.5%). Next, we removed the enzyme-containing gel from between the electrodes by

rinsing it with water and isopropanol, and then blow-dried the test strip with compressed air, leaving the gold electrodes exposed.

A batch of test strips were taped to a glass slide in parallel. We loaded a syringe (34-gauge needle) with gel made from DWCNTs grown by chemical vapor deposition (as described above) and printed it onto the parallel test strips at a speed of 0.13 m/s using an inexpensive 2D plotter (Bachin T-A4). The excess ADC was removed from the gel by gently rinsing the channel with ethanol and then blowing it dry with compressed air. The bare electrodes exhibit strong electrochemical activity in solution, so to passivate them we printed a dot of polydimethylsiloxane (Sylgard® 184) on each gold electrode and cured it at 70 ^{o}C. The polydimethylsiloxane did not cover the DWCNT channel.

To convert the DWCNTs into Tube^2 nanostructures, we functionalized them by soaking the prepared test strips in 100 mM 2-fluorobenzoic acid diazonium salt for 12 hours in the dark.[31] Next, we attached DNA probes to the Tube^2 nanostructures (with 5' amine linkers) by carbodiimide activation with 1-ethyl-3-(3-dimethylaminopropyl)-carbodiimide hydrochloride and sulfo-N-hydroxysulfosuccinimide (Fisher Scientific), as previously described.[3] See Table 4-1 for the DNA and RNA sequences used in this chapter. Electrical characterization and sensing experiments were conducted with a Keithley 4200 semiconductor parameter analyzer.

Table 4-1. DNA and RNA sequences used in test-strip sensing experiments

Name	Sequence	Charges per molecule
Probe	5' TAGTCTGAACAACTGGTGTAAGTTCCATCTCTAATTGAG GTTGAACCTCAATTG	54
DNA Target	5' CAATTGTTGAGGTTCAACCTCAATTAGAGATGGAACTTA CACCAGTTGTTCAGACTA	57
RNA Target	5' CAAUUGUUGAGGUUCAACCUCAAUUAGAGAUGGAACU ACACCAGUUGUUCAGACUA	57

A simple polydimethylsiloxane test cell was used in the sensing experiment to hold the test strip steady for electrical characterization and maintain a constant volume of analyte solution. We measured the current as a function of time (at 0.5 V_{SD}) while injecting buffer (0.1X PBS) as a control, or target DNA. The sensing experiment was also repeated for one device featuring an alternative RNA target, which elicited a similar response as the DNA tests.

4.3 Results and discussion

4.3.1 pH tuned SWCNT dispersions form a self-assembling ink

Our direct-write assembly technique was enabled by an accidental discovery that ADC (Figure 4-1a), a highly effective surfactant widely used for dispersing SWCNTs in water (Figure 4-1b, left), transitions through several distinct phases (liquid, gel, and solid) depending on the degree of protonation. If the pH of a SWCNT solution in ADC is reduced to below the pKa of deoxycholic acid (~6.6), the surfactant becomes protonated, forming an insoluble composite packed with SWCNTs (Figure 4-1b, right). However, when we deprotonate approximately 50% of the deoxycholic acid molecules in the composite by adding ammonium hydroxide, we find that the material turns into a gel (Figure 4-1b, middle). We applied this technique to make carbon nanotube gels with a wide variety of carbon nanotube species, including purified SWCNT semiconductors, unsorted commercial SWCNTs, and double-wall carbon nanotubes (DWCNTs; see Methods for more details).

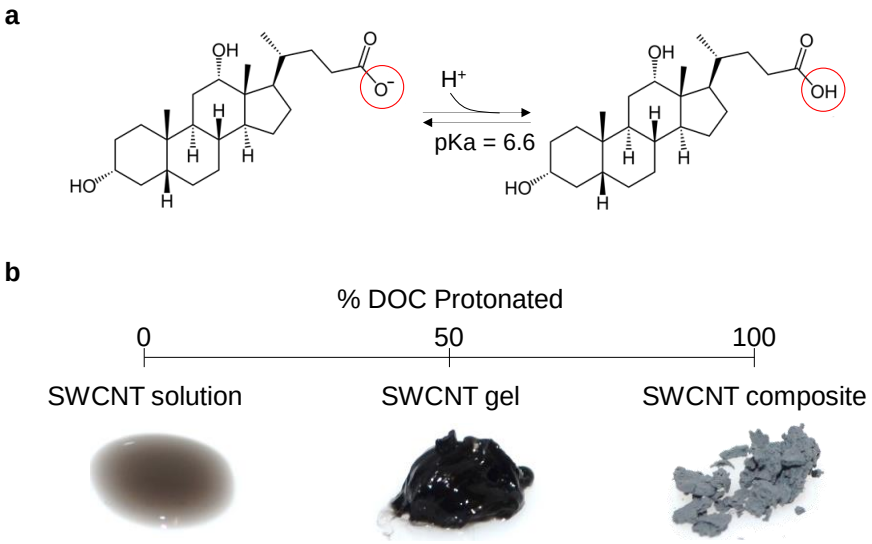

Figure 4-1. The phase behavior of a deoxycholate surfactant-stabilized suspension of SWCNTs can be tuned with pH. a) At pH above 6.6, unprotonated deoxycholate anions are water soluble. Below pH 6.6, the deoxycholate is protonated, forming insoluble deoxycholic acid. **b)** The ADC-SWCNT mixture can reversibly transform between solution, gel, and solid composite, depending on the degree of protonation. At ~50% protonation, a SWCNT gel forms spontaneously.

This SWCNT/ADC gel exhibits liquid crystalline properties, with self-assembled millimeter sized rod-like domains visible by optical microscopy (Figure 4-2a). Rod-like liquid crystal have been observed in highly concentrated sodium deoxycholate solutions[120] and attributed to a combination of hydrophobic interactions, and hydrogen bonding.[121] Notably, the self-assembled domains can be aligned with an applied shear force. For example, we sandwiched the gel between two sapphire slides and sheared the slides in opposite directions to align the self-assembled domains. Photoluminescence imaging of the sheared gel film indicates that the SWCNT align with a high degree of long-range order (Figure 4-2b).

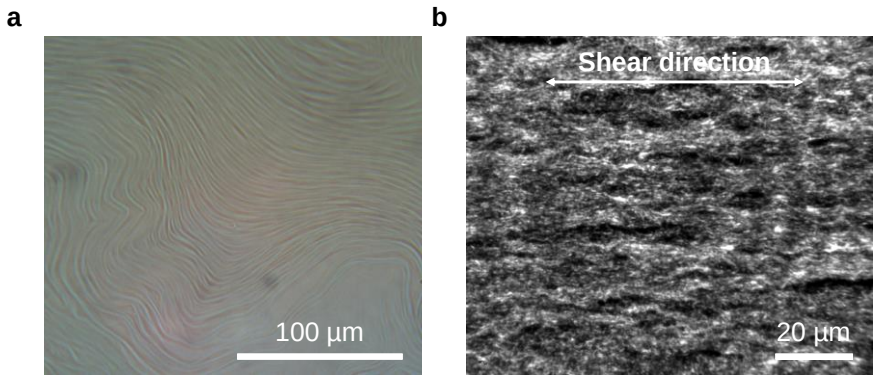

Figure 4-2. SWCNT/ADC gel self-assembles into liquid crystalline domains that can be oriented with a shear force. a) Optical micrograph of the SWCNT/ADC gel sandwiched between two glass slides, which demonstrates liquid crystalline behavior as indicated by the striations. **b)** Photoluminescence image showing alignment of SWCNTs after shearing the SWCNT/ADC gel between two sapphire slides.

4.3.2 The ink contains individualized and aligned SWCNTs

The SWCNT/ADC gel also spontaneously forms fibers when certain shear forces are applied. For example, by simply dipping a needle into the SWCNT/ADC gel, we can pull out a continuous fiber, as long as 30 cm in length at merely 1 µm in diameter (Figure 4-3a), reminiscent of the behavior of molten polymers or small molecule amphiphile gels.[122] The SWCNTs are aligned along the axis of the fiber, as evidenced by SEM imaging (Figure 4-3b). Furthermore, under high vacuum conditions, some cracks ~200 nm wide are formed in the solidified gel, exposing the SWCNTs uniformly dispersed throughout the fiber cross-section. SWCNT/ADC gel fibers made using (6,5)-enriched semiconducting SWCNTs (obtained by aqueous two-phase extraction[118]) fluoresce at 990 nm, which is the E_{11} photoluminescence characteristic of (6,5)-SWCNTs (Figure 4-3c, d). Remarkably, this photoluminescence is brightly visible for both the (6,5)-enriched

sample, as well as unsorted SG65 SWCNT material, which contains metallic nanotubes (Figure 4-3d). Normally the small population of metallic SWCNTs in the unsorted SG65 material leads to photoluminescence quenching as the metallic and semiconducting SWCNTs form junctions and bundles. The bright emission of the unsorted SG65 gel fiber indicates that the SWCNTs are not bundled but are instead spaced apart from each other by the surrounding gelled ADC molecules. The lower PL intensity in the SG65 fiber compared to the (6,5) fiber is possibly due to differences in the fiber diameter. Additionally, the presence of other SWCNT chiralities, such as (6,4) and (8,3), cause a slight shift in the E_{11} emission wavelength (980 nm) of the SG65 fiber compared to the (6,5) fiber (990 nm).

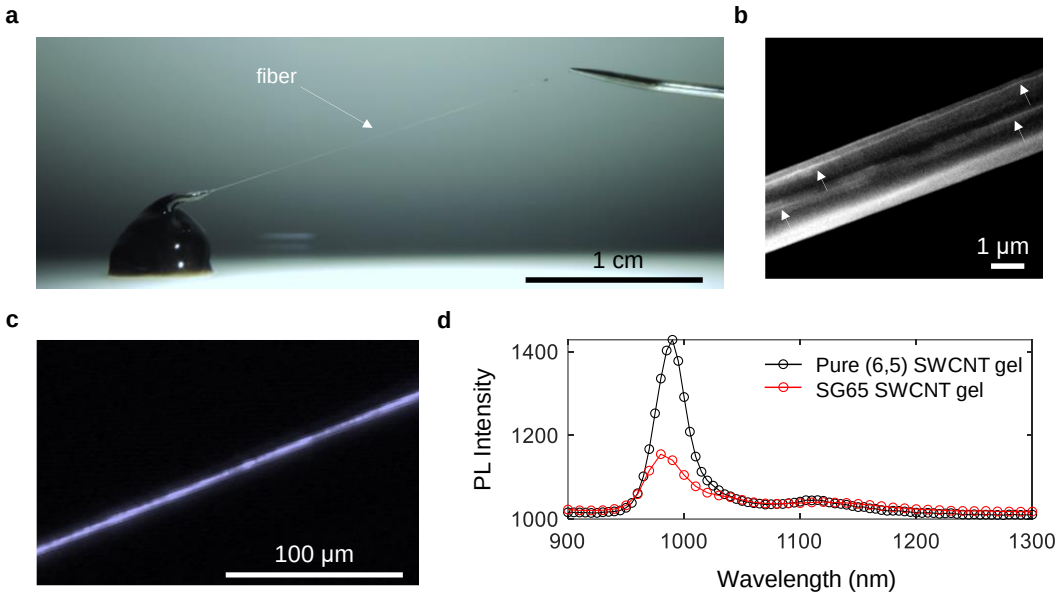

Figure 4-3. SWCNT/ADC gels can be pulled into microfibers containing aligned, individualized SWCNTs. a) Photograph of a thin SWCNT/ADC fiber being pulled from a droplet of a SWCNT/ADC gel using a needle. **b)** SEM image showing SWCNTs (indicated with arrows) near the surface of the fiber and oriented along the fiber axis. **c)** False-color photoluminescence image showing the bright E_{11} emission (990 nm) from (6,5)-SWCNTs within the fiber under excitation by a 561 nm laser. **d)** Photoluminescence spectra showing the strong E_{11} emission from the (6,5)-SWCNT chirality for fibers made from both raw SG65 and purified (6,5)-SWCNT solutions.

4.3.3 Printing microfibers and aligned thin films of SWCNTs

The fibers can be deposited as monolayers onto a variety of substrate morphologies. For example, by withdrawing a fiber using a needle, we can place it between two gold pillars (Figure 4-4a). Alternatively, we can deposit aligned SWCNTs on an electrode array (Figure 4-4b) or silicon wafer (Figure 4-4c) by gently contacting a gel-loaded syringe to the substrate and moving it in the writing

direction. A micropositioner was used in this study for consistency, but the technique is sufficiently robust to deposit fibers with an inexpensive 2D plotter or even by hand.

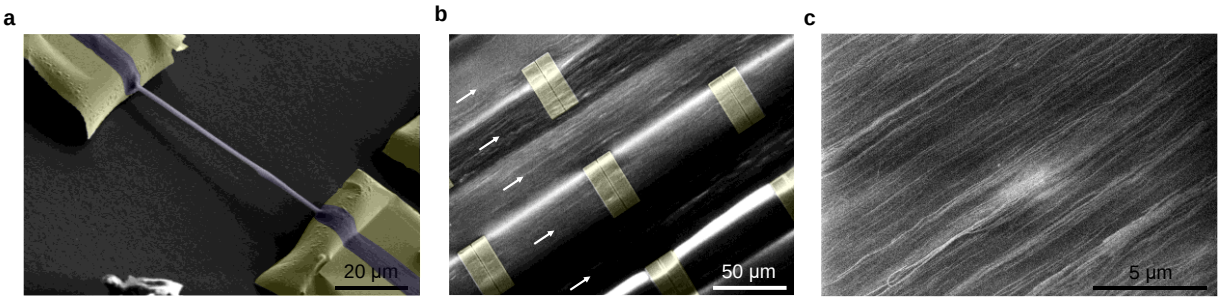

Figure 4-4. The SWCNT/ADC gel can be directly written as suspended fibers or aligned monolayer films. a) SEM image of a SWCNT/ADC gel fiber suspended between two gold pillars. The image is false-colored to show the different components (the SWCNT/ADC gel is purple, and the electrodes are yellow). **b)** SEM image of the SWCNT/ADC gel written onto an array of gold electrodes on a silicon substrate. The white arrows indicate the individual fibers. The electrodes are false-colored yellow for clarity. **c)** High magnification SEM image showing the aligned SWCNT monolayer written on the silicon substrate.

4.3.4 Fabricating suspended monolayers of SWCNTs

Fabricating suspended monolayers of carbon nanotubes has historically been a challenge as the solvents used in solution processing would cause the SWCNTs to collapse into the trench. We have recently found that the ADC surfactant used to make the gel can be removed by gentle thermal annealing.[119] This advance enables us to print the SWCNT/ADC gel across a trench and remove the ADC molecules without the SWCNTs collapsing. To demonstrate, we produced an array of gold electrodes separated by trenches 1 µm wide and 120 nm deep. We then printed the EC2.0 SWCNT/ADC gel in stripes across the electrode array using a syringe. SEM shows the SWCNTs

embedded in the gel and draped across the trench (Figure 4-5a). After thermal annealing at 400 °C the SWCNTs remained suspended across the gap while the excess ADC molecules were removed (Figure 4-5b; see Methods for details). Figure 4-5c shows that the SWCNTs form clean parallel electrical pathways between the electrodes. To our knowledge, this is the only technique that can directly print aligned nanotube monolayers over a trench.

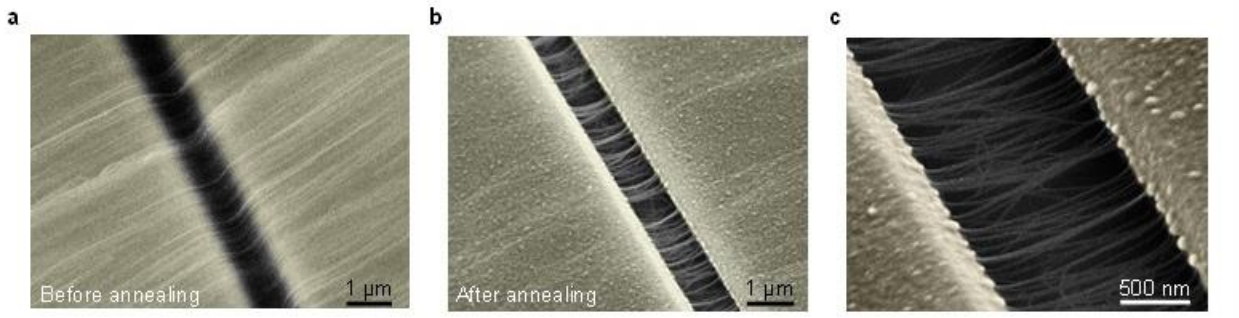

Figure 4-5. The SWCNT/ADC gel can be used to directly print aligned SWCNT monolayers over trenches. a) High magnification SEM showing aligned SWCNTs within the gel suspended across a trench between two gold electrodes. **b)** After thermal annealing, the excess ADC is removed and the SWCNTs remain suspended over the trench. **c)** High magnification SEM image of clean, individualized SWCNTs suspended across the trench after annealing.

This unique monolayer printing capability seems to arise from the wetting behavior of the gel on substrates. It is notable that when contacting metal, silicon, or glass substrates, the SWCNT/ADC gel evenly spreads out, wetting the surface such as in Figure 4-4a. In addition to enabling the printing of monolayer films, this behavior should translate into excellent electrical contact. To test this, we deposited DWCNT gel fibers on gold electrodes with different channel lengths and then removed the excess ADC by rinsing the fiber with ethanol. DWCNTs were used as they have exhibited high electrical conductance in previous studies.[8] As a control, we deposited DWCNTs

on a polycarbonate membrane by vacuum membrane solution transfer, a common approach for fabricating nanotube thin films,[54,123] and transferred the DWCNT film to the gold electrodes and used chloroform to remove the polycarbonate (see Methods for details). We then measured the contact resistance of the fiber and film morphologies using the transmission line method, finding that the gel-printed DWCNT fiber featured a ~3x reduction in contact resistance (width-normalized) than that of the film fabricated by vacuum membrane solution transfer.

4.3.5 Disposable biosensors for SARS-CoV2 RNA printed from self-assembled ink

To demonstrate the scalability of this printing technique for electrical devices, we used a batch process to fabricate electrical biosensors in parallel using blood glucose test strips as the substrate (Figure 4-6a). The glucose test strip is an ideal example of successful point-of-care testing, in that it can be mass produced and has a reproducible sensing response.[99] As a proof-of-concept, we used tube-in-a-tube (Tube^2) nanostructures as the device channel. Tube^2 nanostructures are heavily functionalized semiconducting DWCNTs that enable sensitive chemical detection in a simple two-electrode device configuration, as we described previously.[3] To form the device, we printed DWCNTs directly across the electrodes on the test strip using a 2D plotter (Figure 4-6b) and then converted them into Tube^2 nanostructures by functionalizing the DWCNT surfaces with 2-flurobenzoic acid diazonium salt.[31] The aligned Tube^2 nanostructures can be seen in the device channel by AFM (Figure 4-6c).

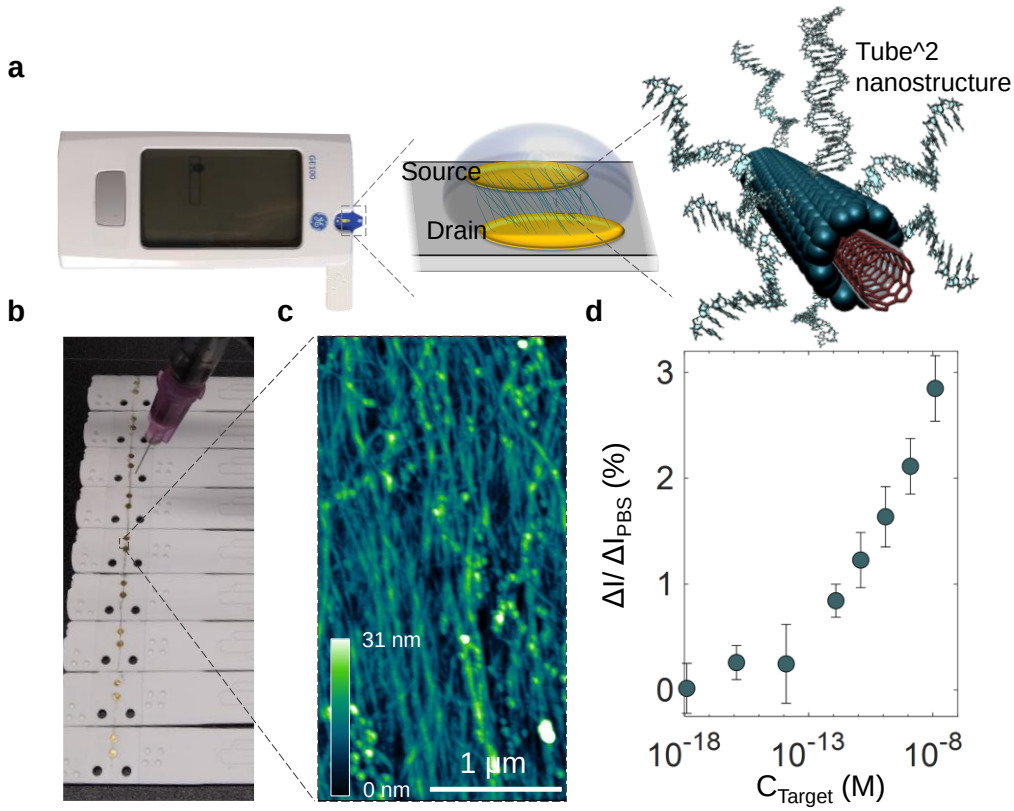

Figure 4-6. Highly sensitive diagnostic devices printed from the DWCNT/ADC gel. a) A DWCNT gel can be printed onto disposable test strips, much like the fabrication of blood glucose sensors. **b)** The process can be automated with a simple 2D plotter to make large batches of test strip sensors. **c)** AFM confirms that the DWCNTs remain aligned in the device channel. **d)** The printed sensors exhibit picomolar level detection of SARS-CoV-2 biomarkers. Error bars represent the coefficient of variance of the current at each concentration.

As a model sensing system, we chose a 57-base SARS-CoV-2 RNA sequence as the target given the importance of inexpensive and rapid tests in stemming viral transmission. The approach we used here can also apply to other RNA or DNA biomarkers simply by changing the identity of the probe molecule attached to the Tube^2 nanostructures to meet rapidly evolving public health needs. Initially, we used a DNA mimic of this target RNA sequence for device characterization

since RNA is degraded more rapidly than DNA. We attached DNA probes for the SARS-CoV-2 biomarkers to the carboxyl groups on the Tube^2 surface using carbodiimide linking (see Methods for details and the DNA sequence) and determined their sensing response to increasing target DNA concentrations (Figure 4-6d). We compared five devices to find a limit of detection for both DNA and RNA model biomarkers in the range of 10^{-15} to 10^{-11} M in 0.1X PBS. We note that this device is a simple proof-of-concept, and the sensitivity could be further optimized in terms of the nanotube number density and by using a chirality sorting technique to enrich the Tube^2 structures with semiconducting inner walls increase their ON/OFF current ratio[9] and therefore the magnitude of their response to target molecules.

These test strip devices exhibited notably low heterogeneity in their conductance, addressing a major roadblock in the scaling of carbon nanotube electronics. Device heterogeneity arises from the variability in the number of nanotubes crossing the channel, and from the chirality of the nanotubes. To circumvent this roadblock, thin films of randomly oriented carbon nanotubes are often used, but this approach also leads to reduced sensitivity due to the presence of junctions and bundles, which may provide non-gated electrical pathways or introduce electrical noise. In our case, since the DWCNTs are evenly distributed within the gel, and since a continuous gel stripe can be printed across a large batch of devices (Figure 4-6b), we can achieve more uniform properties compared to other fabrication techniques. For example, the electrical resistance of dielectrophoresis-deposited DWCNTs exhibits high variability between devices, with a coefficient of variance of 216.9% (N = 14). In contrast, our gel-printed films made with the same DWCNT source had a coefficient of variance of 149.7% (N = 10), a 31% improvement. We anticipate that this homogeneity can be further enhanced by using chirality sorting to achieve uniform inner and outer wall electrical properties.

4.4 Conclusions

This work addresses the challenge of forming aligned and suspended SWCNT monolayers for thin film electronics. We find that at about 50% protonation, ADC surfactant-stabilized SWCNT solutions form composite gels that exhibit self-assembly behavior, allowing us to directly print aligned SWCNTs in various forms, including fibers and thin films. Remarkably, the printed carbon nanotubes can align in monolayers suspended over trenches and exhibit low contact resistance, reduced electrical heterogeneity, and bright photoluminescence. We directly printed sensitive SARS-CoV2 biosensors to demonstrate the potential application of this direct-write assembly approach in scaled device fabrication for public health and point-of-care diagnosis. We expect that this technique will help finally open the way for the scalable production of high-performance SWCNT electronics.

Chapter 5: Scalable Production of Fiber Field-effect Transistors for Neurotransmitter Detection

This chapter is adapted from a manuscript in preparation:

Benjamin Barnes, Fathima-Zhulfaa Zhulficar, Ziyi Wang, Jeffrey Fagan, YuHuang Wang.

B.B. and Y.H.W. conceived the idea, designed experiments, and analyzed the data. F-Z.Z. and Z.W. assisted with preparing the CNT gel and coating fibers. J.F. purified (6,4) SWCNTs. B.B. performed device fabrication, surface functionalization, electrical characterization as well as all the other experiments. B.B. and Y.H.W. wrote the manuscript with inputs from all authors.

5.1 Introduction

Communication in the human brain involves a combination of electrical signals along the neuron, and chemical signals at the synapses between neurons.[124] The electrical signals are now well understood and can be both recorded and induced with implantable electrophysiological probes,[125] leading to breakthroughs in our understanding of brain function as well as neurological disorders and their treatment. However, the flow of chemical information is not equally understood, leading to a vast gap in our picture of brain function.[126]

Implantable field-effect transistor (FET) chemical sensors have recently been investigated for neurotransmitter detection.[49,51] One example made from a plastic shank patterned with indium oxide semiconductor and metal contacts was used to detect serotonin successfully.[49] The materials constraints of such devices limit their performance, however. For example, the plastic shank is on the order of 50 µm wide reducing its flexibility which can lead to scarring of the brain tissue over time.[127] Fiber-like devices are attractive for overcoming this problem, as they can be made from more flexible and biocompatible materials such as carbon nanotubes.[127,128] For example, a

dopamine sensor was recently demonstrated consisting of two metal fibers bridged by a semiconducting polymer, and one dry-spun single-wall carbon nanotube (SWCNT) fiber acting as the gate.[51] While such an approach offers advantages in flexibility, the device platform is still large at a total of ~150 µm in diameter, raising biocompatibility concerns. Furthermore, the semiconducting polymer has low electrical mobility and low On-state conductance, limiting the sensitivity of the device. Aligned SWCNTs have been used in ultrahigh performance chemical sensing,[27,28] and would be the ideal material for the fabrication of fiber-like sensors, but there is currently no way to fabricate such devices scalably and with a form factor conducive to neural implantation.

In this work, we approach this difficult problem with a new fabrication technique that enables the production of FET chemical sensors on the surface of 10 µm diameter para-aramid fibers. By pulling the para-aramid fibers through a semiconducting single wall carbon nanotube (SWCNT) gel at high speed (>0.6 km min^{-1}), we can form aligned monolayers of chirality pure semiconductors on the para-aramid surface. The aligned SWCNT monolayer enables a high On-state conductance (~24 µS) in a solution-gated configuration. Additionally, the fibers can be imparted with chemical functionality by attaching aptamers for selectively binding neurotransmitters, which electrostatically gate the fiber FETs in response to target molecules.

5.2 Materials and methods

5.2.1 Gel synthesis

SWCNT solutions were prepared using the superacid surfactant exchange method previously described in our lab.[85] Briefly, SWCNTs were dissolved in chlorosulfonic acid at a concentration of 0.5 mg/mL. After stirring for at least 24 hours, we added the dissolved SWCNTs dropwise to a solution containing 0.08 wt% sodium deoxycholate and 0.75 M NaOH. The volume ratio of

SWCNT solution to sodium deoxycholate solution was 4:250. We then added HCl to the solution to precipitate the SWCNTs and sodium deoxycholate. The precipitate was collected, washed with deionized water, and then redissolved in water and NaOH to a DOC concentration of 2 wt%. We then centrifuged the solution to remove bundles. Gel was prepared by precipitating 3 mL of the above solution by adding HCl, and redissolving the precipitate with 70 µL of 1 M NaOH and 200 µL of deionized water.

5.2.2 Gel coating

One end of the para-aramid fiber was tied to the rotor of a benchtop centrifuge and a droplet of gel was placed on the fiber. We then turned on the centrifuge at a designated velocity and allowed it to pull the fiber through the gel. To remove excess DOC, we flowed ethanol along the axis of the coated fiber.

5.2.3 SWCNT functionalization

SG65 SWCNTs were functionalized with a one-pot method previously developed in our lab.[30] Briefly, SWCNTs were dissolved in chlorosulfonic acid at a concentration of 0.1 mg/mL with stirring for 24 hours. Next, sodium nitrite and 4-amino 2-fluorobenzoic acid were added to the chlorosulfonic acid solution at a 1:1:1 mole ratio with the carbon. The solution was then added dropwise to water, collected on a filter, dried, and redispersed by superacid surfactant exchange as described above.

5.2.4 Fiber FET patterning

We found that water sprayed from a micro-syringe with a 57 µm diameter can fully remove the gel from the fiber surface to create 50-100 µm gaps. To pattern FETs, we first coated the whole fiber with (6,4) SWCNTs, and then removed the DOC by rinsing with ethanol. Next, we coated

metallic SWCNTs on the fiber, patterned 50 µm gaps using water, and then removed the DOC with ethanol rinsing. The underlying semiconducting SWCNT coating was not removed by water since it was already stabilized by ethanol rinsing.

5.3 Results and discussion

5.3.1 Forming aligned thin films of SWCNTs on the surface of strong synthetic microfibers

Previously we reported a SWCNT liquid crystal gel made from ammonium deoxycholate that can be printed into aligned SWCNT arrays on silicon substrates (Chapter 4). We have observed that aligned monolayers of SWCNTs form on the surface of synthetic 10 µm diameter para-aramid fibers when pulled through this gel at high velocity (Figure 5-1a). Para-aramid single fibers are highly flexible yet have an exceptionally high longitudinal Young's modulus of ~85 GPa (for 12 µm diameter).[129] This means that the fiber can withstand high-speed reel-to-reel style processing while remaining mechanically compatible with neural tissue.[127] The SWCNT gel easily wets the para-aramid surface, enabling the fabrication of conformal SWCNT coatings on the surface (Figure 5-1b-c).

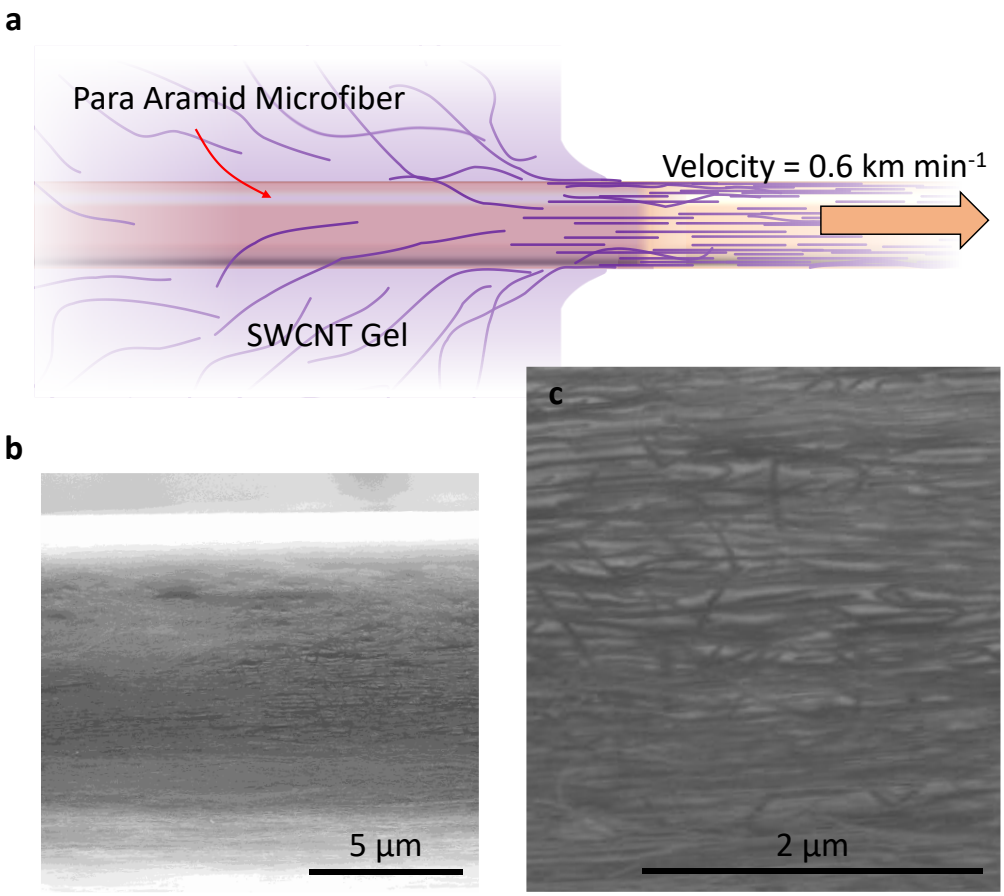

Figure 5-1. Aligned monolayers form on para-aramid fibers when they are pulled through a SWCNT gel at high velocity. a) schematic of the SWCNT gel coating a para-aramid fiber. **b)** low-magnification SEM image of an EC1.0 SWCNT coating on the surface of the para-aramid fiber. **c)** High resolution SEM image showing the aligned SWCNT monolayer on the para-aramid surface.

The pulling speed is a critical parameter for achieving quality aligned thin films of SWCNTs on the para-aramid surface. It is notable that at arbitrarily low speeds, the coatings of SWCNTs are aligned due to the liquid crystalline nature of the SWCNT gel, but are very thick, up to ~2 µm (Figure 5-2), which corresponds to a dense multilayer of SWCNTs. At higher speeds, the coatings

form sub-monolayers of SWCNTs, but it is notable that above 1 km min^{-1} some disorder is introduced into the resulting film due to turbulence. A coating velocity of about 0.6 km min^{-1} is the optimal for creating SWCNT monolayers while retaining excellent alignment (Figure 5-2, center).

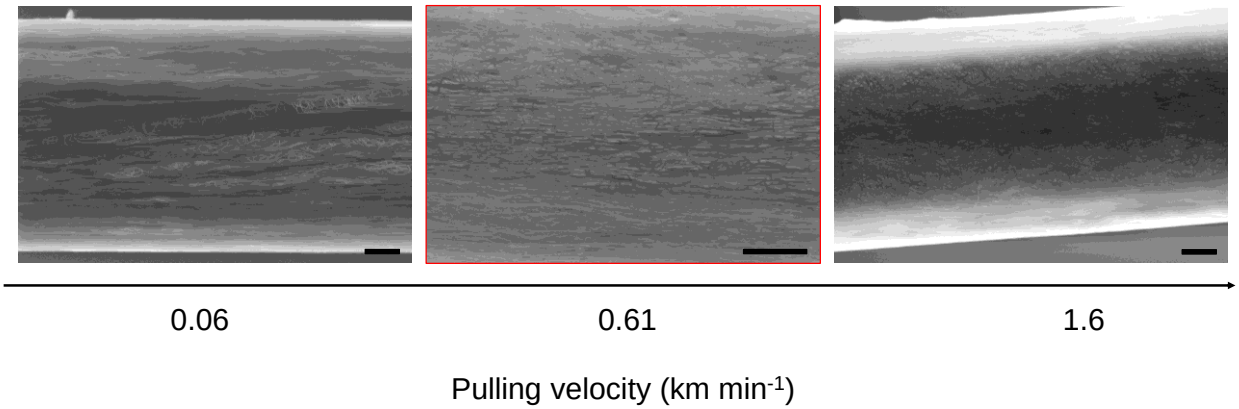

Figure 5-2. Alignment and monolayer coating is optimized by pulling speed. Representative SEM images of para-aramid fibers pulled through a SWCNT gel at increasing velocities. At low velocity (left), the aligned SWCNT layer is on the order of 2 µm thick. At higher velocity (center) the SWCNTs remain aligned, but the thickness is reduced to approximately a monolayer. At a higher velocity (right) the coating remains thin, but the SWCNTs become disorganized, possibly due to turbulence. All scale bars are 2 µm.

5.3.2 Controlling electrical functionality of the fibers with solution processed SWCNTs

One advantage of this coating approach over using dry-spun carbon nanotube fibers is that we can control the SWCNT chirality through solution processing to achieve electrically functional fibers.[22] In contrast, dry-spun carbon nanotube fibers are typically made from a raw carbon nanotube material directly from the growth furnace which contains a wide variety of semiconducting and metallic nanotubes,[55] therefore limiting the electronic functionality of the

fiber. The coating method developed in this work however, enables the use of SWCNTs purified by electronic type with aqueous two-phase extraction.[22] As a demonstration, we coated a fiber with pure (6,4) SWCNTs purified by aqueous two-phase extraction. UV-visible absorption of the (6,4) gel (Figure 5-3a) shows the characteristic E_{11} absorption peak at 880 nm. We note that the sharpness of the peaks and the low background indicate that the SWCNTs in the gel are not significantly bundled. After coating fibers with the SWCNT gel, we can remove the DOC molecules by rinsing the fiber with ethanol along the fiber axis. This removes the DOC without disturbing the SWCNT alignment. Raman analysis shows that the (6,4) radial breathing mode peak on the coated para-aramid fiber at 337 cm^{-1} indicating that the fiber now has the semiconducting functionality of the (6,4) SWCNTs (Figure 5-3b). Furthermore, mapping the intensity of the 337 cm^{-1} peak on the para-aramid fiber confirms the uniformity of the SWCNT coating on the fiber surface (Figure 5-3c).

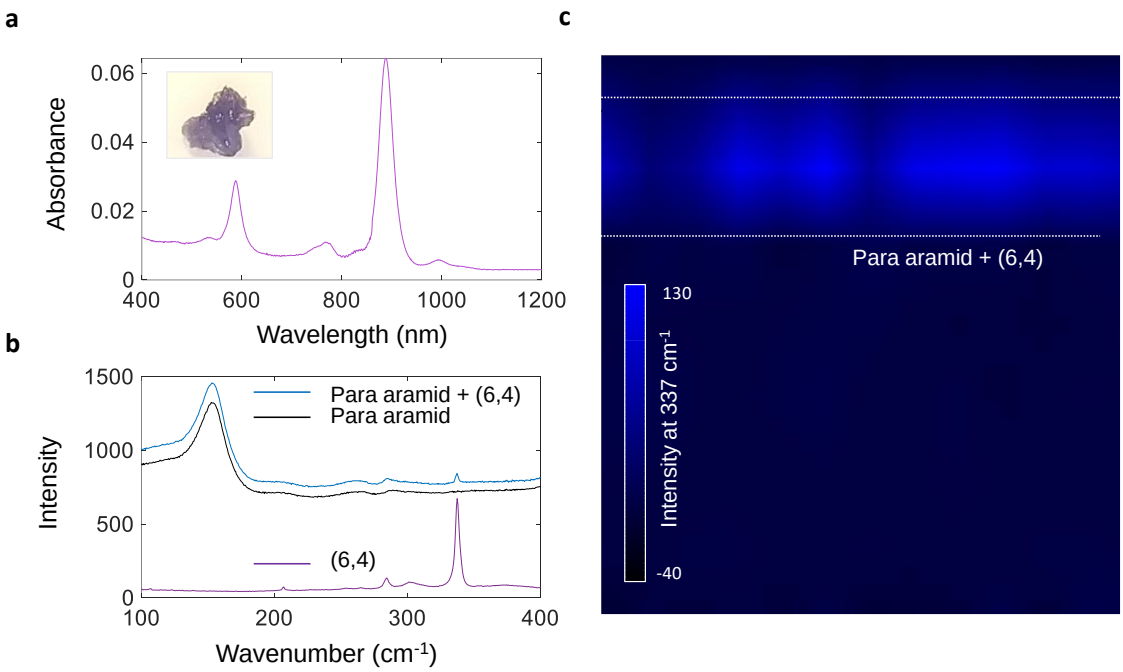

Figure 5-3. Chirality-pure SWCNTs can be coated on the para-aramid fibers to impart semiconducting functionality. a) UV-visible absorption spectrum of the (6,4) SWCNT gel sandwiched between two glass coverslips shows the sharp E_{11} absorption peak at 880 nm and low background levels, characteristic of individualized (6,4) SWCNTs. The inset is a photograph of the (6,4) SWCNT gel. The purple color is due to the bandgap of the (6,4) SWCNTs and is indicative of high purity. **b)** Raman analysis of the pure (6,4) SWCNTs, and para-aramid fiber, as well as (6,4) SWCNT-coated para-aramid fiber unambiguously confirming the SWCNT coating on the fiber surface. Excitation was with a 633 nm HeNe laser, and spectra are averages of 3-4 different points. **c)** Raman map of intensity of the peak at 337 cm^{-1} for a (6,4) SWCNT-coated fiber showing the attachment of semiconducting SWCNTs on the surface.

Additionally, we can create highly electrically conductive coatings by using metallic carbon nanotubes. For example, we used this method to coat EC1.5 SWCNTs on the fibers and achieved

an electrical conductance as high as ~83 S/m. EC1.5 was chosen as it contains a large proportion of metallic SWCNTs. Metallic SWCNT fibers can be used as electrical traces for fiber-like FET sensors, as the aligned carbon nanotube surfaces increase biocompatible,[130] have a low contact resistance with the semiconducting SWCNT channel, and are highly electrically conductive.

5.3.3 Patterning FETs on the fiber surface

By patterning alternating sections of semiconducting and metallic SWCNT coatings, we can easily create fiber FETs. First, we coat a semiconducting layer and remove the surfactant with ethanol, and then coat a metallic layer on top. Spraying the fiber with a thin stream of water from a micro syringe creates 50 μm gaps in the metallic SWCNT coating without disturbing the underlying semiconductors. These gaps form the semiconducting channels of the fiber FETs (Figure 5-4a). We evaluated the electrical properties of these fiber FETs with a solution gated configuration. Multiple FETs patterned on the same fiber show uniform electrical conductance, within an order of magnitude, and similar ON/OFF switching (Figure 5-4b), comparable with high performance solution gated graphene FETs[131] but lower than that typically seen in SWCNT FETs. This discrepancy may be attributed to incomplete removal of metallic SWCNTs from the channel during the patterning process.

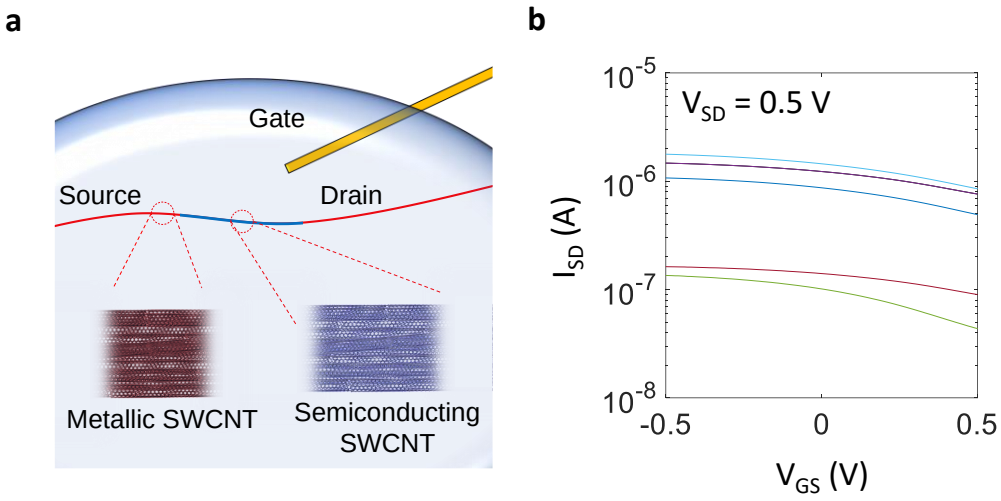

Figure 5-4. Fiber FETs can be electrically gated. a) Schematic of the fiber FET characterization. **b)** Gated IV curves of 5 devices patterned on the same fiber show high ON conductance and ON/OFF current ratios up to 5.

5.3.4 Adding chemical functionality with covalently-modified SWCNTs

To add chemical functionality to these fiber FETs, we coated them with a functionalized SWCNT layer. Functionalization of SWCNTs with diazonium salts is a versatile approach for tuning the optical and chemical properties of the material.[29] In this case, we functionalized SWCNTs with a high degree of carboxyl functional groups by reacting them in chlorosulfonic acid with 2-fluorobenzoic acid diazonium (Figure 5-5a). This is a highly scalable approach to chemical modification.[30] The degree of functionalization can be inferred from the growth of the Raman D/G ratio and loss of the radial breathing mode peak of the SWCNTs (Figure 5-5b). The carboxyl groups serve as attachment points for amine-terminated DNA aptamer probes (Figure 5-5a). In this case, we attached aptamers used in previous literature for binding dopamine.[39] The attachment of the aptamers can be seen at the single-SWCNT level with atomic force microscopy (AFM)

(Figure 5-5c). Analysis of the feature height before and after the reaction confirm that that the aptamers are attached to the SWCNTs (Figure 5-5d).

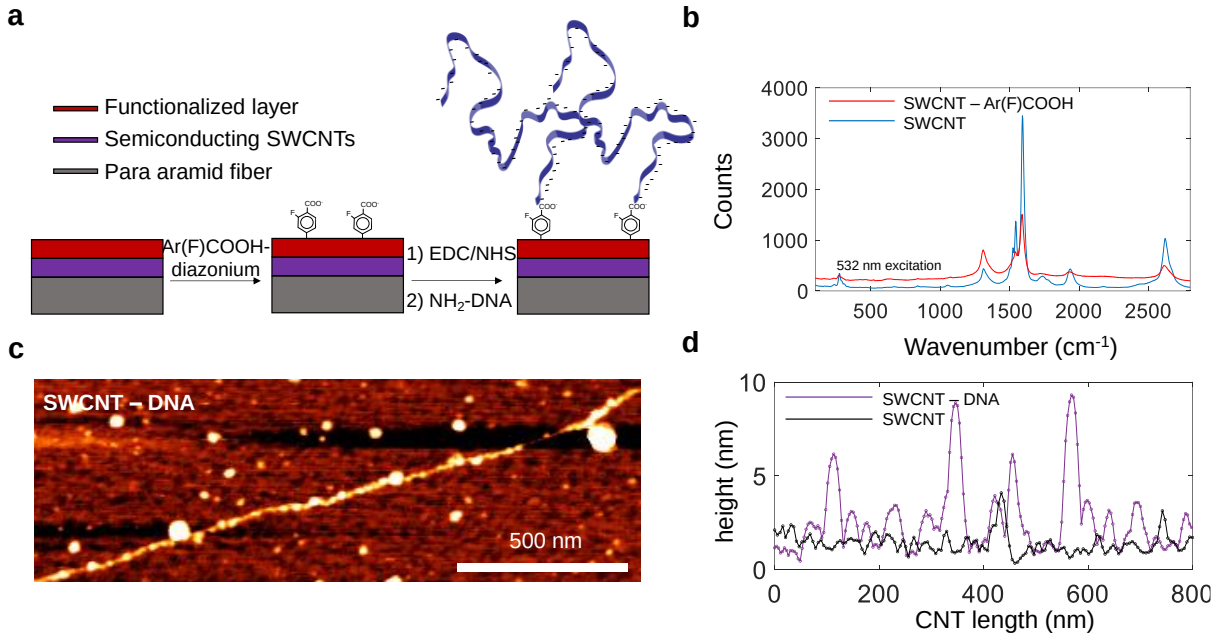

Figure 5-5. Chemical functionality can be added to the fiber FETs by coating them with a layer of covalently modified SWCNTs. a) Schematic showing a layer of 2-fluorobenzoic acid functionalized SWCNTs coated on the semiconducting fiber and subsequently functionalized with DNA aptamer probes. Features are not drawn to scale. **b)** Raman analysis of the SWCNTs before and after the reaction with 2-fluorobenzoic acid diazonium salt show a high degree of functionalization, as evidenced by the growth of the D peak (~1300 cm^{-1}) and loss of the radial breathing mode peak (~175 cm^{-1}). **c)** AFM confirms that the carboxylated SWCNTs can be functionalized with aptamer probes. **d)** Height analysis with AFM shows the aptamer probes on the SWCNT surface.

5.3.5 Electrical detection of dopamine using a fiber FET sensor

Aptamers are short DNA fragments which adopt an equilibrium 3-dimensional conformation in solution. When an aptamer binds with its target molecule, the conformation changes. In sensing applications, aptamers are chosen that can shift in and out of the Debye length of the sensors (Figure 5-6a), thus electrostatically gating the FET sensor even in high ionic strength conditions.[39,49] We can confirm this behavior by measuring a solution gated IV curve. After attaching the aptamer probes to the carboxyl-functionalized fiber, we observe an increase in the conductance (Figure 5-6b). This is due to the increased negative charge density of the aptamer probes near the semiconducting fiber surface. The semiconducting SWCNTs are a p-type material, and the negative aptamers are analogous to a negative gate voltage. After adding 1 mM dopamine to the solution however, the current decreases again (Figure 5-6b). This suggests that the aptamer extends away from the sensor surface when it binds with the dopamine, which his analogous to reducing the magnitude of the negative gate voltage. We also note that some of the device response may be due to the electrochemical oxidation of dopamine on the gold solution gate probe which is a common complication reported in literature. We anticipate that a thin passivating layer of Perylene C or polystyrene may reduce this contribution.

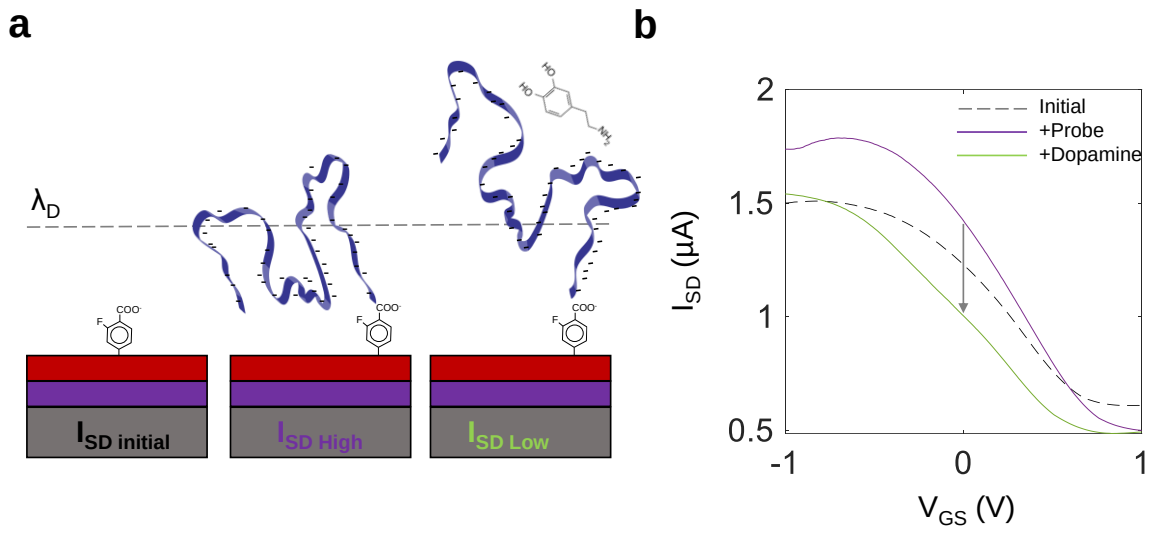

Figure 5-6. Conductance of the fiber FET can be modulated by dopamine binding with the aptamer probe. a) The spatial conformation of the aptamer probe shifts when binding with the dopamine target, electrostatically gating the semiconducting SWCNT coating on the fiber FET. The Debye length is indicated by λ_D. Features are not drawn to scale. **b)** This electrostatic gating is visible as a shift in the fiber conductance.

5.4 Conclusions

Electrical gating behavior in response to dopamine indicates that these fiber FET devices can be used as a chemical sensing platform. The 10 μm diameter of the fibers makes this one of the smallest FET chemical sensors. Additionally, we have shown that the electrical and chemical functionality of the fibers can easily be tuned by taking advantage of the wide range of solution processing methods for chirality sorting and chemical functionalization available to SWCNTs, which provides an advantage over traditional chemical probes made from shank style substrates, conventional metals, and inorganic semiconductors. Finally, the potential for a high production rate enabled by the high strength of the para-aramid and the ability to coat aligned SWCNTs at

>0.6 km min^{-1} shows that this device geometry can be scaled to meet the demand of the growing market for neural implants.

Chapter 6: Summary and Outlook

In summary, this dissertation demonstrates that structural control enabled by solution processed Tube^2 nanostructures is key to addressing the fundamental challenges of electrical biosensing. We have shown that Tube^2 nanostructures ordered into parallel electrical pathways can overcome the time barrier presented by trace molecule detection while retaining selectivity and ultrahigh sensitivity. This advance is enabled by the full-length dispersion of Tube-in-a-tube (Tube^2) nanostructures by superacid surfactant exchange[85] and subsequent length sorting procedures.[33] Furthermore, we have found that these long nanostructures can be ordered into self-assembled liquid crystalline gel for printing and coating on a variety of substrates, increasing the level of structural control to the microscopic and bulk domains. Thin films of Tube^2 nanostructures and carbon nanotubes printed from the gel can be suspended over etched trenches on a traditional substrate or coated onto the surface of strong synthetic fibers. The thin films provide the first high-throughput printing technique for fabricating aligned suspended thin films, towards high performance sensors. Additionally, the carbon nanotube coated fibers developed in this work may prove useful for implantable field-effect transistor (FET) biosensors with an ultrasmall footprint. These advances have immediate and practical implications for healthcare as improved electrical biosensing promises to further expand the availability of diagnostic tools, resulting in a more decentralized approach to public health. This means that the time between symptom onset and diagnosis can be shortened, diagnostic tools will become more available in regions where traditional healthcare networks are not sufficiently developed, and healthcare costs can potentially be reduced.

Additionally, in regard to fundamental studies, the importance of structural control and new techniques outlined in this dissertation may enable a further exploration of the physical limits of

chemical gating with Tube^2 nanostructures. The chemical sensing experiments conducted in this dissertation have relied on a phenomenon we previously described as chemical gating.[3] Evidenced through this and previous work[3,31] by a substantial shift in threshold voltage when the Tube^2 sensor is exposed to charged target molecules, this shift has enabled chemical detection with only 2 electrodes, instead of the typical 3-electrode design required in other FET sensors. Thus, while the phenomenon of chemical gating has proven useful in sensor design at the ensemble level, the fundamental limits at the single nanostructure level have yet to be determined. Validation of chemical gating can potentially be achieved in a carefully controlled, single-Tube^2 device by quantitatively correlating the target molecule charge with the electrical signal generated.

Recent advances in partner labs may enable such a highly optimized device platform for validating chemical gating at the single nanostructure level. For example, chirality sorting of double-wall carbon nanotubes developed by Flavel and colleagues can potentially be used to control the inner wall bandgap of the Tube^2 nanostructure (Figure 6-1a).[9] Ultrapure double-wall carbon nanotubes with semiconducting inner walls exhibit excellent FET characteristics[9] and will be useful for validation of the chemical gating theory at the single-Tube^2 level. (Figure 6-1b). Furthermore, a system of "spatially correlated" DNA probes is a concept we are developing that can potentially be used in such a study to maintain a higher charge density within the Debye length of the Tube^2 nanostructures with improved selectivity (Figure 6-1c). Finally, the solution dispersal and self-assembly of long Tube^2 nanostructures developed in this dissertation facilitate the fabrication of devices with discrete suspended electrical pathways (Figure 6-1d) that will be used in future fundamental studies.

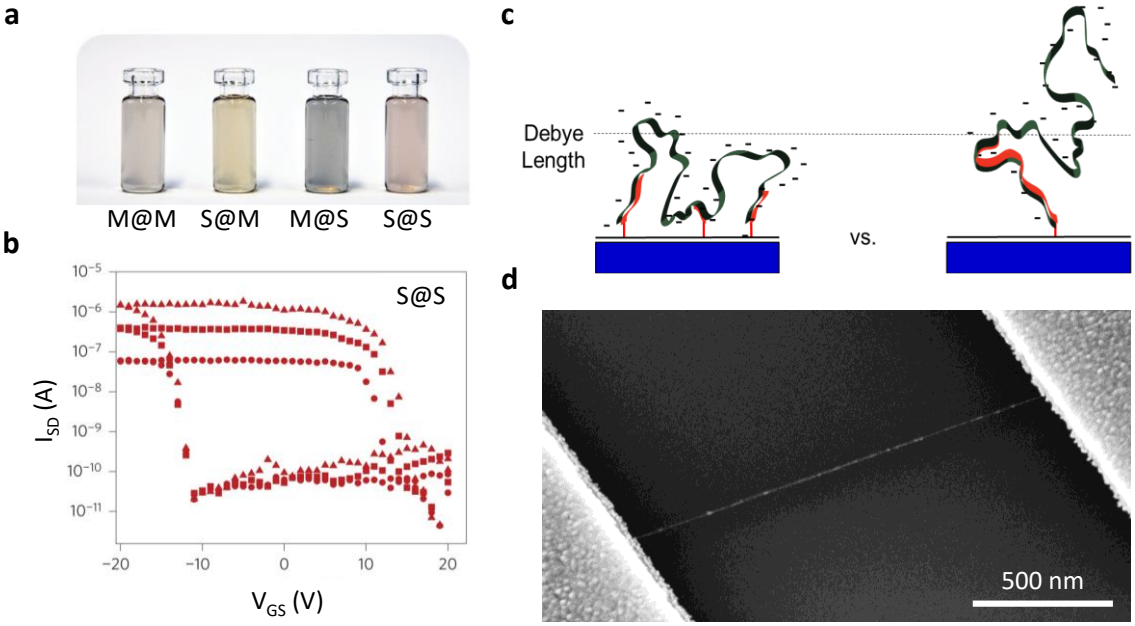

Figure 6-1. Structure control can be used to explore the limit of chemical gating. a) Recent advances in column chromatography enable separation of DWCNTs by inner and outer wall bandgap. S indicates a semiconducting wall; M indicates a metallic wall. S@M is shorthand for a semiconducting inner wall and metallic outer wall. **b)** DWCNTs with semiconducting inner and outer walls exhibit excellent FET characteristics that will be useful for validation of the chemical gating theory at the single-Tube^2 level. Figures a and b are adapted with permission from reference [9]. **c)** Correlated DNA probes (on the right) can potentially be used to study chemical gating. The small probe fragments pull the DNA target closer to the Tube^2 surface than a traditional long DNA probe (on the left). **d)** An individual aligned and suspended long Tube^2 nanostructure, like the one shown here, provide an ideal electrical system for studying the limits of chemical gating. The fabrication of such devices is facilitated by the techniques developed in this dissertation.

Together, these advances will enable the fabrication of a carefully controlled Tube^2 system of predetermined electrical parameters. By using DNA targets of different lengths, and by comparing the electrical response with neutral peptide nucleic acids, we anticipate that it will be possible to create a direct and quantitative correlation between target molecule charge density and the electrical response of the Tube^2 sensor.

6.1 Contributions to the field and new questions

Fundamental discoveries:

- Long CNT self-interactions lead to partitioning by length in solution.
- Constriction of electrical current to parallel electrical pathways increases sensitivity of chemical detection.
- Densely functionalized and suspended Tube^2 nanostructures can detect DNA hybridization in high ionic strength conditions.
- pH-tuned CNT/surfactant gels exhibit liquid crystalline properties.

Technical advances:

- Iterative sorting enables the extraction of CNTs up to 18 µm in length.
- Aligned and suspended Tube^2 nanostructures collectively enable rapid detection of trace biomarkers.
- CNT/surfactant gel can be printed into aligned and suspended thin films.
- Synthetic microfibers can be coated with aligned monolayers of CNTs by pulling them rapidly through surfactant gel.

Opened questions:

- How does signal and noise scale for aligned and suspended Tube^2 sensors between an individual nanostructure, and thousands of parallel nanostructures?

- What is the mechanism enabling chemical detection in high ionic strength when using densely functionalized Tube^2 nanostructures?

Bibliography

(1) Wang, P.; Barnes, B.; Huang, Z.; Wang, Z.; Zheng, M.; Wang, Y. Beyond Color: The New Carbon Ink. *Adv. Mater.* **2021**, *33*, 2005890.

(2) Piao, Y.; Chen, C.-F.; Green, A. A.; Kwon, H.; Hersam, M. C.; Lee, C. S.; Schatz, G. C.; Wang, Y. Optical and Electrical Properties of Inner Tubes in Outer Wall-Selectively Functionalized Double-Wall Carbon Nanotubes. *J. Phys. Chem. Lett.* **2011**, *2*, 1577-1582.

(3) Ng, A. L.; Chen, C.-F.; Kwon, H.; Peng, Z.; Lee, C. S.; Wang, Y. Chemical Gating of a Synthetic Tube-in-a-Tube Semiconductor. *J. Am. Chem. Soc.* **2017**, *139*, 3045-3051.

(4) Kroto, H. W.; Heath, J. R.; O'Brien, S. C.; Curl, R. F.; Smalley, R. E. C60: Buckminsterfullerene. *Nature* **1985**, *318*, 162-163.

(5) Iijima, S. Helical microtubules of graphitic carbon. *Nature* **1991**, *354*, 56-58.

(6) Iijima, S.; Ichihashi, T. Single-shell carbon nanotubes of 1-nm diameter. *Nature* **1993**, *363*, 603-605.

(7) Novoselov, K. S.; Geim, A. K.; Morozov, S. V.; Jiang, D.; Zhang, Y.; Dubonos, S. V.; Grigorieva, I. V.; Firsov, A. A. Electric Field Effect in Atomically Thin Carbon Films. *Science* **2004**, *306*, 666.

(8) Wang, P.; Peng, Z.; Li, M.; Wang, Y. Stretchable Transparent Conductive Films from Long Carbon Nanotube Metals. *Small* **2018**, *14*, 1802625.

(9) Li, H.; Gordeev, G.; Wasserroth, S.; Chakravadhanula, V. S. K.; Neelakandhan, S. K. C.; Hennrich, F.; Jorio, A.; Reich, S.; Krupke, R.; Flavel, B. S. Inner- and Outer-Wall Sorting of Double-Walled Carbon Nanotubes. *Nat. Nanotechnol.* **2017**, *12*, 1176-1182.

(10) Javey, A.; Guo, J.; Wang, Q.; Lundstrom, M.; Dai, H. Ballistic carbon nanotube field-effect transistors. *Nature* **2003**, *424*, 654-657.

(11) Bonaccorso, F.; Colombo, L.; Yu, G.; Stoller, M.; Tozzini, V.; Ferrari, A. C.; Ruoff, R. S.; Pellegrini, V. Graphene, related two-dimensional crystals, and hybrid systems for energy conversion and storage. *Science* **2015**, *347*, 1246501.

(12) Endo, M.; Muramatsu, H.; Hayashi, T.; Kim, Y. A.; Terrones, M.; Dresselhaus, M. S. 'Buckypaper' from coaxial nanotubes. *Nature* **2005**, *433*, 476-476.

(13) Peng, Y.; Cullis, T.; Inkson, B. Accurate electrical testing of individual gold nanowires by in situ scanning electron microscope nanomanipulators. *Appl. Phys. Lett.* **2008**, *93*, 183112.

(14) Chung, S.-W.; Yu, J.-Y.; Heath, J. R. Silicon nanowire devices. *Appl. Phys. Lett.* **2000**, *76*, 2068-2070.

(15) Mann, D.; Javey, A.; Kong, J.; Wang, Q.; Dai, H. Ballistic Transport in Metallic Nanotubes with Reliable Pd Ohmic Contacts. *Nano Lett.* **2003**, *3*, 1541-1544.

(16) Tilke, A.; Pescini, L.; Erbe, A.; Lorenz, H.; Blick, R. H. Electron-phonon interaction in suspended highly doped silicon nanowires. *Nanotechnol.* **2002**, *13*, 491-494.

(17) Morgan, M. Electrical conduction in amorphous carbon films. *Thin Solid Films* **1971**, *7*, 313-323.

(18) Castro Neto, A. H.; Guinea, F.; Peres, N. M. R.; Novoselov, K. S.; Geim, A. K. The electronic properties of graphene. *Rev. Mod. Phys.* **2009**, *81*, 109-162.

(19) He, P.; Cao, J.; Ding, H.; Liu, C.; Neilson, J.; Li, Z.; Kinloch, I. A.; Derby, B. Screen-Printing of a Highly Conductive Graphene Ink for Flexible Printed Electronics. *ACS Appl. Mater. Interfaces* **2019**, *11*, 32225-32234.

(20) Karagiannidis, P. G.; Hodge, S. A.; Lombardi, L.; Tomarchio, F.; Decorde, N.; Milana, S.; Goykhman, I.; Su, Y.; Mesite, S. V.; Johnstone, D. N.; Leary, R. K.; Midgley, P. A.; Pugno, N. M.; Torrisi, F.; Ferrari, A. C. Microfluidization of Graphite and Formulation of Graphene-Based Conductive Inks. *ACS Nano* **2017**, *11*, 2742-2755.

(21) Franklin, A. D. Nanomaterials in transistors: From high-performance to thin-film applications. *Science* **2015**, *349*, 704-713.

(22) Yang, F.; Wang, M.; Zhang, D.; Yang, J.; Zheng, M.; Li, Y. Chirality Pure Carbon Nanotubes: Growth, Sorting, and Characterization. *Chem. Rev.* **2020**, *120*, 2693-2758.

(23) Schroeder, V.; Savagatrup, S.; He, M.; Lin, S.; Swager, T. M. Carbon Nanotube Chemical Sensors. *Chem. Rev.* **2019**, *119*, 599-663.

(24) Cao, Q. e. a. Carbon nanotube transistors scaled to a 40-nanometer footprint. *Science* **2017**, 1369 – 1372.

(25) Kong, J. e. a. Nanotube Molecular Wires as Chemical Sensors. *Science* **2000**, 622 – 625.

(26) Collins, P. G. e. a. Extreme Oxygen Sensitivity of Electronic Properties of Carbon Nanotubes. *Science* **2000**, 1801 – 1804.

(27) Choi, Y.; Moody, I. S.; Sims, P. C.; Hunt, S. R.; Corso, B. L.; Perez, I.; Weiss, G. A.; Collins, P. G. Single-Molecule Lysozyme Dynamics Monitored by an Electronic Circuit. *Science* **2012**, 319-324.

(28) Sorgenfrei, S.; Chiu, C.-y.; Gonzalez, R. L.; Yu, Y.-J.; Kim, P.; Nuckolls, C.; Shepard, K. L. Label-free single-molecule detection of DNA-hybridization kinetics with a carbon nanotube field-effect transistor. *Nat. Nanotechnol.* **2011**, *6*, 126-132.

(29) Brozena, A. H.; Kim, M.; Powell, L. R.; Wang, Y. Controlling the optical properties of carbon nanotubes with organic colour-centre quantum defects. *Nat. Rev. Chem.* **2019**, *3*, 375-392.

(30) Luo, H.-B.; Wang, P.; Wu, X.; Qu, H.; Ren, X.; Wang, Y. One-pot, large-scale synthesis of organic color center-tailored semiconducting carbon nanotubes. *ACS Nano* **2019**, *13*, 8417-8424.

(31) Huang, J.; Ng, A. L.; Piao, Y.; Chen, C.-F.; Green, A. A.; Sun, C.-F.; Hersam, M. C.; Lee, C. S.; Wang, Y. Covalently Functionalized Double-Walled Carbon Nanotubes Combine High Sensitivity and Selectivity in the Electrical Detection of Small Molecules. *J. Am. Chem. Soc.* **2013**, *135*, 2306-2312.

(32) Green, A. A. H., M.C. Processing and properties of highly enriched double-wall carbon nanotubes. *Nature* **2009**, *4*, 64 – 70.

(33) Wang, P.; Barnes, B.; Wu, X.; Qu, H.; Zhang, C.; Shi, Y.; Headrick, R. J.; Pasquali, M.; Wang, Y. Self-Sorting of 10-μm-Long Single-Walled Carbon Nanotubes in Aqueous Solution. *Adv. Mater.* **2019**, *31*, 1901641.

(34) Sheehan, P. E.; Whitman, L. J. Detection Limits for Nanoscale Biosensors. *Nano Lett.* **2005**, *5*, 803-807.

(35) Israelachvili, J. N.: *Intermolecular and Surface Forces*; 3rd ed.; Academic Press: Burlington, 2011.

(36) Butt, J. H. K., M. : *Surface and interfacial forces*; Wiley, 2010.

(37) Elnathan, R. K., M.; Pevzner, A,; Engel, Y.; Burstein, L.; KhatchTourints, A.; Lichtenstein, A.; Kantaev, R.; Patolsky, F. Biorecognition Layer Engineering: Overcoming Screening Limitations of Nanowire-Based FET Devices. *Nano Lett.* **2012**, *12*, 5245-5254.

(38) Maehashi, K. K., T.; Kerman, K.; Takumura, Y.; Matsumoto, K.; Tamiya, E. Label-Free Protein Biosensor Based on Aptamer-Modified Carbon Nanotube Field-Effect Transistors. *Anal. Chem.* **2007**, *79*, 782-787.

(39) Nakatsuka, N.; Yang, K.-A.; Abendroth, J. M.; Cheung, K. M.; Xu, X.; Yang, H.; Zhao, C.; Zhu, B.; Rim, Y. S.; Yang, Y.; Weiss, P. S.; Stojanovich, M. N.; Andrews, A. M. Aptamer–Field-Effect Transistors Overcome Debye Length Limitations for Small-Molecule Sensing. *Science* **2018**, *361*, 319-324.

(40) Gao, N.; Gao, T.; Yang, X.; Dai, X.; Zhou, W.; Zhang, A.; Lieber, C. M. Specific Detection of Biomolecules in Physiological Solutions Using Graphene Transistor Biosensors. *PNAS* **2016**, *113*, 14633-14638.

(41) Goh, G. L.; Agarwala, S.; Yeong, W. Y. Directed and On-Demand Alignment of Carbon Nanotube: A Review toward 3D Printing of Electronics. *Advanced Materials Interfaces* **2019**, *6*, 1801318.

(42) Kang, S. J.; Kocabas, C.; Ozel, T.; Shim, M.; Pimparkar, N.; Alam, M. A.; Rotkin, S. V.; Rogers, J. A. High-performance electronics using dense, perfectly aligned arrays of single-walled carbon nanotubes. *Nat. Nanotechnol.* **2007**, *2*, 230-236.

(43) Yongho Joo, G. J. B., Michael S. Arnold, Padma Gopalan. Dose-Controlled, Floating Evaporative Self-assembly and Alignment of Semiconducting Carbon Nanotubes from Organic Solvents. *Langmuire* **2014**, *30*, 3460-3466.

(44) Li, Q.; Liu, J. Combined Printing of Highly Aligned Single-Walled Carbon Nanotube Thin Films with Liquid Metal for Direct Fabrication of Functional Electronic Devices. *Advanced Electronic Materials* **2020**, *6*, 2000537.

(45) Zhao, M.; Chen, Y.; Wang, K.; Zhang, Z.; Streit, J. K.; Fagan, J. A.; Tang, J.; Zheng, M.; Yang, C.; Zhu, Z.; Sun, W. DNA-directed nanofabrication of high-performance carbon nanotube field-effect transistors. *Science* **2020**, *368*, 878-881.

(46) Sun, W.; Shen, J.; Zhao, Z.; Arellano, N.; Rettner, C.; Tang, J.; Cao, T.; Zhou, Z.; Ta, T.; Streit, J. K.; Fagan, J. A.; Schaus, T.; Zheng, M.; Han, S.-J.; Shih, W. M.; Maune, H. T.; Yin, P. Precise pitch-scaling of carbon nanotube arrays within three-dimensional DNA nanotrenches. *Science* **2020**, *368*, 874-877.

(47) Liu, S.; Zhang, J.; Nshimiyimana, J. P.; Chi, X.; Hu, X.; Wu, P.; Liu, J.; Wang, G.; Sun, L. Ultraclean individual suspended single-walled carbon nanotube field effect transistor. *Nanotechnology* **2018**, *29*, 175302.

(48) Sedky, S.; Witvrouw, A.; Bender, H.; Baert, K. Experimental determination of the maximum post-process annealing temperature for standard CMOS wafers. *IEEE Trans. Electron Devices* **2001**, *48*, 377-385.

(49) Zhao, C.; Cheung, K. M.; Huang, I.-W.; Yang, H.; Nakatsuka, N.; Liu, W.; Cao, Y.; Man, T.; Weiss, P. S.; Monbouquette, H. G.; Andrews, A. M. Implantable aptamer-field-effect transistor neuroprobes for in vivo neurotransmitter monitoring. *Sci. Adv.* **2021**, *7*, eabj7422.

(50) Feng, J.; Chen, C.; Sun, X.; Peng, H. Implantable Fiber Biosensors Based on Carbon Nanotubes. *Accounts of Materials Research* **2021**, *2*, 138-146.

(51) Wu, X.; Feng, J.; Deng, J.; Cui, Z.; Wang, L.; Xie, S.; Chen, C.; Tang, C.; Han, Z.; Yu, H.; Sun, X.; Peng, H. Fiber-shaped organic electrochemical transistors for biochemical detections with high sensitivity and stability. *Science China Chemistry* **2020**, *63*, 1281-1288.

(52) Wang, L.; Xie, S.; Wang, Z.; Liu, F.; Yang, Y.; Tang, C.; Wu, X.; Liu, P.; Li, Y.; Saiyin, H.; Zheng, S.; Sun, X.; Xu, F.; Yu, H.; Peng, H. Functionalized helical fibre bundles of

carbon nanotubes as electrochemical sensors for long-term in vivo monitoring of multiple disease biomarkers. *Nat. Biomed. Eng.* **2020**, *4*, 159-171.

(53) O'connell, M. J.; Bachilo, S. M.; Huffman, C. B.; Moore, V. C.; Strano, M. S.; Haroz, E. H.; Rialon, K. L.; Boul, P. J.; Noon, W. H.; Kittrell, C.; Ma, J.; Hauge, R. H.; Weisman, R. B.; Smalley, R. E. Band gap fluorescence from individual single-walled carbon nanotubes. *Science* **2002**, *297*, 593-596.

(54) Wu, Z.; Chen, Z.; Du, X.; Logan, J. M.; Sippel, J.; Nikolou, M.; Kamaras, K.; Reynolds, J. R.; Tanner, D. B.; Hebard, A. F.; Rinzler, A. G. Transparent, Conductive Carbon Nanotube Films. *Science* **2004**, *305*, 1273-1276.

(55) Behabtu, N.; Young, C. C.; Tsentalovich, D. E.; Kleinerman, O.; Wang, X.; Ma, A. W.; Bengio, E. A.; ter Waarbeek, R. F.; de Jong, J. J.; Hoogerwerf, R. E.; Fairchild, S. B.; Ferguson, J. B.; Marayama, B.; Kono, J.; Talmon, Y.; Cohen, Y.; Otto, M. J.; Pasquali, M. Strong, light, multifunctional fibers of carbon nanotubes with ultrahigh conductivity. *Science* **2013**, *339*, 182-186.

(56) Bai, Y.; Zhang, R.; Ye, X.; Zhu, Z.; Xie, H.; Shen, B.; Cai, D.; Liu, B.; Zhang, C.; Jia, Z.; Zhang, S.; Li, X.; Wei, F. Carbon nanotube bundles with tensile strength over 80 GPa. *Nat. Nanotechnol.* **2018**, *13*, 589-595.

(57) Arnold, M. S.; Green, A. A.; Hulvat, J. F.; Stupp, S. I.; Hersam, M. C. Sorting carbon nanotubes by electronic structure using density differentiation. *Nat. Nanotechnol.* **2006**, *1*, 60.

(58) Tu, X.; Manohar, S.; Jagota, A.; Zheng, M. DNA sequence motifs for structure-specific recognition and separation of carbon nanotubes. *Nature* **2009**, *460*, 250-253.

(59) Liu, H.; Nishide, D.; Tanaka, T.; Kataura, H. Large-scale single-chirality separation of single-wall carbon nanotubes by simple gel chromatography. *Nat. Commun.* **2011**, *2*, 309.

(60) Khripin, C. Y.; Fagan, J. A.; Zheng, M. Spontaneous partition of carbon nanotubes in polymer-modified aqueous phases. *J. Am. Chem. Soc.* **2013**, *135*, 6822-6825.

(61) Kostarelos, K. The long and short of carbon nanotube toxicity. *Nat. Biotechnol.* **2008**, *26*, 774.

(62) Kolosnjaj-Tabi, J.; Hartman, K. B.; Boudjemaa, S.; Ananta, J. S.; Morgant, G.; Szwarc, H.; Wilson, L. J.; Moussa, F. In vivo behavior of large doses of ultrashort and full-length single-walled carbon nanotubes after oral and intraperitoneal administration to Swiss mice. *ACS Nano* **2010**, *4*, 1481-1492.

(63) Hecht, D. S.; Hu, L.; Irvin, G. Emerging transparent electrodes based on thin films of carbon nanotubes, graphene, and metallic nanostructures. *Adv. Mater.* **2011**, *23*, 1482-1513.

(64) Tsentalovich, D. E.; Headrick, R. J.; Mirri, F.; Hao, J.; Behabtu, N.; Young, C. C.; Pasquali, M. Influence of carbon nanotube characteristics on macroscopic fiber properties. *ACS Appl. Mater. Interfaces* **2017**, *9*, 36189-36198.

(65) Headrick, R. J.; Tsentalovich, D. E.; Berdegué, J.; Bengio, E. A.; Liberman, L.; Kleinerman, O.; Lucas, M. S.; Talmon, Y.; Pasquali, M. Structure–property relations in carbon nanotube fibers by downscaling solution processing. *Adv. Mater.* **2018**, *30*, 1704482.

(66) Kamalasanan, K.; Gottardi, R.; Tan, S.; Chen, Y.; Godugu, B.; Rothstein, S.; Balazs, A. C.; Star, A.; Little, S. R. "Zero-Dimensional" Single-Walled Carbon Nanotubes. *Angew. Chem. Int. Ed.* **2013**, *52*, 11308-11312.

(67) Danne, N.; Kim, M.; Godin, A. G.; Kwon, H.; Gao, Z.; Wu, X.; Hartmann, N. F.; Doorn, S. K.; Lounis, B.; Wang, Y.; Cognet, L. Ultrashort Carbon Nanotubes That Fluoresce Brightly In The Near-Infrared. *ACS Nano* **2018**, *12*, 6059-6065.

(68) Khripin, C. Y.; Tu, X.; Heddleston, J. M.; Silvera-Batista, C.; Hight Walker, A. R.; Fagan, J.; Zheng, M. High-resolution length fractionation of surfactant-dispersed carbon nanotubes. *Anal. Chem.* **2013**, *85*, 1382-1388.

(69) Jeffrey A. Fagan, M. L. B., Jaehun Chun, Pingting Nie, Barry J. Bauer, Jeffrey R. Simpson, Angela Hight-Walker, Erik K. Hobbie. Centrifugal Length Separation of Carbon Nanotubes. *Langmuir* **2008**, *24*, 13880-13889.

(70) Ohmori, S.; Saito, T.; Shukla, B.; Yumura, M.; Iijima, S. Fractionation of single wall carbon nanotubes by length using cross flow filtration method. *ACS Nano* **2010**, *4*, 3606-3610.

(71) Gui, H.; Chen, H.; Khripin, C. Y.; Liu, B.; Fagan, J. A.; Zhou, C.; Zheng, M. A facile and low-cost length sorting of single-wall carbon nanotubes by precipitation and applications for thin-film transistors. *Nanoscale* **2016**, *8*, 3467-3473.

(72) Fagan, J. A.; Becker, M. L.; Chun, J.; Nie, P.; Bauer, B. J.; Simpson, J. R.; Hight-Walker, A.; Hobbie, E. K. Centrifugal length separation of carbon nanotubes. *Langmuir* **2008**, *24*, 13880-13889.

(73) Miyata, Y.; Shiozawa, K.; Asada, Y.; Ohno, Y.; Kitaura, R.; Mizutani, T.; Shinohara, H. Length-sorted semiconducting carbon nanotubes for high-mobility thin film transistors. *Nano Res.* **2011**, *4*, 963-970.

(74) Allard, S.; Forster, M.; Souharce, B.; Thiem, H.; Scherf, U. Organic semiconductors for solution-processable field-effect transistors (OFETs). *Angew. Chem. Int. Ed.* **2008**, *47*, 4070-4098.

(75) Sun, Y.; Rogers, J. A. Inorganic semiconductors for flexible electronics. *Adv. Mater.* **2007**, *19*, 1897-1916.

(76) Street, R. A. Thin-film transistors. *Adv. Mater.* **2009**, *21*, 2007-2022.

(77) Tsentalovich, D. E.; Ma, A. W.; Lee, J. A.; Behabtu, N.; Bengio, E. A.; Choi, A.; Hao, J.; Luo, Y.; Headrick, R. J.; Green, M. J.; Talmon, Y.; Pasquali, M. Relationship of extensional viscosity and liquid crystalline transition to length distribution in carbon nanotube solutions. *Macromolecules* **2016**, *49*, 681-689.

(78) He, X.; Gao, W.; Xie, L.; Li, B.; Zhang, Q.; Lei, S.; Robinson, J. M.; Hároz, E. H.; Doorn, S. K.; Wang, W.; Vajtai, R.; Ajayan, P. M.; Adams, W. W.; Hauge, R. H.; Kono, J. Wafer-scale monodomain films of spontaneously aligned single-walled carbon nanotubes. *Nat. Nanotechnol.* **2016**, *11*, 633-638.

(79) Davis, V. A.; Parra-Vasquez, A. N. G.; Green, M. J.; Rai, P. K.; Behabtu, N.; Prieto, V.; Booker, R. D.; Schmidt, J.; Kesselman, E.; Zhou, W.; Fan, H.; Adams, W. W.; Hauge, R. H.; Fischer, J. E.; Cohen, Y.; Talmon, Y.; Smalley, R. E.; Pasquali, M. True solutions of single-walled carbon nanotubes for assembly into macroscopic materials. *Nat. Nanotechnol.* **2009**, *4*, 830.

(80) Hu, H.; Zhao, B.; Itkis, M. E.; Haddon, R. C. Nitric Acid Purification of Single-Walled Carbon Nanotubes. *J. Phys. Chem. B* **2003**, *107*, 13838-13842.

(81) Tchoul, M. N.; Ford, W. T.; Lolli, G.; Resasco, D. E.; Arepalli, S. Effect of Mild Nitric Acid Oxidation on Dispersability, Size, and Structure of Single-Walled Carbon Nanotubes. *Chem. Mater.* **2007**, *19*, 5765-5772.

(82) Karousis, N.; Tagmatarchis, N.; Tasis, D. Current Progress on the Chemical Modification of Carbon Nanotubes. *Chem. Rev.* **2010**, *110*, 5366-5397.

(83) Ziegler, K. J.; Gu, Z.; Peng, H.; Flor, E. L.; Hauge, R. H.; Smalley, R. E. Controlled Oxidative Cutting of Single-Walled Carbon Nanotubes. *J. Am. Chem. Soc.* **2005**, *127*, 1541-1547.

(84) Parra-Vasquez, A. N. G.; Behabtu, N.; Green, M. J.; Pint, C. L.; Young, C. C.; Schmidt, J.; Kesselman, E.; Goyal, A.; Ajayan, P. M.; Cohen, Y.; Talmon, Y.; Hauge, R. H.; Pasquali, M. Spontaneous Dissolution of Ultralong Single- and Multiwalled Carbon Nanotubes. *ACS Nano* **2010**, *4*, 3969-3978.

(85) Wang, P.; Kim, M.; Peng, Z.; Sun, C.-F.; Mok, J.; Lieberman, A.; Wang, Y. Superacid-Surfactant Exchange: Enabling Nondestructive Dispersion of Full-Length Carbon Nanotubes in Water. *ACS Nano* **2017**, *11*, 9231-9238.

(86) Onsager, L. The effects of shape on the interaction of colloidal particles. *Ann. N. Y. Acad. Sci.* **1949**, *51*, 627-659.

(87) Flory, P. J. Phase equilibria in solutions of rod-like particles. *Proc. R. Soc. Lond. A* **1956**, *234*, 73-89.

(88) Wensink, H.; Vroege, G. Isotropic–nematic phase behavior of length-polydisperse hard rods. *J. Chem. Phys.* **2003**, *119*, 6868-6882.

(89) Green, M. J.; Parra-Vasquez, A. N. G.; Behabtu, N.; Pasquali, M. Modeling the phase behavior of polydisperse rigid rods with attractive interactions with applications to single-walled carbon nanotubes in superacids. *J. Chem. Phys.* **2009**, *131*, 084901.

(90) Ramesh, S.; Ericson, L. M.; Davis, V. A.; Saini, R. K.; Kittrell, C.; Pasquali, M.; Billups, W.; Adams, W. W.; Hauge, R. H.; Smalley, R. E. Dissolution of pristine single walled carbon nanotubes in superacids by direct protonation. *J. Phys. Chem. B* **2004**, *108*, 8794-8798.

(91) Davis, V. A.; Ericson, L. M.; Parra-Vasquez, A. N. G.; Fan, H.; Wang, Y.; Prieto, V.; Longoria, J. A.; Ramesh, S.; Saini, R. K.; Kittrell, C. Phase behavior and rheology of SWNTs in superacids. *Macromolecules* **2004**, *37*, 154-160.

(92) Fagan, J. A.; Hároz, E. H.; Ihly, R.; Gui, H.; Blackburn, J. L.; Simpson, J. R.; Lam, S.; Hight Walker, A. R.; Doorn, S. K.; Zheng, M. Isolation of > 1 nm diameter single-wall carbon nanotube species using aqueous two-phase extraction. *ACS Nano* **2015**, *9*, 5377-5390.

(93) Chortos, A.; Pochorovski, I.; Lin, P.; Pitner, G.; Yan, X.; Gao, T. Z.; To, J. W.; Lei, T.; Will III, J. W.; Wong, H.-S. P.; Bao, Z. Universal Selective Dispersion of Semiconducting Carbon Nanotubes from Commercial Sources Using a Supramolecular Polymer. *ACS Nano* **2017**, *11*, 5660-5669.

(94) Sangwan, V. K.; Ortiz, R. P.; Alaboson, J. M.; Emery, J. D.; Bedzyk, M. J.; Lauhon, L. J.; Marks, T. J.; Hersam, M. C. Fundamental performance limits of carbon nanotube thin-film transistors achieved using hybrid molecular dielectrics. *ACS Nano* **2012**, *6*, 7480-7488.

(95) Zhang, L.; Tu, X.; Welsher, K.; Wang, X.; Zheng, M.; Dai, H. Optical characterizations and electronic devices of nearly pure (10, 5) single-walled carbon nanotubes. *J. Am. Chem. Soc.* **2009**, *131*, 2454-2455.

(96) Gubala, V.; Harris, L. F.; Ricco, A. J.; Tan, M. X.; Williams, D. E. Point of Care Diagnostics: Status and Future. *Anal. Chem.* **2012**, *84*, 487-515.

(97) Gambhir, S. S.; Ge, T. J.; Vermesh, O.; Spitler, R. Toward achieving precision health. *Sci. Transl. Med.* **2018**, *10*, eaao3612.

(98) Akkilic, N.; Geschwindner, S.; Höök, F. Single-molecule biosensors: Recent advances and applications. *Biosens. Bioelectron.* **2020**, *151*, 111944.

(99) Turner, A. P. F. Biosensors: Sense and Sensibility. *Chem. Soc. Rev.* **2013**, *42*, 3184-3196.

(100) Vashist, S. K.; Luppa, P. B.; Yeo, L. Y.; Ozcan, A.; Luong, J. H. T. Emerging Technologies for Next-Generation Point-of-Care Testing. *Trends Biotechnol.* **2015**, *33*, 692-705.

(101) Cao, Q.; Rogers, J. A. Ultrathin films of single-walled carbon nanotubes for electronics and sensors: A review of fundamental and applied aspects. *Adv. Mater.* **2009**, *21*, 29-53.

(102) Li, P.; Lee, G.-H.; Kim, S. Y.; Kwon, S. Y.; Kim, H.-R.; Park, S. From Diagnosis to Treatment: Recent Advances in Patient-Friendly Biosensors and Implantable Devices. *ACS Nano* **2021**, *15*, 1960-2004.

(103) Béraud, A.; Sauvage, M.; Bazán, C. M.; Tie, M.; Bencherif, A.; Bouilly, D. Graphene field-effect transistors as bioanalytical sensors: design, operation and performance. *Analyst* **2021**, *146*, 403-428.

(104) Stern, E.; Klemic, J. F.; Routenberg, D. A.; Wyrembak, P. N.; Turner-Evans, D. B.; Hamilton, A. D.; LaVan, D. A.; Fahmy, T. M.; Reed, M. A. Label-Free Immunodetection with CMOS-Compatible Semiconducting Nanowires. *Nature* **2007**, *445*, 519-522.

(105) Duchamp, M.; Lee, K.; Dwir, B.; Seo, J. W.; Kapon, E.; Forro, L.; Magrez, A. Controlled Positioning of Carbon Nanotubes by Dielectrophoresis: Insights into the Solvent and Substrate Role. *ACS Nano* **2010**, *4*, 279-284.

(106) Ng, A. L.; Sun, Y.; Powell, L.; Sun, C.-F.; Chen, C.-F.; Lee, C. S.; Wang, Y. Selective Breakdown of Metallic Pathways in Double-Walled Carbon Nanotube Networks. *Small* **2015**, *11*, 96-102.

(107) Bouilly, D.; Cabana, J.; Meunier, F.; Desjardins-Carrière, M.; Lapointe, F.; Gagnon, P.; Larouche, F. L.; Adam, E.; Paillet, M.; Martel, R. Wall-Selective Probing of Double-Walled Carbon Nanotubes Using Covalent Functionalization. *ACS Nano* **2011**, *5*, 4927-4934.

(108) Steere, A. C.; Strle, F.; Wormser, G. P.; Hu, L. T.; Branda, J. A.; Hovius, J. W. R.; Li, X.; Mead, P. S. Lyme borreliosis. *Nat. Rev. Dis. Primers* **2016**, *2*, 16090.

(109) Mei, J.; Li, Y.-T.; Zhang, H.; Xiao, M.-M.; Ning, Y.; Zhang, Z.-Y.; Zhang, G. J. Molybdenum Disulfide Field-Effect Transistor Biosensor for Ultrasensitive Detection of DNA by Employing Morpholino as Probe. *Biosens. Bioelectron.* **2018**, *110*, 71-77.

(110) Hajian, R.; Balderston, S.; Tran, T.; deBoer, T.; Etienne, J.; Sandhu, M.; Wauford, N. A.; Chung, J.-Y.; Nokes, J.; Athaiya, M.; Paredes, J.; Peytavi, R.; Goldsmith, B.; Murthy, N.; Conboy, I. M.; Aran, K. Detection of Unamplified Target Genes Via CRISPR–Cas9 Immobilized on a Graphene Field-Effect Transistor. *Nat. Biomed. Eng.* **2019**, *3*, 427-437.

(111) Poghossian, A.; Cherstvy, A.; Ingebrandt, S.; Offenhäusser, A.; Schöning, M. J. Possibilities and Limitations of Label-Free Detection of DNA Hybridization With Field-Effect-Based Devices. *Sensors Actuators B: Chem.* **2005**, *111-112*, 470-480.

(112) Damaschun, G.; Damaschun, H.; Misselwitz, R.; Pospelov, V. A.; Zalenskaya, I. A.; Zirwer, D.; Müller, J. J.; Vorobev, V. I. How Many Base-Pairs Per Turn Does DNA Have in Solution and in Chromatin? An Answer from Wide-Angle X-Ray Scattering. *Biomed. Biochim. Acta* **1983**, *42*, 697-703.

(113) Legay, G.; Markey, L.; Meunier-Prest, R.; Finot, E. Measurements of Thickness Dispersion in Biolayers by Scanning Force Microscopy and Comparison with Spectroscopic Ellipsometry Analysis. *Ultramicroscopy* **2007**, *107*, 1111-1117.

(114) Jinkins, K. R.; Foradori, S. M.; Saraswat, V.; Jacobberger, R. M.; Dwyer, J. H.; Gopalan, P.; Berson, A.; Arnold, M. S. Aligned 2D carbon nanotube liquid crystals for wafer-scale electronics. *Sci. Adv.* **2021**, *7*, eabh0640.

(115) Brady, G. J.; Way, A. J.; Safron, N. S.; Evensen, H. T.; Gopalan, P.; Arnold, M. S. Quasi-ballistic carbon nanotube array transistors with current density exceeding Si and GaAs. *Sci. Adv.* **2016**, *2*, e1601240.

(116) Liu, L.; Han, J.; Xu, L.; Zhou, J.; Zhao, C.; Ding, S.; Shi, H.; Xiao, M.; Ding, L.; Ma, Z.; Jin, C.; Zhang, Z.; Peng, L.-M. Aligned, high-density semiconducting carbon nanotube arrays for high-performance electronics. *Science* **2020**, *368*, 850-856.

(117) Seichepine, F. R., J.; Dudina, A.; Hierlemann, A.; Frey, U. . Dielectrophoresis-Assisted Integration of 1024 Carbon Nanotube Sensors into a CMOS Microsystem. *Adv. Mater.* **2017**, *29*.

(118) Subbaiyan, N. K.; Cambré, S.; Parra-Vasquez, A. N. G.; Hároz, E. H.; Doorn, S. K.; Duque, J. G. Role of Surfactants and Salt in Aqueous Two-Phase Separation of Carbon Nanotubes toward Simple Chirality Isolation. *ACS Nano* **2014**, *8*, 1619-1628.

(119) Zhang, C.; Wang, P.; Barnes, B.; Fortner, J.; Wang, Y. Cleanly Removable Surfactant for Carbon Nanotubes. *Chem. Mater.* **2021**, *33*, 4551-4557.

(120) Hobbie, E. K.; Fagan, J. A.; Becker, M. L.; Hudson, S. D.; Fakhri, N.; Pasquali, M. Self-Assembly of Ordered Nanowires in Biological Suspensions of Single-Wall Carbon Nanotubes. *ACS Nano* **2009**, *3*, 189-196.

(121) Marques, E. F.; Edlund, H.; La Mesa, C.; Khan, A. Liquid Crystals and Phase Equilibria Binary Bile Salt-Water Systems. *Langmuir* **2000**, *16*, 5178-5186.

(122) Christoff-Tempesta, T.; Cho, Y.; Kim, D.-Y.; Geri, M.; Lamour, G.; Lew, A. J.; Zuo, X.; Lindemann, W. R.; Ortony, J. H. Self-assembly of aramid amphiphiles into ultra-stable nanoribbons and aligned nanoribbon threads. *Nat. Nanotechnol.* **2021**.

(123) Hu, L.; Hecht, D. S.; Grüner, G. Percolation in Transparent and Conducting Carbon Nanotube Networks. *Nano Lett.* **2004**, *4*, 2513-2517.

(124) Patel, S. R.; Lieber, C. M. Precision electronic medicine in the brain. *Nat. Biotechnol.* **2019**, *37*, 1007-1012.

(125) Keefer, E. W.; Botterman, B. R.; Romero, M. I.; Rossi, A. F.; Gross, G. W. Carbon nanotube coating improves neuronal recordings. *Nat. Nanotechnol.* **2008**, *3*, 434-439.

(126) Acarón Ledesma, H.; Li, X.; Carvalho-de-Souza, J. L.; Wei, W.; Bezanilla, F.; Tian, B. An atlas of nano-enabled neural interfaces. *Nat. Nanotechnol.* **2019**, *14*, 645-657.

(127) Guosong Hong, C. M. L. Novel electrode technologies for neural recordings. *Nature Reviews Neuroscience* **2019**, *20*, 330-345.

(128) Yang, X.; Zhou, T.; Zwang, T. J.; Hong, G.; Zhao, Y.; Viveros, R. D.; Fu, T.-M.; Gao, T.; Lieber, C. M. Bioinspired neuron-like electronics. *Nature Materials* **2019**, *18*, 510-517.

(129) Cheng , M.; Chen, W.; Weerasooriya, T. Mechanical Properties of Kevlar® KM2 Single Fiber. *J. Eng. Mater. Technol.* **2005**, *127*, 197-203.

(130) Fan, L.; Feng, C.; Zhao, W.; Qian, L.; Wang, Y.; Li, Y. Directional Neurite Outgrowth on Superaligned Carbon Nanotube Yarn Patterned Substrate. *Nano Lett.* **2012**, *12*, 3668-3673.

(131) Masvidal-Codina, E.; Illa, X.; Dasilva, M.; Calia, A. B.; Dragojević, T.; Vidal-Rosas, E. E.; Prats-Alfonso, E.; Martínez-Aguilar, J.; De la Cruz, J. M.; Garcia-Cortadella, R.; Godignon, P.; Rius, G.; Camassa, A.; Del Corro, E.; Bousquet, J.; Hébert, C.; Durduran, T.; Villa, R.; Sanchez-Vives, M. V.; Garrido, J. A.; Guimerà-Brunet, A. High-resolution mapping of infraslow cortical brain activity enabled by graphene microtransistors. *Nature Materials* **2019**, *18*, 280-288.